Technische Universität München
Max-Planck-Institut für Biochemie
Abteilung Molekulare Strukturbiologie

Identification and Visualization of Macromolecules in intact cells by Cryo-electron Tomography.

Carolin Susanne Fleischer

Vollständiger Abdruck der von der Fakultät für Chemie
der Technischen Universität München
zur Erlangung des akademischen Grades eines

Doktors der Naturwissenschaften (Dr. rer. nat.)

genehmigten Dissertation.

Vositzender:		Univ.-Prof. Dr. J. Buchner
Prüfer der Dissertation:	1.	Hon.-Prof. Dr. W. Baumeister
	2.	Univ.-Prof. Dr. S. Weinkauf

Die Dissertation wurde am 31.08.2010 bei der Technischen Universität München eingereicht und durch die Fakultät für Chemie am 21.03.2011 angenommen.

Für meine Eltern

Contents

List of Figures

Abstract

The structure and function of macromolecules have been in the focus of scientific interest for decades. A central role is assigned to the ribosome, as a key part in the ubiquitous translation process. The determination of the crystal structure has been a milestone in ribosome research, but still very little is known about macromolecular complexes in their natural environment, the cytoplasm.

In this study, we provide information about the spatial distribution and orientation of ribosomes during different growth states in the model organism *Spiroplasma citri* by using cryo-electron tomography in combination with pattern recognition algorithms.

S. citri is a plant pathogenic bacterium from the family of Mollicutes that has no cell wall and is very little in size. With a diameter from 80 - 200 nm, this organism is well-suited for electron microscopic approaches. We recorded and analyzed a total of 38 tomograms in which ribosomes were identified by template matching techniques. The encountered particles were validated carefully before 3D averaging was performed. The averaged structures show differences during the different growth states: The average of the logarithmic phase ribosome shows three extra densities that are not present in the averages of stationary phase or starvation phase tomograms. One very prominent density is located at the binding site of the elongation factor, indicating that the ribosome is actively translating in this phase.

The number of ribosomes per visible part of the cell, as represented in the tomograms, decreases by 50% from the exponential to the stationary phase. For the starvation phase, the number of ribosomes decreases slightly further.

The distribution of the ribosomes was similar for the different growth states. No specific pattern was observed and the molecules are spread evenly throughout the cell. The distance of the ribosomes to the cell membrane was calculated and compared between the growth states but no preferred localization could be determined. For all growth phases the ribosomes show a statistical uniform distribution concerning their distance to the membrane.

In contrast to other organisms like *E. coli* or *B. subtilis*, *S. citri* does not form any kind of ribosomal clusters. The particles were examined in relation to their closest neighbor, but neither polyribosomes nor ribosome dimers occurred. However, the volume occupa-

tion of ribosomes per cell volume is approximately 50 % compared to *E. coli*.
As our results show that it is possible to get detailed information about protein structure and distribution, we decided to go one step further and develop genetic tools for *S. citri* in order to use it as *in vivo* expression system. The structure of foreign proteins could be determined in a cytosolic environment which comes closer to the native conditions than any isolated cellular fraction. We succeeded in generating an expression vector that was able to express 20S proteasome from *T. acidophilum* and Tripeptidyl Peptidase II from *D. melanogaster*.
We also expressed a fluorescent protein that could be used for localization studies in *S. citri*. As GFP is not suited for fluorescence experiments in *S. citri* we used a Flavin mononucleotide-based fluorescent protein (FbFP). *S. citri* grows under facultatively anaerobic conditions and the molecular oxygen level in the medium is not sufficient for GFP's chromophore activation. Still, the fluorescence signal is quite weak and more optimization has to be done to use FbFP routinely in *S. citri*. A labeling approach of endogenous proteins with a fluorescent tag failed due to a lacking recombination of the vector into the genome.

Zusammenfassung

Struktur und Funktion von makromolekularen Komplexen sind seit Jahrzehnten ein zentrales Interesse der Naturwissenschaft. Eine besondere Rolle spielt hierbei das Ribosom, aufgrund seiner zentralen Bedeutung im ubiquitären und essentiellen Vorgang der Protein Translation. Die Aufklärung der Kristallstruktur war ein wesentlicher Schritt in der Ribosomenforschung und es konnten viele Aussagen über die Funktionsweise aus der Struktur gezogen werden. Dennoch ist immer noch wenig bekannt über die Verteilung und die Orientierung der Ribosomen in ihrer natürlichen Umgebung: dem Zytoplasma. In dieser Arbeit wird die räumliche Verteilung und die Orientierung von Ribosomen in unterschiedlichen Wachstumsphasen im Modelorganismus *Spiroplasma citri* untersucht. Hierfür wird die Methode der Cryo-Elektronen Tomographie mit Mustererkennungsalgorithmen kombiniert.

S. citri ist ein sehr dünnes, pflanzen-pathogenes, zellwandfreies Bakterium aus der Familie der Mollicuten. Mit einem Durchmesser von nur 80 - 200 nm ist dieser Organismus hervorragend für Cryo-Elektronen Tomographie geeignet. Im Ganzen wurden 38 Tomogramme aufgenommen und analysiert, aus denen die Ribosomen mittels Mustererkennung identifiziert wurden. Die gefundenen Partikel wurden sorgfältig geprüft, bevor eine 3D Mittelung gemacht wurde. Die gemittelten Partikel zeigen deutliche Unterschiede je nach Wachstumsphase in denen die Tomogramme aufgenommen wurden: Die Struktur des Ribosoms aus logarithmisch wachsenden Zellen zeigt drei Extra-Massen, die weder in der Struktur der Ribosomen aus der stationären, noch in der Struktur der Ribosomen aus der Hungerphase sichtbar sind. Die prominenteste Extramasse sitzt an der Bindungsstelle für den Elongationsfaktor, was darauf hinweist, dass sich die Ribosomen zum Zeitpunkt der Aufnahme in einem aktiv translatierendem Zustand befanden.

Die Anzahl der Ribosomen pro Tomogramm und damit pro sichtbaren Zellausschnitt nimmt von der logarithmischen Phase zur stationären Phase um ca. 50% ab. Eine noch größere Abnahme sieht man zwischen logarithmischer und Hungerphase.

Die Verteilung der Ribosomen folgt in keiner der Wachstumsphasen einem speziellen Muster. Die Moleküle sind gleichmäßig über die ganze Zelle verteilt. Bei der Berechnung des Abstandes der Ribosomen zur Zellmembran ergab sich eine zufällige Gleichverteilung für alle Wachstumsphasen.

Im Gegensatz zu anderen Organismen wie *E. coli* oder *B. subtilis* formt *S. citri* keine ribosomalen Cluster. Es konnten weder Polyribosomen noch Dimere gefunden werden. Die Ribosomendichte bezogen auf das Zellvolumen entspricht etwa 50 % von der von *E. coli*.

Nachdem wir zeigen konnten, dass durch diesen Experimentationsansatz eine Fülle von Informationen über Struktur und Verteilung gewonnen werden können, sollte ein Expressionsvektor generiert werden, mit dem fremde Gene in *S. citri* exprimiert werden können. Die Struktur dieser Proteine könnte dann in einer zytosolischen Umgebung bestimmt werden, was die Proteine in einem naturnäheren Zustand erhält als bei einer Aufreinigung. Wir konnen einen Vektor klonieren, mit dem erfolgreich 20S Proteasom aus *T. acidophilum* und Tripeptidyl Peptidase II aus *D. melanogaster* exprimiert werden konnten.

Ebenso konnte erfolgreich ein fluoreszierendes Protein exprimiert werden, das in Zukunft für Markierungen in *S. citri* verwendet werden kann. Da GFP aufgrund des Sauerstoffmangels in den fakultativ anaerob wachsenden *S. citri* Zellen nicht geeignet ist, wurde ein Flavin Mononukleotid-basierendes fluoreszentes Protein (FbFP) verwendet, das ohne molekularen Sauerstoff auskommt. Das erhaltene Fluoreszenz-Signal ist jedoch noch sehr schwach und weitere Optimierungsarbeit muss investiert werden, bevor FbFP standardmäßig in *S. citri* verwendet werden kann.

Der Versuch, endogene Proteinen fluoreszent zu markieren schlug fehl, da der Vektor nicht ins Genom der Zellen integriert wurde.

1 Introduction

1.1 From Structural Biology to Visual Proteomics

Classical structural biology has contributed to the understanding of biological mechanisms to a large extend. For example the solution of crystal structures of the ribosome and its subunits, as well as cryo-electron microscopy of purified ribosomes, have helped to understand details of translation and its regulation [28, 39].
However, all these experiments were done with isolated and purified proteins. In contrast to this, visual proteomics aims at generating a molecular atlas of the macromolecular complexes of the cell and getting information on the spatial orientation, distribution, concentration and interaction of proteins in their natural environment [63, 51]. The first atlas of ribosomes in an intact cell was generated in 2006 [66]. Cellular tomograms are a valuable source of information as they show a snapshot of local molecular interactions, that are the basis of higher cellular processes and functions.
We focus on the ribosome as a key player of protein synthesis, a process of utmost importance for all living organisms. A comparison of the distribution, orientation and 3D averages of ribosomes in different growth states is a central question of this work. As model organism we use *Spiroplasma citri*, a bacterium that is well suited for tomo -graphic experiments with subsequent template matching approaches on intact cells due to its small size and apparently uncrowded cytoplasm. We combine cryo-electron tomography and a correlation-based algorithm called Molmatch [26] to identify and visualize ribosomes in the cytoplasm of *S. citri*.

1.2 Template Matching

1.2.1 Generation of Reference Structures from High Resolution Atomic Structures

The template recognition algorithm used is based on a correlative comparison of the known reference structure with the unknown protein structures in the cellular context of vitrified cells. Due to the limited resolution of cellular tomograms, complexes suited for

template matching are limited to a molecular mass of more than 300 kDa [79]. For the generation of reference structures that can be correlated with the tomographic data, the high resolution structures must be downsampled to the resolution of the EM. Most 3D structures of biological macromolecules were solved by x-ray crystallography. Some were solved by NMR spectroscopy (*nuclear magnetic resonance*) or electron crystallography. All the atomic structures are archieved in the *Brookhaven protein data bank* (PDB). These pdb files contain the coordinates of the atoms of the proteins.
The atomic coordinates and the element numbers Z are transferred to a kartesian grating with defined mesh size. The approximate electrostatical potential is proportional to the sum of element numbers in one voxel. The resulting density distribution is then folded by the effective, defocus-dependent contrast transfer function (CTF).

1.2.2 Template Recognition using Cross Correlation

To localize small references in a large spatial environment, the local correlation function (LCF) is the method of choice [75, 24]. An application for this purpose is the visualization of macromolecules with a diameter of about 25 nm in cryo-electron tomograms of cells with a length of several μm.
The correlation coefficient (CC) is a quantitative measure of similarity between two functions concerning one or several independent variables. When doing template matching in electron microscopic reconstructions the grey levels of the tomogram T, that correspond to the measured intensity, are compared with the generated grey levels of a reference R. In general, the standardized CC of two discrete functions T and R with an extension of N pixel is:

$$CC = \frac{\sum_{r=1,1,1}^{N}(T_r - \overline{T})(R_r - \overline{R})}{\sqrt{\sum_{r=1,1,1}^{N}(T_r - \overline{T})^2}\sqrt{\sum_{r=1,1,1}^{N}(R_r - \overline{R})^2}} \tag{1.2.1}$$

with $\overline{T}$ and $\overline{R}$ being the mean of the respective functions. Values of normed CC range between -1 and +1. If both functions correlate, CC values unequal zero. If the CC has a value of 1, both functions are identical at that position. If the CC is zero, the functions are independent from each other.
To circumvent a possible scale and bias difference between the voxel values in the tomogram and the reference, both functions T and R are normalized to the same scale before calculating the cross correlation function. In a first step, a bias, that is, an additive or constant background, can be removed by subtracting the respective average defined as:

$$\overline{x} = \frac{1}{N}\sum_{i=1}^{N} x_i \tag{1.2.2}$$

with N giving the number of voxels over which function x is defined.

Then an overall scale, that is, a multiplicative constant can be removed by deviding both functions by their square norm, defined as:

$$|x| = \sqrt{\frac{1}{N}\sum_{i=1}^{N}(x-\overline{x})^2} \tag{1.2.3}$$

The normalized function $\widehat{x}$ corresponding to x is then given by:

$$\widehat{x} = \frac{x-\overline{x}}{|x|} \tag{1.2.4}$$

The normalized correlation function $CC(x)$ takes the relative shift between both functions into account:

$$CC(x) = \frac{\sum_{r=1,1,1}^{N}(T_{r+x}-\overline{T})(R_r-\overline{R})}{\sqrt{\sum_{r=1,1,1}^{N}(T_r-\overline{T})^2}\sqrt{\sum_{r=1,1,1}^{N}(R_r-\overline{R})^2}} \tag{1.2.5}$$

This calculation is done most efficiently in Fourier space:

$$CC(x) = \mathcal{F}\left\{\mathcal{F}\left\{R_r\right\}\mathcal{F}^*\left\{T_r\right\}\right\} \tag{1.2.6}$$

The LCF proofs to be particularly efficient for computing the correlation of objects that differ a lot in their size ($N >> M$). The correlation is done in a defined area of size M. The LCF filters function T locally and non-linearly within the defined area $M$with a binary mask function Θ:

$$CC = \frac{\sum_{r=1,1,1}^{N}(T_r-\overline{T})\Theta_{r+x}(R_r-\overline{R})}{\sqrt{\sum_{r=1,1,1}^{N}(T_r-\overline{T})^2\Theta_{r+x}}\sqrt{\sum_{r=1,1,1}^{N}(R_r-\overline{R})^2}} \tag{1.2.7}$$

$$\Theta_{r+x} = \begin{cases} 1 & if(1,1,1) \leq r+x \leq M \\ 0 & else \end{cases}$$

Taken together, template matching requires the calculation of the locally normalized cross-correlation function for a sufficient large number of Euler rotations $\phi\theta\psi$ of the template. The maxima of the resulting cross-correlation coefficient

$$LCF_{(\phi\theta\psi)}(x) = \frac{\sum_{r=1,1,1}^{N}(T-\overline{T})R_{\phi\theta\psi}(R-\overline{R})}{\sqrt{\sum_{r=1,1,1}^{N}(T-\overline{T})^2\cdot\sum_{r=1,1,1}^{M}R_{\phi\theta\psi}(R-\overline{R})^2}} \tag{1.2.8}$$

give the most probable locations of the template. Both, the numerator and the denom-

inator can be efficiently calculated in Fourier space, resulting in one 3D function per Euler angle combination. The local peaks of this function indicate likely locations of the template in the orientation given.

The Missing Wedge Problem

Typically, tomograms are recorded with an angular range of 120°. Therefore, the information corrsponding to the other 60° is not included in the reconstruction. In Fourier space this corresponds to a wegde-like area around the positive and negative z-axis where no information is available, the so-called *missing wedge*. In ordinary space, this manifests as elongation or smearing of the object along the z-axis.
The missing wedge causes serious problems for template matching, as it distorts the shape of the observed molecules. This problem can be overcome by limiting the cross-correlation to the information outside the missing wedge.
As the unavailable information is also a volume in Fourier space, one can set the Fourier coefficients of both, the tomogram and the reference inside the missing wedge, to zero. The so-called point spread function (PSF) is the Fourier transform of the wedge function, that has the value one inside the experimentally accessible zone and zero outside it. The PSF descibes how a single bright point would appear under the influence of the missing wedge. With this, the equation

$$LCF_{(\phi\theta\psi)}(x) = \frac{\sum_{r=1,1,1}^{N}(T-\overline{T})PSF \bullet R_{\phi\theta\psi}(R-\overline{R})}{\sqrt{\sum_{r=1,1,1}^{N}(T-\overline{T})^2 \cdot \sum_{r=1,1,1}^{M} PSF \bullet R_{\phi\theta\psi}(R-\overline{R})^2}} \tag{1.2.9}$$

adapts to the fact that due to the missing wedge, different amounts of information are available in different orientations of view.

1.3 Structure Determination *in situ* by Averaging of Subtomograms

Cryo-electron tomography is a unique technique to obtain three-dimensional insights into pleiomorphic objects like cells or organelles in a close-to-native state. However, the interpretable resolution of CET is limited by the applicable electron dose. For macromolecules that occur in identical copies within one or more tomograms this limitation can be overcome by coherently averaging them. If the differently oriented and positioned particles are brought into precise register, their weak individual signals are amplified, resulting in an average that is of higher resolution.

As biological samples are extremely sensitive to radiation, a certain dose of electrons must not be exceeded. For imaging biological macromolecules faithfully, a total dose of $80\,e^-/\text{Å}^2$ is considered as limit.
This low electron dose results in a low signal-to-noise ratio (SNR) in the tomograms. Due to this, the signal of a single macromolecule does not reveal much of its substructure; the information is typically not significant above 5-10 nm resolution. However, substantially higher resolution information can be extracted by coherently averaging several copies of a molecule, thereby increasing the electron dose *in silico*. The dose-limited resolution theoretically grows as a function of the number N of averaged particles, proportional to $\sqrt{N}$ [80]. However, this equation holds only if the individual particles are brought into precise register and if they are identical. Furthermore, no missing wedge is allowed.
This means, that two procedures are necessary: an algorithm that aligns the subtomograms of the single particles to a common origin and an algorithm that classifies different subtomograms into different bins if there is a structural heterogeneity among the individual particles.

If there are N subtomograms with Pi copies of the particle, the covered particles are variously oriented and only roughly aligned at their centers after template matching.
Each single particle is rotated (specified by the Euler angles $\phi_i, \theta i$ and ψi) and subsequently translated (specified by the vectors $\Delta x_i, \Delta y_i$ and Δz_i) with respect to the coordinate system of the coherent average.
The alignment algorithm has to find the translations and rotations that align the ideally coherent Average A with respect to the particle Pi. Given the determination of these parameters, A can be obtained by applying the inverse rotations and translations.
The similarity between an individual particle and the coherent average after application of the translation vector and the Euler angles should be maximized. This similarity is described by a scoring function that has to be optimized for the refinement procedure. Thereby the missing wedge problem has to be taken into account.
Usually, one is only interested in a specific macromolecule and negative effects of any random features adjacent to the individual particles, such as membranes or other proteins should be minimized. This can be achieved by a tight mask around the particle. In addition, it is often beneficial to band-limit the correlation function [98]. Very low frequencies tend to dominate the signal of cryo-electron tomograms, in particular when an energy filter was used during imaging [33]. Low frequencies can vary due to changes of specimen thickness, whereas the very high frequencies suffer from the low SNR. The correction for the missing wedge, the masking and the band-pass filtering should be applied prior to performing the correlation.

In addition to an appropriate scoring function, an algorithm is needed to determine the translation vectors and Euler angles for those individual particles that render the maximum value of the scoring function. This function is optimized using an iterative process where the correlation function is computed for each particle and the average of the preceding run (the reference) in different orientations. The reference for the next iteration is the average of the single particles that are inversely rotated and translated, using the parameters that yielded the maximum correlation values. The entire refinement procedure must be iterated several times, typical are 10 iterations. The angular sampling for the initial iterations should be relatively coarse, e.g. 5°, and then made finer gradually. Simultaneously, a strong low-pass filter can be beneficial in the first iterations [87] and should then be gradually released to finally recover the maximum information content from the individual particles.
A prerequisite for applying the refinement procedure above is knowledge of the approximate orientations of the single particles, which can be obtained by using an initial model for alignment. However, this may bias the result by trapping the optimization process in a local maximum corresponding to the vicinity of the initial template.

1.4 The Model Organism *Spiroplasma citri*

Spiroplasma citri is a plant pathogenic bacterium that belongs to the family of Mollicutes. These are a class of microorganisms phylogenetically related to low G-C content Gram-positive bacteria [99]. They are characterized by the lack of a cell wall, a small genome size, a small number of rRNA operons and their relatively limited metabolism [5]. Mollicutes are one of the smallest, most rudimentary free-living and self-replicating procaryotic organisms that are only contained by a cholesterol-containing membrane [95]. In liquid medium, the cells form helical shapes with a diameter of 80 - 200 nm and a length of approximately 3 μm in the logarithmic growth phase up to 10 μm in stationary phase. They propagate through the medium by rotation along the longitudinal axis [13].

Plant pathogenic mollicutes are agents of several hundred diseases, affecting plants of great economic importance. They are restricted to the phloem sieve tubes and are transmitted from plant to plant by sap-feeding leafhoppers. *S. citri*, the causal agent of citrus stubborn disease, has been cultured since 1970 [77, 78]. Over the years it has become a model organism for studying the relationship of plant mollicutes with their host, the plant and the insect vector [6, 22].

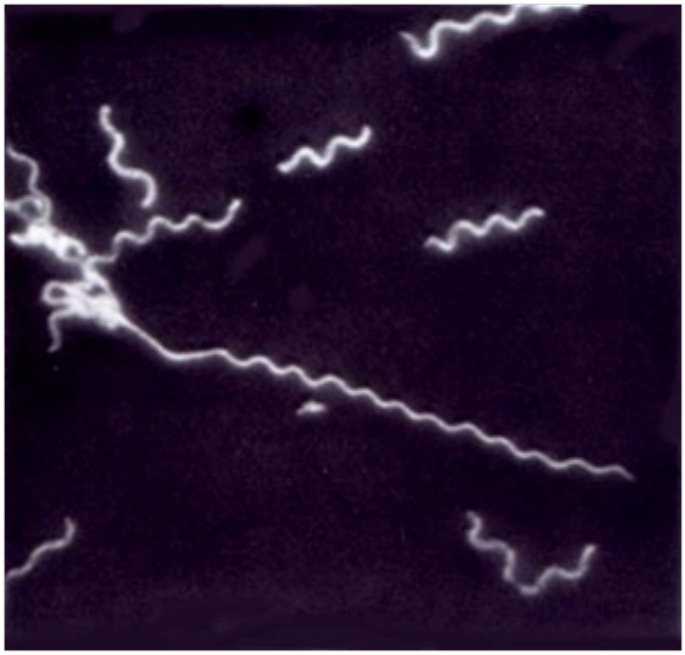

Figure 1.4.1: Darkfild micrograph of *S. citri*. From apsnet.org

The determination of the genomic sequence and the engineering of vectors for specific gene targeting allowed the studies of gene function [18, 23, 71, 43]. As homologous recombination is inefficient in *Spiroplasma*, this specific gene targeting could only be achieved by using replicative *OriC* plasmids as disruption vectors [18, 31, 71]. The construction of new gene targeting vectors for a two-step strategy with two distinct selection markers allows to screen for the rare recombination events [19]. For this approach, first transformants are screened for their resistance to gentamycin and then site-specific recombinants are selected for their resistance to tetracyclin, which can only be expressed through recombination at the target gene sequence. However, an efficient methodology for expressing foreign genes in *S. citri* has not been established yet.

On a structural basis, *Spiroplasma* got into the focus of interest because of its defined cell shape and its motility despite the lack of flagella or pili. This led to the assumption that *Mycoplasma* in general and specifically *Spiroplasma* contain cytoskeletal structures. First models were based on reports about intracellular, filamentous structures in different Mollicutes [92]. The small size and the apparently uncrowded cytoplasm make *Spiroplasma* a versatile model organism for cryo-electron tomography studies.

1.5 The Translation Process - Ribosomes

1.5.1 Protein Biosynthesis as a Central Process in Cell Biology

Protein biosynthesis is a central process in all living cells and therefore requires extensive biological machinery. It was estimated that 35 - 45 % of the genes in a theoretical minimal genome are devoted to translation [61].
A large portion of the cell's energy is invested into the process of translation. For example, fast growing *E. coli* cells spend 30 - 50 % of their energy budget on protein biosynthesis. Part of this energy is invested into the process of translation itself, another part into synthesizing the translational machinery.
As protein biosynthesis is of utmost importance for all living cells, structure, function and regulation of the translational machinery constitute central questions in biology and have been in the focus of interest of scientists for several decades.
Understanding protein biosynthesis and its regulation is also of considerable medical interest. Translation is for example inhibited by 70 % of the natural occurring antibiotics [86]. Expanding our knowledge about translation therefore not only serves to answer fundamental questions, but it enables the further characterization of a prime drug target.

1.5.2 The Ribosome

The ribosome is one of the biggest and most complex macromolecular machines known. Ribosomes comprise ribosomal RNA (rRNA) and proteins and are generally organized into two subunits that are characterized by their sedimentation coefficient: The 30S small subunit and the 50S large subunit. Together they form the 70S ribosome. The 30S subunit consists of 16 S rRNA (1542 nt) and 21 different proteins, while the 50S subunit contains 23 S rRNA (2904 nt) and 33 different proteins.

The two techniques that have been most important in providing structural information about the ribosome are cryo-electron microscopy and x-ray crystallography. 3D density maps obtained by single particle cryo-electron microscopy were published since 1991 and nowadays reach a resolution of 8 - 12 Å. The 30S subunit from *Thermus thermophilus* [90, 102] and the 50S subunit from *Haloarcula marismortui* [2] and *Deinococcus radiodurans* [39] were solved at atomic resolution by x-ray crystallography.

The 30S Subunit at Atomic Resolution

The atomic model of the *T. thermophilus* 30S subunit [102] shows a distinct organization into four morphological units earlier recognized in cryo-electron microscopy reconstructions [25, 50], referred to as head, body, shoulder and platform, that closely correspond to the four domains of the 16 S rRNA tertiary structure.

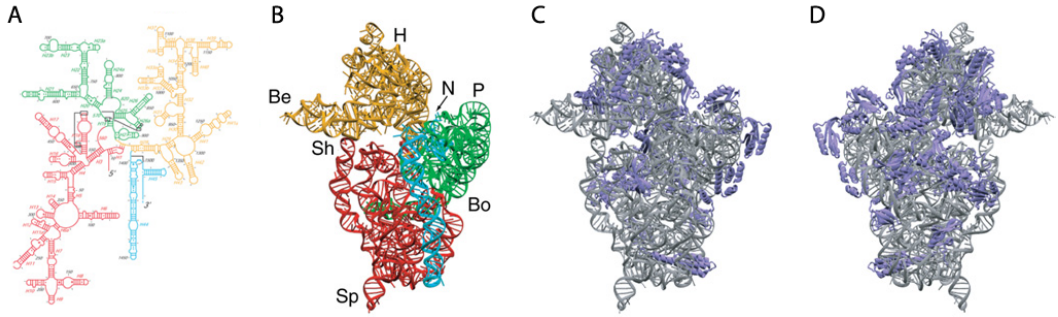

Figure 1.5.1: The structure of the small ribosomal subunit from *T. thermophilus*. A) secondary structure with the principal domains indicated by different colors. B) X-ray crystal structure of 16 S RNA, with the domains colored as in A). C) and D) Front and back view of the complete x-ray structure, with both RNA and proteins. Landmarks: Be, beak; Bo, body; H, head; N, neck; P, platform; Sh, shoulder; Sp, spur (From [102]).

A long helix, helix 44, runs along most of the body of the subunit on the intersubunit face, its top forming the part of the decoding center. Both, shoulder and platform domains, form intermitted contacts with the head, creating channels through which the mRNA can pass. At the solvent side of the entrance channel, a triangular arrangement of three proteins, S3, S4 and S5 is reasonable for unwinding mRNA to prepare it for single-strand presentation at the decoding site.

The 50S Subunit at Atomic Resolution

The atomic model of the 50S subunit shows a compact, monolithic structure with three protrusions (figure 1.5.3). The first protrusion is the mushroom-shaped L1-stalk, whose stem is formed by a pair of RNA helices and whose head is formed by two components: a globular rRNA element and protein L1, which is the largest protein of the whole subunit. This stalk is highly flexible and involved in the tRNA translocation process [97]. The second, middle protrusion is the so-called central protuberance, formed by 5 S RNA and proteins L5 and L27. This component is instrumental in defining and fine-tuning

the relative position of the 30S subunit through bridges connecting to the 30S subunit head. The third protrusion, on the right side, is formed by proteins L10 and L7/L12 and is highly mobile, such that it eludes definition in x-ray maps. The base of the L7/L12 stalk is the site of factor interaction and GTPase-associated activity of the ribosome. It is composed of protein L10 and a component known as the GTPase-associated center (GAC). The latter is composed of protein L11 and a 58-nucleotide rRNA segment.

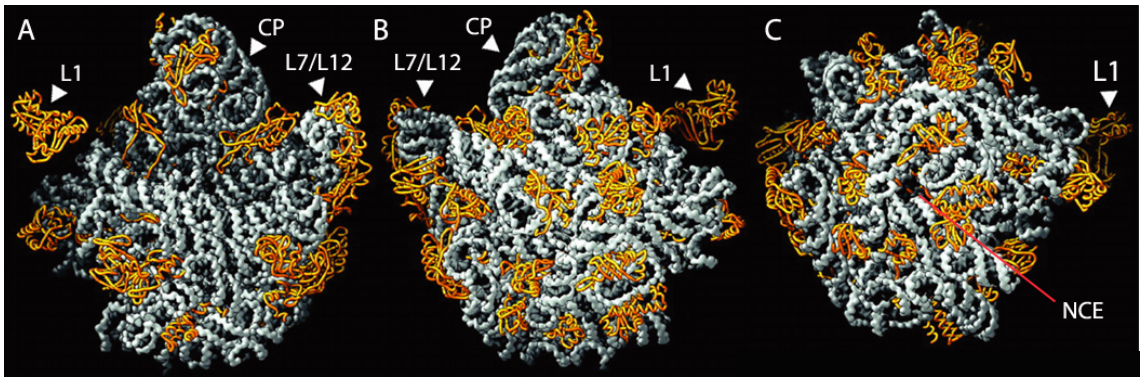

Figure 1.5.2: The structure of the large subunit of *H. marismortui* at atomic resolution. Proteins are shown in yellow. A) Schuwirth orientation front B) Schuwirth orientation back, C) Bottom view. L1, L1-stalk; CP, central protuberance; L7/L12, L7/L12-stalk; NCE, nascent chain exit tunnel. Adapted from [2].

Another defining feature of the 50S subunit is the polypeptide exit tunnel, a tunnel of approximately 100 Å length running through the core of the subunit, from the peptidyl-transferase center to the polypeptide exit site on the subunit's solvent side. The average width of the tunnel is 15 Å, starting with a narrower passage in its upper part. Tails of two proteins, L4 and L22, , whose globular parts flank the exit site, line a segment of the exit tunnel and are thought to function as a gate [44, 64, 94].

The Assembled 70S Ribosome

As the structure of the subunits is known, the most important questions on the structure of the whole ribosome remaining, are the relative orientation of the subunits to each other, potential conformational changes upon association and the nature of interactions between the subunits.
The orientation of the subunits is such that the head of the 30S subunit faces the central protuberance of the 50S subunit. The joining of the subunits creates a solvent-accessible

intersubunit space, large enough to accommodate approximately three tRNAs [25]. Importantly, this space is shaped such that it accommodates the L-profile of a tRNA molecule. Here, protein biosynthesis occurs.
The ribosomal subunits are connected by several well defined intersubunit bridges. There are 20 central bridges [9, 104] mostly formed by RNA - RNA contacts. RNA - protein or protein - protein contacts mostly occur at peripheral locations, where flexibility is required to accommodate the conformational rearrangement between the small and the large subunit.

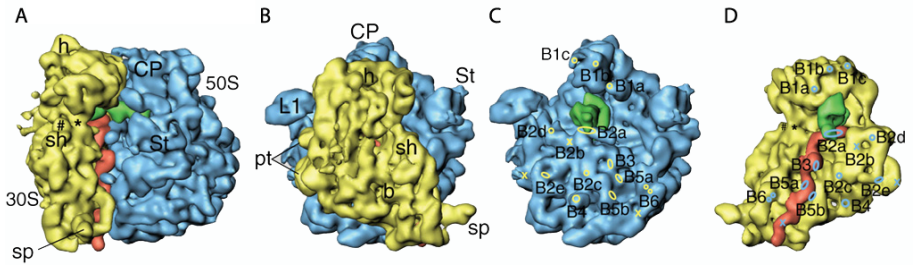

Figure 1.5.3: Cryo-EM structure of the 70S ribosome from *E. coli* at 11.5 Å resolution. A) side view, with helix 44 of 16 S RNA in orange, P-site tRNA in green. B) View from the solvent side from the 30S subunit. C) Same view, with 30S subunit removed. D) Opposite view, with 50S subunit removed. Landmarks: sp, spur; pt, platform; sh, shoulder; h, head; b, body; St, L7/L12 stalk; CP, central protuberance; L1, L1 stalk; (C) and (D) show designations of intersubunit bridges. From [28].

The Path of the mRNA

During initiation of protein biosynthesis, mRNA associates with the small ribosomal subunit, binding to a 6-nucleotide stretch in the 5' region to a complementary segment of the 16 S RNA, the Shine-Dalgarno sequence [84]. This interaction, probably with the assistance of S1, provides the correct registration of the initiator codon in the subunits P site which is required for the binding of the initiator tRNA. In the fully assembled ribosome, the mRNA goes through a channel formed between shoulder and head of the small subunit [25], curves around the neck in the cleft region to form a U-turn [83] and exits through a channel formed between platform and head. Both, entrance and exit channels are formed by mobile, ribosomal RNA elements.

The Exit Path of the Nascent Polypeptide

The nascent polypeptide, also called nascent chain, exits the large subunit through a long (approximately 100 Å) tunnel, which runs from the peptidyl-transferase center to a

point at the back of the subunit. The tunnel starts in a 30 Å wide funnel-shaped cavity formed entirely by RNA, the peptidyl-transferase center. In its subsequent narrower segment, the width of the tunnel varies between 15 Å and 10 Å, allowing the polypeptide to prefold into alpha-helical, but unlikely globular forms [55]. Much of the length of the tunnel is formed by RNA, however, a segment immediately below the peptidyl-transferase center is lined with protein. This segment undergoes conformational changes during the elongation cycle [28], which could have the purpose of gating or actively promoting the passage of the polypeptide.

1.6 The Protein Degradation Machinery - Proteasome and TPPII

Cellular proteins are in a dynamic state of constant renewal - they are beeing synthesized and degraded continuously. Protein degradation in the cytosol is a regulated process and it is involved in controlling a broad array of biological processes, such as transcription, DNA repair and protein quality control. Two proteolytic proteins were chosen as model proteins for heterologous expression in *Spiroplasma citri*; the 20S proteasome from *Thermoplasma acidophilum* for its stability and addiction to assemble and Tripeptidyl Peptidase II (TPPII) for its characteristic size and shape.
Expressing proteins in a host as thin as *S. citri* makes it possible to investigate not only single protein structures in a cellular environment but also protein interactions of fragile complexes if two or more proteins are co-expressed.

1.6.1 The 20S Proteasome from *T. acidophilum*

The 20S proteasome is a high-molecular multi-catalytic enzyme complex with a molecular weight of 700 kDa, which is ubiquitous in eukaryotes and archea [88]. In bacteria the proteasome is rare and non-essential [46]. The molecular architecture of the 20S proteasome is highly conserved from Archaea to human with increasing complexity of the subunit composition. The *T. acidophilum* enzyme consists only two types of subunits, namely α and β.
The 28 subunits of the *T. acidophilum* 20S proteasome form a cylinder of 14.8 nm length, consisting of four rings with seven-fold symmetry and a diameter of 11.3 nm [68] (figure 1.6.1). Immuno-electronmicroscopical experiments showed that the outer rings consist of α-subunits while the inner rings consist of β-subunits [35] (figure 1.6.1**A** and **B**).
The x-ray structure was solved in 1995 by Löwe *et al.* [57].

1.6.2 Tripeptidyl Peptidase II

TPPII was classified as serin protease of the subtilisin type [85]. The 3D structure of the TPPII complex of *Drosophila melanogaster* has been intensively studied by single particle electron microscopy and has been resolved to a resolution of 2.2 nm [74]. It assembles into a 6 MDa complex of 60 x 28 nm. The spindle-shaped homo-oligomer is composed of two twisted strands, each containing 10 segments. Each segment is composed of two, head-to-head oriented monomers of 150 kDa (figure 1.6.1**C** and **D**).
TPPII has so far been isolated from *Drosophila* larvae or heterologously expressed in and isolated from *E. coli*, but the structure of the protein in the cellular environment has not as yet been studied.

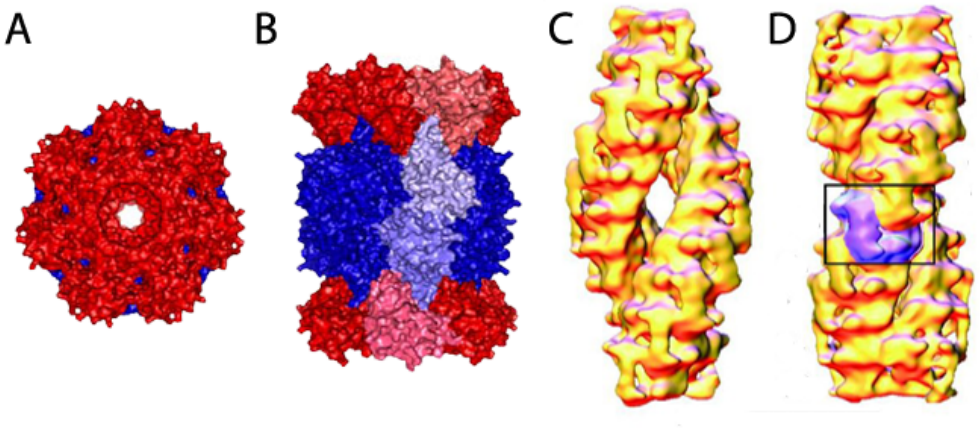

Figure 1.6.1: Structure of the 20S proteasome from *T. acidophilum* and TPPII from *D. melanogaster*. a) 20S proteasome top-view b) 20S proteasome side-view. c) and d) TPPII spindle side-view in two different orientations. From [74]. Proteins are not to scale.

1.7 The Aims of this Work

The structure and function of macromolecules, for example the ribosome, have been a major focus of interest for scientists in the last decades. The solution of structures by X-ray crystallography and cryo-electron microscopy of purified samples have been milestones in ribosome research. However, little is known about the behavior of ribosomes in their natural environment, the highly crowded cytoplasm.
When aiming at a better understanding of the function of these ribonucleoproteins, it is important to explore their cellular distribution *in vivo*. One aim of the cellular identification of ribosomes at a molecular level is the identification of interactions with other

macromolecules. Therefore, we aim at 3D ribosome atlases of *S. citri* cells during different growth states that contain information about the spatial orientation and distribution of ribosomes in intact cells. In the focus of interest is the distribution pattern of ribosomes under changing cellular conditions and possible ribosome - ribosome interactions. The 3D averaging of subtomograms of identified ribosomes allows the retrieval of novel structural information.

Moreover, we aim at providing genetic tools for the manipulation of *Spiroplasma citri* to express foreign genes heterologously and to label endogenous proteins fluorescently. Expressing foreign genes in an organism that is highly suited for cellular electron tomography would enable us to study protein structures in a cellular environment without purification. Moreover, protein interactions of fragile protein complexes could be studied if two proteins are co-expressed.

So far, there is no technique established that could independently varify the results obtained by template matching. As described, template matching is a very powerful technique, but it is influenced by factors like sample thickness, tilt angle or the missing wedge. Therefore, it is a useful methodological approach to establish a system of fluorescently labelled proteins that enables the validation of the template matching. Ribosomes, again, are well-suited model proteins for this purpose, as they are big and show a high contrast in the electron microscope due to their RNA content. The ribosomes are to be tagged with a fluorescent marker on genome level, to obtain a 100 % coverage of fluorescent labelling. The distribution pattern of ribosomes studied by fluorescence microscopy can then be correlated to the distribution information obtained by template matching. Hence, fluorescently labeled protein complexes might enable a correlative localization approach using fluorescence microscopy and electron tomography.

2 Electron Tomography

2.1 Transmission Electron Microscopy

2.1.1 Parts and Function

The TEM was first developed by Ernst Ruska [76] in the early 30's based on the same optical principles as a light microscope but using electrons as source of illumination and electromagnetic lenses.
The electrons are generated and accelerated in a field emission gun (FEG) which produces a highly coherent, intense beam. Below the extraction anode is a small electrostatic lens. This so-called gun lens positions the first cross-over of the electron beam. The beam has to be formed into an even, parallel illumination which is achieved by aligning the beam-defining apertures accordingly. Parallel illumination is important for producing high-quality micrographs, as otherwise defocus and magnification variations occur. Usually a two-condenser system is used, where condenser 1 (C1) controls the spot size of the beam and condenser 2 (C2) controls the intensity (size) of the beam.
After passing the specimen, where part of the electrons interact with the atoms of the sample, the image is magnified and focused by the objective lens. Electrons that are highly scattered are blanked by the objective aperture, which is situated directly underneath the objective lens, and thereby the image contrast is enhanced. The projection system consists of a set of lenses that is used to further magnify the image of the specimen and to project it to the detector.
The microscope is equipped with three sets of double deflection coils, gun, beam (above the objective lens) and the image deflection coils (below the objective). Deflection coils play an essential role in the alignment of the microscope and are used for aligning the gun, beam, objective lens, magnification system and detector alignments.
See figure 2.1.1 for an illustration of the optical path of the electron microscope.

2.1.2 Contrast Formation in the Electron Microscope

The basis of image formation in the electron microscope is the interaction of the electrons with the object. Three sorts of contrasts are known in electron microscopy: phase,

amplitude and scattering absorbtion contrast. Phase and amplitude contrast are based on the wave character of the electrons and are described by wave optics. Imaging in the electron microscope can be approximately described as multiplication in Fourier space of the scattered wave and a function c that describes the imaging characteristics of the optical system.

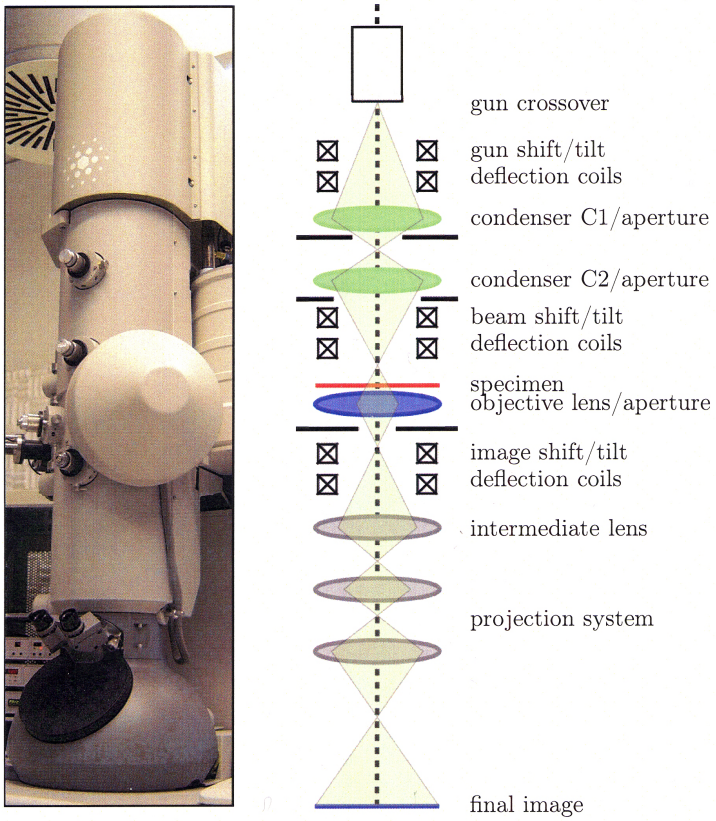

Figure 2.1.1: Optical path of an electron microscope. Depicted is a two condenser system (Tecnai F30 'Polara', FEI Company, Eindhoven, The Netherlands).

One of theses characteristics is described as contrast transfer function (CTF), which describes the property of the objective lens. The phase of elastically scattered electrons is shifted by $90\,^\circ$ ($\pi/2$) compared to the unscattered electrons. As result, a pure phase object that is imaged with an ideal lense is invisible. Electromagnetic lenses are by far not ideal but they prolong the optical path of the passing waves, which results in a phase shifting. Causal for this phase shifting is the spherical aberration and the defocussing of the objective lens. The phase contrast is maximized if there is an additional phase shifting of the scattering wave of $\pm\frac{\pi}{2}$.
Since the amplitude CTF is near 1 at low frequencies, the defocus can be adjusted close

to zero, still having sufficient contrast. The focus value that provides maximal frequency response is defined as

$$\Delta f_{Sch} = -1.2 \cdot \sqrt{C_s \cdot \lambda} \tag{2.1.1}$$

and is called Scherzer focus [82]. In case of an acceleration voltage of 300 keV the wavelength of the electrons is $\lambda = 1.97\,pm, \Delta f_{Sch} = -75\,nm$. At this defocus value the position of the first zero-crossing of the CFT is at maximal frequency, therefore maximizing the micrography information content.
In practise, low-dose biological samples under cryo-conditions are very sensitive to beam damage, resulting in a very low SNR. They are 'weak phase objects'. Their exit wave phase shift is small and the amplitude contrast is only about 7 % of the total contrast [91]. To increase the contrast, the defocus can be increased by adjusting the excitation of the objective lens at the expense of diminishing the higher frequency information. So one has to trade off carefully resolution against contrast and chose the working defocus accordingly. If the CFT can be corrected by phase flipping, the information that can be drawn from the micrograph is nearly doubled. The Scherzer focus theoretically gives the highest resolution, but the corresponding contrast is too low in practice. Especially as cellular tomography usually does not resolve data behind the second or third zero point of the CFT a focus of ~4 to -8 μm is preferred.

2.1.3 Energy Filtering

As inelastic scattering events become more frequent with increasing object thickness, the size of the sample limits the contrast in the acquired micrographs. The spheric aberration causes a smearing of the focus plane by scattering inelastically and multiply scattered electrons in different focus layers.
The mean free path of inelastically scattered electrons is in the range of 100 nm to 250 nm for voltages of 120 keV to 300 keV [21, 33]. Those electrons have lost kinetic energy by the scattering event and lead to a blurring of the image due to the chromatic aberrations of the lenses [11].
Energy filters are spectroscopic devices that are able to filter electrons according to their certain kinetic energy. They are available as in-column or post-column versions. To reduce the effect of chromatic aberrations only electrons that have a kinetic energy close to the primary energy are allowed to pass the filter. This is called zero-loss peak filtering [32]. Since inelastically scattered electrons add random noise to the image, energy filtering can also increase the SNR of the micrographs.

2.2 Cryo-electron Tomography

2.2.1 The projection theorem

The projection theorem, which is of fundamental importance in the attempts to recover 3D objects from 2D projections, implies that the projection of a two-dimensional function $f(x, y)$ can be obtained as the inverse one-dimensional Fourier transform of a central section through its 2D Fourier transform $\mathcal{F}[f(x, y)]$. An analogous relationship holds between the projection of a three-dimensional object and the corresponding central section of its 3D Fourier transform. This means that reconstruction can be achieved by filling the 3D Fourier space with data on 2D central planes that are derived from the projections by 2D Fourier transformation (figure 2.2.1). Varying the projection direction by tilting the specimen, results in a number of central sections which can be combined to the ultimate 3D information.

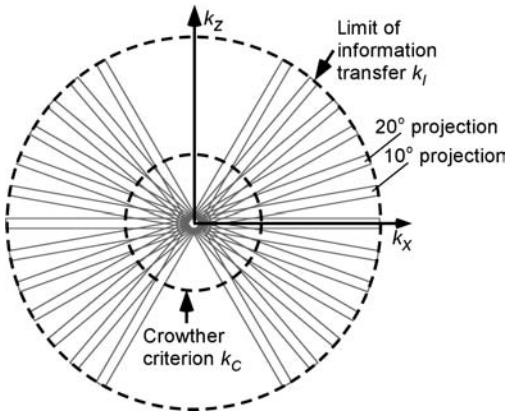

Figure 2.2.1: Data sampling in Fourier space. A projection of an object with thickness d corresponds to a central slice of thickness 1/d in Fourier space. Therefore, the three-dimensional information of the specimen (outside of the missing wedge) is gathered homogeneously up to frequency k_C (Crowther criterion).

Crowther *et al.* [12] derived a criteria for the maximum 3D resolution r of a tomographic reconstruction based on the size D of a spherical object and the number of projections N that must be distributed over the full tilt range. For a tomographic single-axis tilt series with angular increment of $\Delta\alpha = \pi/N$ r is defined as

$$r = \frac{\pi \cdot D}{N} = \Delta\alpha \cdot D. \tag{2.2.1}$$

This equation assumes a complete tilt series. Hitherto, for a limited tilt range there can

be just an estimation for the upper limit.

2.2.2 Alignment of Projections

Alignment is initially understood as an operation that is performed on two or more images with the aim of bringing a common motif into register. In case of tomographic data, the translations of different projections relative to each other are determined. We use a reference-based alignment method [36, 54, 89] based on 10 nm colloidal gold markers that are applied to the grid together with the specimen. The position of these marker points are marked manually and compared to the coordinates of a model. Based on this information, an alignment model is calculated and the pixel error between predicted and real coordinated is minimized. Subsequently, the data is reconstructed with a suitable reconstruction method.

2.2.3 Tomographic Reconstruction

The most common method for reconstructiong tomographic data is the weighted back projection [69, 38]. This method can be applied to arbitrary tilt geometries and it executes the back projection in real space, while the mathematical preparation of the single projections is done in Fourier space. Back-projection is an operation that is the inverse to projection: while the projection operation produces a 2D image of the 3D object, back projection 'smears out' a 2D image to a 3D volume (figure 2.2.2), which is called back-projection body [41], by translation into the direction perpendicular to the original projection direction.

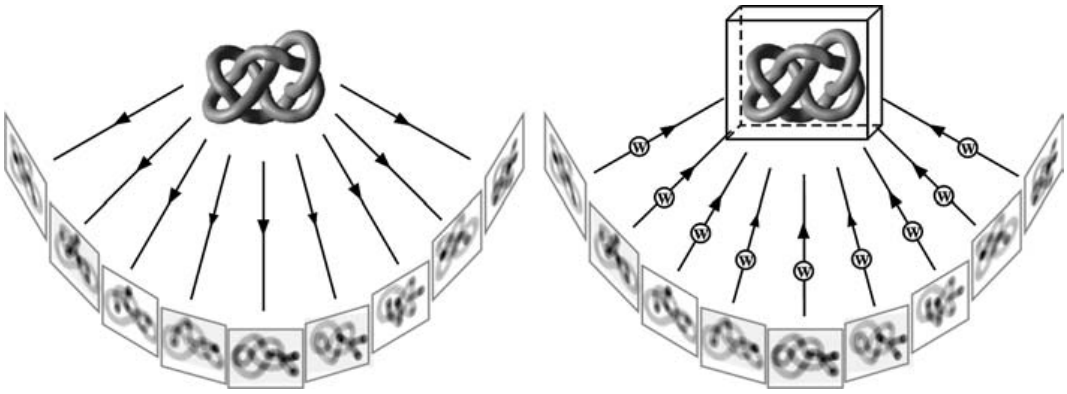

Figure 2.2.2: The principle of tomographic reconstruction. Imaging the specimen under different tilt angles gives several single projections. Back-projecting these projections with a suited algorithm results in the reconstructed 3D volume.

Combining the single back-projection bodies to a common volume without weighting them results in a blurred version of the object. This is due to the fact that low frequencies are overemphasized in the 3D reconstruction because the single central parts of the projections overlap in the region around the origin. The density of sampling points decreases with increasing spatial frequency.
Multiplication with a suitable radius-dependent weight is necessary to restore the correct balance in Fourier space. Prior to reconstruction, the projections are weighted with the distance to the center, so that high frequencies are enhanced. This kind of weighting is called analytical. If the precise diameter of the sample is known, one can also apply an exact weighting, based on the spherical or cylindrical shape of the object [41].

2.2.4 Limitations of Electron Tomography

The holder that was used for taking tomograms for this work with the FEI Tecnai 'Polara' can be tilted to a maximum of $\pm 60\,^{\circ}$ as recommended by the manufacturer. The missing projections at the high tilt angles result in a double wedge of missing information in Fourier space (figure 2.2.3), the so called missing wedge (see section 1.2.2).

Figure 2.2.3: The missing wedge. Influence of the tilt geometry on the 3D reconstruction. Adapted from [56]

In the tomographic recontruction in real space, this leads to an elongation of the structural information along the z-axis. If one uses a double-axis holder, that enables to rotate the specimen inside the holder by $90\,^{\circ}$ in its x-y plane between the acquisition of two tilt series, the missing wedge is reduced to a missing cone. But aligning the two corresponding tilt series turned out to be challenging due to sample movement.

3 Materials & Methods

3.1 Cryo-electron Tomography

3.1.1 Sample Preparation

Growing and Harvesting *S. citri*

S. citri wild type cells were grown in 2 ml liquid SP4 medium using cryo tubes (Nunc). The standard cultivation cycle starts a new passage every 48 h by transferring 200 μl old culture to 1.8 ml fresh medium. Cultures were incubated at 32 °C. For the different growth states cells were harvested by cetrifugation at 20 000 g for 10 min at room temperature after 4 h, 72 h or 120 h. After discarding the supernatant, the cell pellet was resuspended in 400 ml HSO buffer. After a second centrifugation step at 20 000 g for 5 min at room temperature, the pellet was then resuspended carefully in 60 μl HSO buffer. Subsequent plunge freezing was applied immediately.

Plunge-Freezing

As sample slides, molybdenum grids with lacey carbon film, 200 x 200 mesh were used. The carbon film was glow discharged for 30 sec to enhance settling of the sample on the grid. 3 μl 10 nm colloidal gold (Sigma) were put on the grids and let dry completely prior to sample assignation. 3.5 μl cell suspension were applied to the grid and the grid was immediately clamped into the plunge freezer (FEI). Overstanding liquid was blottet with filter paper (Whatman No. 50) from the back, before plunging the grid into liquid ethane. The grids were then transferred under nitogen atmosphere to a grid box and were subsequently stored in liquid nitrogen until further use.

3.1.2 Data Acquisition and Reconstruction

Tomograms of *S. citri* cells were acquired using a FEI Tecnai F30 microscope (Polara) operated at 300 kV and equipped with a Gatan post-column energy filter and a 2k x 2k CCD camera. The magnification on the fluorescence screen was set to 27 500 x resulting

in an object pixel size of 4.68 p/Å. The tomogams were acquired with the TOM[2] package[1]with a nominal defocus between 4 and 10 μm using a tilt range of -60° to 60° in steps of 2°. The images were filtered around zero-loss peak with a slit width of 20 eV. The exposure time was set using a cosine scheme to adapt to the increasing sample thickness at higher tilt angles. The total dose on the sample was $< 80e^{-}/Å^{2}$. The single projections were aligned by manual selection of marker points (tom_setmark) and aligned on a common origin. 3D reconstruction was done using the weighted back projection algorithm (tom_Rec3dGUI.m).

3.1.3 Template matching

For the detection of 70S ribosomes in the recorded tomograms, downsampled reconstructed volumes (binning factor two, resulting in an object pixel size of 1,872 nm/pixel) were cross-correlated with a template structure using the program MOLMATCH. The template was generated from 3.5 Å crystal structures of the *E. coli* ribosome (PDB entries 2AW7 and 2AWB) by adjusting the pixel size and bandpass filtering to 5 nm. The local correlation function (LCF) was calculated by rotating the template over all Euler angels with 10 ° increments. The 300 particles with the highest CCC were selected and the information about 3D coordinates (x, y and z) and Euler angles (Ψ, Θ, Φ) describing the relative orientation of the particles, was stored.

3.1.4 Averaging and Classification of subtomograms

Selected particles were reconstructed in subtomograms with full resolution and 3D aligned against an average of all particles. Particle classification was performed using constraint-correlation.

3.2 Molecular Cloning

3.2.1 Strains

E. coli host strains

Chemically competent *E. coli* strains DH5α (Novagene) and Top10 (Invitrogen) were used for cloning. Strain BL21(DE3) (Invitrogen) was used for protein expression in *E. coli*.

[1]This program was developed by Andreas Korinek

3.2.2 Primers

Primers for amplifying GFP with RBS with different distances to Shine-Dalgarno motif

name	sequence
GFP_16sRBS_for	5' - CTAACTAGCTAGGATCCAAAAGGAGAAGAGTAAGAGATGGGTAAAGGAGAAGAAC - 3'
GFP_10sRBS_for	5' - CTAACTAGCTAGCTAGAAAGGAGAAGAGTAAGAATGGGTAAAGGAGAAG - 3'
GFP_6sRBS_for	5' - CTAACTAGCTAGCTAGAAAGGAGAAGAGTATGGGTAAAGGAGAAG - 3'
GFP_4sRBS_for	5' - CTAACTAGCTAGCTAGAAAGGAGAAGAATGGGTAAAGGAGAAG - 3'
GFP_Nhe_rev	5' - GTGGATCCTTAGCTAGCACCCTTGTATAG - 3'

Primers for inserting a NheI and a NotI Site to the MCS of pSD4

name	sequence
pSD4_casette_for	5' - CTCTAGAGGATCCCCGGGTACCG - 3'
pSD4_casette_rev	5' - CGTAGGCCCACTACGTGAACCATC - 3'
pSD4_NheI	5' - GAATTCGCCCGCTAGCGAGTCGTATTAC - 3'
pSD4_NotI	5' - GTATTACAATTCAGCGGCCGCCGTTTTACAAC - 3'

Primers for changing the RBS of the Proteasome α Subunit by Quick Change

name	sequence
TA_RBS_alpha_for	5' - CCAGCTGCAGATTATAGTGGAGAAAGGAGATAACATGCAACAGGCC - 3'
TA_RBS_alpha_rev	5' - GGCCTGTTGCATGTTATCTCCTTTCTCCACTATAATCTGCAGCTGG - 3'

Primers for amplifying GFP, Proteasome and TPPII with RBS for Insertion into pSD4

name	sequence
TPPII_NheI_for	5' - TAGCTAGCTGAAAAGGAGAAGAGTAAGAGAGTC GATGGCCACCAGCGGTATTGTCGAG - 3'
TPPII_NotI_rev	5' - CTGCGGCCGCAGTTAGAACAAACGGAAGCTGCT GGG - 3'
GFP_NheI_for	5' - TAGCTAGCTGAAAAGGAGAAGAGTAAGAGAGTC GATGGGTAAAGGAGAAGAAC - 3'
GFP_NotI_rev	5' - GTGCGGCCGCAGTTAGCTAGCACCCTTGTATAG - 3'
TAprotea_Nhe_for	5' - TAGCATAGCTAGCTGAAAAGGAGAAGAGTAAGA GAGTCGATGAATCAGACTTTAGAAACTGGTACAAC - 3'
TAprotea_Not_rev	5' - CTAGATAGCGGCCGCAGTTAGAGGAATTTTTTA ACTTCCTCCTGATCG - 3'

Primers for designing the new Vector pFP

name	sequence
QCpSD4ΔPst_for	5' - GCTTGCATGCCAGCAGTTCAGATCTTTATATAAC - 3'
QCpSD4ΔPst_rev	5' - GTTATATAAAGATCTGAACTGCTGGCATGCAAGC - 3'
Pst_OriCs_for	5' - CATCGTACTGCAGGGAAGATAGCACATTATTTTCC - 3'
OriCs_Xba_rev	5' - CATCGTATCTAGATTTTACTCCTTACTTTAG - 3'
Bgl_fruO_for	5' - CATGCTAAGATCTAAGCTTTTACACAAATGC - 3'
fruO_Kpn_rev	5' - CATCGTAGGTACCCTATGAACTTGTAATAATTTG - 3'
Bgl_Pspi_for	5' - CATCGTAAGATCTAATTAAAAGTTAGTGAAC - 3'
Pspi_Kpn_rev	5' - CATGCTAGGTACCTATATTTCCTTTCTC - 3'
Kpn_MCSpFP_Eco	5' - CATGCTAGGTACCGCTAGCATATGTCGACTAGTC TCGAGGGCCCATGGCGGCCGCGGATCCGAATTC CATCGTA - 3'
Eco_MCS_Kpn_rev	5' - TACGATGGAATTCGGATCCGCGGCCGCCATGGGC CCTCGAGACTAGTCGACATATGCTAGCGGTAC CTAGCATG - 3'

Primers for adding a 12 Amino Acid Linker to FbFP flanked by NheI

name	sequence
L4_Bs1_for	5' - GAAGCTGCTGCTGCTAGTTTTCAATC - 3'
L4_Bs2_for	5' - GAAGCTGCTGCTGCGTCGTTCCAGTC - 3'
L4_Pp1_for	5' - GAAGCTGCTGCTATCAACGCAAAACTC - 3'
L8_FbFP_for	5' - GCTGGTGCTGGTGAAGCTGCTGCT - 3'
Nhe_L12_FbFP_for	5' - CATCATAGCTAGCGCTGCTTCCGCTGCTGGTGCT - 3'
Bs1_Nhe_rev	5' - CATCATAGCTAGCTTACATAATCGGAAGC - 3'
Bs2_Nhe_rev	5' - CATCATAGCTAGCTTACTCGAGCAGCTTTTC - 3'
Pp1_Nhe_rev	5' - CATCATAGCTAGCTTAGTGCTTGGCCTGGC - 3'

Primers for Amplifying Genomic Sequences for Insertation into pGOT

gene	sequence
L1	5' - CATGCTATCTGGATCCTAACAAATAGCAAGGAAGCT - 3'
	5' - CTTTTGGATCCGCTAGCTAATTCAATTAAAACTTTAATTC - 3'
L29	5' - CATGCTAGGGATCCATGAATGATTTAACCAAAAAA CAG - 3'
	5' - CATGCTACGGATCCGCTAGCTTATTTTTTTCCTGTCCCTTTC - 3'
FtsZ	5' - CATGCTAGGATCCATGGACAATTTTGATAATTATG - 3'
	5' - CATGCTAAGATCTGCTAGCTCAACTACGACGAACAAATGG - 3'
MreB	5' - CATGCTAGGATCCATGGCCATATTTAATAATAAG - 3'
	5' - CATGCTAAGATCTGCTAGCCTAATTCTTTTGTTTTATG - 3'
ParA	5' - CATCGTAGGATCCATGGGAAAAATTATTGCAATC - 3'
	5' - CATCGTAAGATCTGCTAGCCTCGCCATTGTTTGCC - 3'
Spiralin	5' - CATCGTAGGATCCATGAAAAAACTTTTATCG - 3'
	5' - CATGCTAAGATCTGCTAGCTCCTGCATTTGCTG - 3'
GroEL	5' - CATCGTAGGATCCATGTCAAAATCAATTAAATTTGC - 3'
	5' - CATCGTAAGATCTGCTAGCTTTTTCTAAAATTGGTAG - 3'

3.2.3 Vectors

Expression Vectors

Plasmid	**Marker**	**Description**	*Reference*
pSD4	AmpR, tetM	empty expression vector with dnaN promotor	Duret, 2003
pSD4_6GFP	AmpR, tetM	vector with GFP 6 bps downstream of the Shine-Dalgarno-Sequence	this work
pSD4_10GFP	AmpR, tetM	vector with GFP 10 bps downstream of the Shine-Dalgarno-Sequence	this work
pSD4_16GFP	AmpR, tetM	vector with GFP 16 bps downstream of the Shine-Dalgarno-Sequence	this work
pSpP	AmpR, tetM	empty expression vector with Spiralin promotor	this work
pSpP_6GFP	AmpR, tetM	vector with GFP 6 bps downstream of the Shine-Dalgarno-Sequence	this work
pSpP_10GFP	AmpR, tetM	vector with GFP 10 bps downstream of the Shine-Dalgarno-Sequence	this work
pSpP_16GFP	AmpR, tetM	vector with GFP 16 bps downstream of the Shine-Dalgarno-Sequence	this work
pFP1	AmpR, tetM	empty expression vector with InfB promotor	this work
pFP2	AmpR, tetM	empty expression vector with FruR promotor	this work
pSP	AmpR, tetM	optimized vector with Spiralin promotor	this work

Integration Vectors

Plasmid	**Marker**	**Description**	*Reference*
pGOT1	gen, tetM, AmpR	empty vector that is designed to integrate into the genome	Reaudin, 2005
pGOT_L1	gen, tetM, AmpR	vector with truncated sequence of ribosomal subunit L1	this work
pGOT_L1_GFP	gen, tetM, AmpR	vector with GFP fused to truncated L1 sequence by a 12 aa linker	this work
pGOT_L1_Bs1	gen, tetM, AmpR	vector with FbFP variant Bs1 fused to truncated L1 sequence by a 12 aa linker	this work
pGOT_L29	gen, tetM, AmpR	vector with full length sequence of ribosomal subunit L29	this work
pGOT_L29_GFP	gen, tetM, AmpR	vector with GFP fused to L29 sequence by a 12 aa linker	this work
pGOT_L29_Bs1	gen, tetM, AmpR	vector with FbFP variant Bs1 fused to L29 sequence by a 12 aa linker	this work
pGOT_FtsZ	gen, tetM, AmpR	vector with full length sequence of FtsZ	this work
pGOT_ParA	gen, tetM, AmpR	vector with full length sequence of ParA	this work
pGOT_MreB	gen, tetM, AmpR	vector with full length sequence of MreB	this work
pGOT_Spi	gen, tetM, AmpR	vector with full length sequence of Spralin	this work
pGOT_GroL	gen, tetM, AmpR	vector with full length sequence of GroEL	this work
pGOT_FtsZ_GFP	gen, tetM, AmpR	vector with GFP fused to FtsZ sequence by a 12 aa linker	this work
pGOT_FtsZ_Bs1	gen, tetM, AmpR	vector with FbFP variant Bs1 fused to FtsZ sequence by a 12 aa linker	this work
pGOT_ParA_Bs1	gen, tetM, AmpR	vector with FbFP variant Bs1 fused to ParA sequence by a 12 aa linker	this work
pGOT_MreB_Bs1	gen, tetM, AmpR	vector with FbFP variant Bs1 fused to MreB sequence by a 12 aa linker	this work
pGOT_Spi_Bs1	gen, tetM, AmpR	vector with FbFP variant Bs1 fused to Spiralin sequence by a 12 aa linker	this work
pGOT_GroL_Bs1	gen, tetM, AmpR	vector with FbFP variant Bs1 fused to GroEL sequence by a 12 aa linker	this work

3.2.4 Enzymes, Antibodies and Kits

Enzymes

EcoRI Fast Digest(20 U/μl)	Fermentas
BamHI Fast Digest(20 U/μl)	Fermentas
BglII Fast Digest(20 U/μl)	Fermentas
HindIII Fast Digest(20 U/μl)	Fermentas
PstI Fast Digest(20 U/μl)	Fermentas
XmaI Fast Digest(20 U/μl)	Fermentas
KpnI Fast Digest(20 U/μl)	Fermentas
XbaI (20 U/μl)	NEB
NheI Fast Digest(20 U/μl)	Fermentas
NotI Fast Digest(20 U/μl)	Fermentas
DpnI (10 U/μl)	Stratagene
Pfu Turbo (2.5 U/μl)	Stratagene
Ampligase (20 U/μl)	Epicentre
T4 polynucleotide kinase	NEB
Vent DNA polymerase	NEB
Taq DNA polymerase	NEB
T4 ligase	Fermentas
DNAseI	Ambion
RNase Inhibitor	Roche
Superscript III Reverse Transcriptase	Invitrogen

Antibodies

Protein	Antibody	Produced in	Supplier
GFP	SP3005P anti GFP	rabbit	Acris
TPPII	anti TPP	rabbit	in house
20S	Tetra-His Antibody	mouse	Qiagen
Bs1 and Bs2	evoglow AB Bs	rabbit	Ecocatal
Pp1	evoglow AB Pp	rabbit	Evocatal

Kits

Protein Assay Kit	BioRad
QIAprep Spin Miniprep Kit	Qiagen
QIAprep Gel Extraction Kit	Qiagen
QIAprep RNA Purification Kit	Qiagen
QIAprep PCR Purification Kit	Qiagen
One Step Western	Genetech

3.2.5 Medium and Buffers

Medium

LB medium

10 g/l	NaCl
5 g/l	Tryptone
5 g/l	Yeast Extract

Autoclave at 121 °C for 20 min.

LB Agar

1 l	LB medium
15 g	Bacto Agar

Autoclave at 121 °C for 20 min.

Buffers

TAE buffer

40 mM	Tris-Acetat, pH 8.0
1 mM	EDTA

DNA sample buffer

0.2 %	bromphenol blue
30 %	glycerin

CCR buffer

200 mM	TrisHCl, pH 8.4
30 mM	$MgCl_2$
500 mM	KCl
5 mM	NAD

SDS sample buffer

50 mM	Tris, pH 8.5
5 % (w/v)	SDS
30% (v/v)	Glycerin
0.12%	Bromphenolblau
50 mM	DTT

SDS running buffer

100 mM	Tris
100 mM	Tricine
0.1% (w/v)	SDS

TbfI Solution

100 mM	RbCl
50 mM	$MnCl_2$
10 mM	$CaCl_2$
30 mM	KAc
15 % (w/v)	Glycerol pH adjusted to 5.8 with 0.1 M HAc.

TbfII Solution

10 mM	RbCl
75 mM	$CaCl_2$
10 mM	MOPS pH adjusted to 6.8 with 0.1 M KOH.

4x Laemmli deviding gel buffer

1.5 M	TrisHCl, pH 8.8
0.4 %	SDS

sterile filtered

4x Laemmli collecting gel buffer

0.5 M	TrisHCl, pH 6.8
0.4 %	SDS

sterile filtered

Antibiotics

Antibiotic	stock concentration	final concentration
Ampicillin	100 mg/ml	100μg/ml
Tetracyclin	2 mg/ml	2 - 8μg/ml
Gentamycin	100 mg/ml	100μg/ml

3.2.6 Cloning Techniques

Polymarease Chain Reaction (PCR)

Target DNA was amplifyed from chromosomal DNA or plasmid DNA with Polymerase Chain Reaction (PCR). Therefore primers flanking the gene of interest were chosen and the reaction mix was composed of

1 µl	template DNA
1 µl	forward primer
1 µl	reverse primer
1 µl	10 mM dNTPs
1 µl	Vent DNA polymerase
3 µl	ThermoPol DNA polymerase buffer
22 µl	H_2O
30 µl	total volume

The PCR was performed at

95 °C for 5 min
95 °C for 30 sec
55 °C for 30 sec
72 °C for 1 min
} x 35 cycles
72 °C for 3 min
4 °C for ∞

For amplifying TPPII the elongation step at 72 °C was carried out for 4 min, for the 20S proteasome the elongation step was carried out for 2 min.

Combined Polymerase Chain Reaction (CCR)

In this approach, the insertion of the mutation and the amplification of the mutated fragment occur in only one step. The CCR combines a PCR with a ligation reaction. Every cycle consists of four steps: denaturation of the plasmid DNA, annealing of the oligonucleotides, extension of the oligonucleotides and ligation of the 3'-OH-end of an outer oligonucleotide with the 5'-phosphate-end of the mutagenesis oligonucleotide. Hence, the ligation can only occur when the 5'-end of the mutagenesis oligonucleotide is phosphorylated. As the CCR runs at high temperatures, a thermostable ligase is needed.

For the synthesis the *Pfu*-polymerase was used.

Phosphorylation of the Mutagenesis Oligonucleotides

500 pM	mutagenesis oligonucleotide
10 mM	ATP
0.5 U	T4 Polynucleotide kinase
1 μl	10x T4 kinase buffer
10 μl	total volume

The phosphorylation mix was incubated at 37 °c for 30 min.

CCR Reaction

20 ng	phosphorylated mutagenesis oligonucleotide
20 ng	5'-oligonuclotide (forward primer)
20 ng	3'-oligonuclotide (reverse primer)
20 ng	plasmid DNA (template)
2 μl	10x CCR buffer
2,5 mM	dNTPs
2.5 U	*Pfu*-polymerase
3 U	Ampligase, thermostable
2 μl	10x BSA (4 mg/ml)

ad 20 μl H_2O

The reaction was performed at

95 °C for 5 min
95 °C for 30 sec
55 °C for 30 sec
56 - 67 °C for 1 min } x 35 cycles
72 °C for 3 min
4 °C for ∞

A gradient PCR was performed to determine the optimal annealing temperature for all three primers used in one reaction.

DNA Digest

Restriction digest reactions were carried out in 20 μl 1 x Fast Digest buffer (Fermentas) according to the manufacturer's advice. Resulting DNA fragments were separated by agarose gel electrophoresis.

Agarose Gelelectrophoresis

Samples containing DNA were mixed with 6x DNA sample buffer and loaded on 1% (w/v) agarose gels in 1x TAE buffer containing 1 μl ethidium bromide. A current of 80 - 100 V was applied to separate the DNA fragments. DNA bands were visualized on a UV-transilluminator.

Isolation of DNA from Agarose Gels

DNA fragments obtained by enzymatic digest or PCR reaction were isolated from the separating agarose gel by using the QIAquick Gel Extraction KIT (QIAGEN) according to the manufacturer's protocol. The DNA was eluted in 50 μl of buffer EB.

DNA Ligation

For the ligation of digested DNA fragments, the T4-Ligase of Epicentre was used.

1.5 μl	vector DNA
6.5 μl	insert DNA
1 μl	T4 buffer
1 μl	T4 ligase
10 μl total volume	

The reaction mix was prepared on ice an incubated at room temperature for 1 h.

DNA Transformation into *E. coli*

Competent cells were thawed on ice for 10 min. For ligation approaches 5 μl of DNA were added, for retransformation of complete vectors 0.5 μ l DNA were added and mixed carefully by tapping the tube. After another 20 min on ice, the cells were heat shocked at 42 °C for 45 sec using a waterbath (Haake B3) and subsequently cooled down on ice for two minutes. Then, 450 μl of liquid LB medium were added and the tubes were incubated at 37 °C shaking for one hour. The whole volume was then plated on LB plates containing 100 μg/ml Ampicillin and the plates were incubated over night at 37 °C.

Competent Cells

Competent DH5α cells were produced using the RbCl method modified after (Hanahan, 1983).
500 ml LB medium were inoculated with 10 ml of an overnight culture of *E. coli*DH5α and incubated at 37 °C until midlog-phase (OD_{600} $\tilde{0}$.6. The cells were then cooled down on ice for 15 min before harvesting them in a pre-cooled centrifuge at 1 000 g for 10 min at 4 °C. From this point on, all steps were carried out on ice. The supernating medium was disposed and remaining drops were removed carefully. The pellet was resuspended gently in 100 ml TbfI solution and incubated for 15 min. Cells were then spun down at 2 000 g for 5 min at 4 °C. After removing the supernatant, the cell were resusoended in 5 ml TbfII solution and incubated for further 45 min. Aliquots of 50 μl were shock frozen in liquid nitrogen and stored at -80 °C.

DNA Isolation from *E. coli* using MiniPrep

For the isolation of plasmid DNA a QIAprep Spin Miniprep Kit from QIAGEN was used. *E. coli* cultures containing the plasmid of choice were grown overnight at 37 °C. 4 ml culture were harvested by centrifugation at 20 000 g for 3 min, the supernatant was discarded. Cell lysis and plasmid purification were performed according to the manufacturer's instructions. The DNA was eluted with 50 μl of buffer EB.

3.3 Transgenic *Spiroplasma citri*

3.3.1 Strains

As *S. citri* strain, wild type cells GII-3 were used.

3.3.2 Medium and Buffers

Medium

SP4 medium

1 g	Mycoplasma Broth base
3 g	Bacto Tryptone
1.6 g	Bacto Peptone
225 ml	H_2O bidest

Autoclave at 121 °C for 20 min. After cooling down to 45 °C add

3 ml 50 % (w/v) Glucose
50 ml FKS Gold
25 ml 4 % (w/v) Yeastolate
15 ml 10x CMRL 66

Buffers

HS-buffer

20 mM HEPES
280 mM Sucrose

Autoclave at 121 °C for 20 min.

HSO-buffer

20 mM HEPES
280 mM Sorbitol

Autoclave at 121 °C for 20 min.

TG-buffer

25 mM Tris
190 mM Glycin

Autoclave at 121 °C for 20 min.

NaPi-buffer

0.5 M Na_2HPO_4
0.5 M NaH_2PO_4

mixed to a pH of 7.2
Autoclave at 121 °C for 20 min.

3.3.3 Transformation of DNA into *S. citri*

3 ml *S. citri* culture per transformation approach from an 18 h culture were harvested by centrifugation at 20 000 g for 20 min at 18 °C. The supernatant was discarded and the cell

pellet was resuspended in 1 ml HS buffer per transformation approach and resuspended carefully using a pasteur pipette. After a second centrifugation und the same conditions as described above, the pellet was resuspended in 0.4 ml HS buffer per transformation approach. Cell suspension was kept on ice until further use. In the meantime 1 μg DNA was diluted into a total volume of 20 μl using sterile water and brought into an electroporation cuvette with 4 mm distance (BioRad). The cuvettes holding the DNA were then incubated on ice for 5 min. 0.4 ml cell suspension were added to the cuvettes and incubated on ice for another 5 min. Transformation occurred using an electroporator (BioRad) with the following conditions: Pulsing two times at 1 000 Ohm, 10 μF and 2.5 kV. Time constants were measured for quality control of the transformation process. Directly after electroporation, 800 ml of SP4 medium was added and the whole volume was transferred to a new sterile tube. These tubes were then incubated at 32 °C for 3 h before 200 μl of transformation sample were applied to SP4 plates containing either 100 μg/ml Gentamycin or 2 μg/ml Tetracyclin. The plates were sealed with Parafilm and incubated at 32 °C for three weeks.

3.3.4 Control PCR for checking for the Presence of the Vector

To check if the transformation was successful and the colonies grown contain the vector of interest, a PCR was performed. Therefore primers were chosen that anneal to specific vector sequences that are not present in the chromosomal DNA. The PCR mix contained

1 μl	transformed *S. citri* culture
1 μl	forward primer
1 μl	reverse primer
1 μl	10 mM dNTPs
1 μl	Vent DNA polymerase
3 μl	ThermoPol DNA polymerase buffer
22 μl	H_2O
30 μl	total volume

The PCR was performed at

95 °C for 5 min
95 °C for 30 sec
55 °C for 30 sec
72 °C for 1 min
} x 35 cycles
72 °C for 3 min
4 °C for ∞

unless otherwise stated. 10 µl of the PCR mix were loaded to an agarose gel and examined.

3.3.5 RNA Isolation and Investigation

RNA Isolation

2 ml of a 48 h *S. citri* culture were harvested by centrifugation at 14 000 rpm for 5 min at 18 °C in an Eppendorff centrifuge. The supernatant was discarded and the pellet was resuspended in 600 µl RLT buffer (RNeasy Kit, Qiagen). One volume of Roti-Phenole (Roth) was added and the sample was vortexed (Vortexer) for one minute. After adding 300 µl glass beads (0.6 µ m diameter) the sample was vortexted three times for one minute, putting it on ice for one minute in between the vortexing steps. The sample was centrifuged at 14 000 rpm for 5 min and the supernatant was moved to a fresh tube and mixed with one volume chlorophorm by vortexing for one minute. After centrifugation at 14 000 rpm for another 5 min, the upper phase was separated and one volume 70 % Ethanol was added. This mix was then transferred to an RNeasy column (Qiagen) and the washing and recovering from the column was performed according to manufacurers protocol. This yielded 40 µl RNA in sterile, RNase-free water.

RT-PCR

First, the success of RNA isolation was checked by performing an agagose gelelectrophoresis on a 1.2 % TBE gel containing 1 % GITC. 5 µl RNA were mixed with 1 µl DNA sample buffer and loaded onto the gel. Applying 80 V current, the running time was about 45 min. After that, DNase was added to the RNA using the following scheme:

25 µl	RNA
3 µl	DNase buffer
1 µl	DNaseI (Ambion)
30 µl	total volume

The reaction mix was incubated at 37 °C for 1 h.
The digest was stopped by adding 5 µl inactivation reagent and vortexing thorrowly, before centrifuging 10 000 rpm for 5 min at 4 °C. The supernatant was moved to a fresh tube.
To make sure that no DNA was left in the RNA sample, a PCR was performed using primers annealing to the gene of interest. The result was checked by performing an agarose gelelectrophoresis. If no bands were visible, cDNA synthesis was performed, otherwise the DNase digest was repeated.
For the cDNA synthesis 10 µl RNA (5 ng) were mixed with 1 µl random hexamer solution (Fermentas) and incubated at 70 °C for 5 min. Then, the following chemicals were added:

0.5 µl	RNase inhibitor
4 µl	First Strand Buffer
1 µl	0.1 M DTT
1 µl	dNTPs
1 µl	Superscript III Reverse Transcriptase
1.5 µl	H_2O
20 µl	total volume

The reaction mix was incubated at 42 °C for 1 min. Then the reverse transcriptase was inactivated at 65 °C for 15 min.

PCR with cDNA

The PCR with cDNA was performed with

0.5 µl	primer forward
0.5 µl	primer reverse
0.5 µl	cDNA
0.5 µl	dNTPs
1 µl	Vent DNA polymerase
2 µl	ThermoPol DNA polymerase buffer
15 µl	H_2O
20 µl	total volume

cycling at

95 °C for 3 min
95 °C for 30 sec
55 °C for 30 sec
72 °C for 1 min
} x 35 cycles
72 °C for 3 min
4 °C for ∞

10 µl of the PCR mix were loaded onto a TAE agarose gel and investigated.

3.3.6 Protein Isolation and Characterization

Lysing *S.citri*

S. citri cells were lysed by mechanical forces. The cells were harvested by centrifugation at 20 000 g for 15 min at 18 °C. After removing the supernatant the pellet was resuspendet carefully in 200 µl buffer for washing. After a second centrifugation step the cell pellet was resuspended in 50 - 100 µl of NaPi buffer. Glass beads with a diameter of 0.6 mm were added to the cell suspension and the sample was vortexted virorously for 1 min and put on ice for 1 min immediately. The vortexing step was repeated three times with incubation on ice as last step. Then the sample was centrifuged at 20 000 g for 10 min at 4 °C and the supernatant was moved to a fresh tube.

SDS-PAGE

10 µl of the sample were mixed with 10 µl of SDS sample buffer and incubated at 95 °C for 5 min for denaturation. Subsequently the sample was loaded on a 12 - 15 % SDS gel and run, together with a protein standard ladder, at 25 mA for 1.5 h.
The gel was then removed from the chamber and washed with MilliQ three times for 10 min. Staining was performed with Coomassie Hot Stain solution or with PageBlue solution (Fermentas). Destaining was done overnight in MilliQ.

Western Blot Analysis

For Western Blot Analysis, the unstained SDS gels were blotted to a nylon membrane using a wet chamber. Therefore the gel and four Whatman papers of the same size were incubated for 5 min in TB buffer. The gel was then placed on the nylon membrane and any air in between was removed. With two Whatmanpapers flanking on each side, the gel and the membrane were placed into the blotting apperature (BioRad) according

to the manufactureres instructions. The blotting was then performed with 100 V and 400 mA for 1 h.
Detection of the protein of interest was done using the One-Step Western Kit (Genetech) according to the manufacturers protocol. The blot was developed by applying 10 ml of chemoluminescent substrate (Chromosensor) for 10 min. The developed blot was scanned immediately.

4 Distribution of Macromolecules

4.1 Growth States of *S. citri*

4.1.1 Monitoring the Growth of *S. citri*

In this work, we were interested in the distribution of macromolecules in different growth states of *S. citri*. To determine the doubling rate and the distinct growth states of the cells, growth curves were recorded. *S. citri* is so small that the light absorption of the culture does not change significantly over time. Thus, measuring the optical density is not suited for monitoring the growth of these cells. Therefore, the method most commonly used for this is plating appropriate dilution series and subsequent counting for colony forming units.

For rough estimation of the culture growth the SP4 medium contains Phenol Red. As the cells produce lactate during metabolism, the medium gets more acid over time and the color changes from red over orange to yellow.

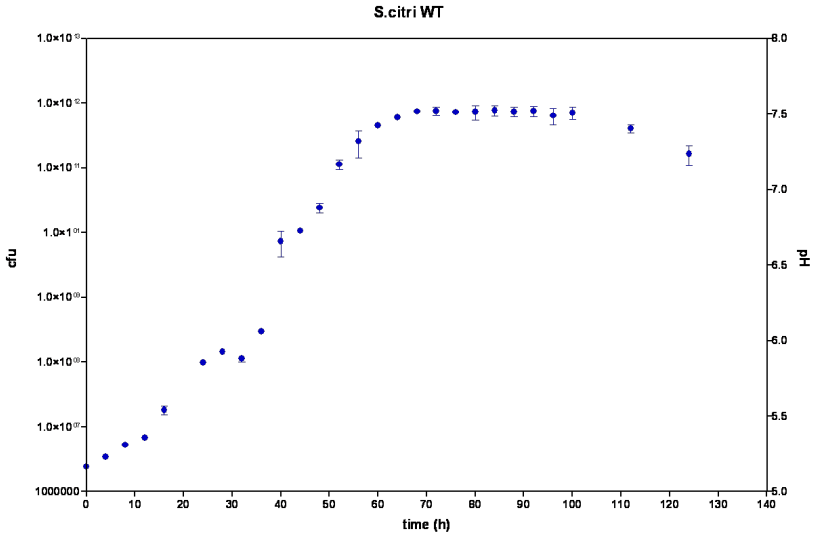

Figure 4.1.1: Growth curve of *S. citri*. Every four hours, 100 μl of the culture were diluted and plated on SP4 plates. 10 days later the colonies were counted and the colony forming units (cfu) per μl were calculated.

4.1.2 Division Rate and Generation Time

As seen in figure 4.1.1, *S. citri* starts with a short linear lag-phase during the first hours of growth before entering the exponential growth phase, the so-called log-phase. After 56 h the cell growth slows down and passes into the stationary phase where cell division and cell death are in equilibrium. After 120 h the culture enters the starvation phase.

The division rate is defined as

$$\nu = \frac{\lg N_{t2} - \lg N_{t1}}{\lg 2(t_2 - t_1)} \tag{4.1.1}$$

with N being the number of colony forming units at time point t_i.

With a colony number of $2*10^{11}$ at 54 h and $3.5*10^7$ at 16 h, the division rate calculated from this growth curve is $\mathbf{0.33\,h^{-1}}$.

The generation time is calculated by $g = \frac{1}{\nu}$: **3 h**.

4.1.3 Alternative Methods for Monitoring *S. citri* Growth

Monitoring the growth of *S. citri* by counting the colony-forming units bears some disadvantages: First, it is extremely media-consuming, owing to the fact that in late logarithmic and in stationary phase the dilution factor for an appropriate number of colonies is 10^{12}. Also the amount of medium that is needed for the plates is not to be underestimated.
Finally, this is a very time-consuming method. As *S. citri* is very small and grows slowly, it takes about 10 days for the colonies to become visible on the plates. A slight deviation of dilution can cause very dense plates which makes counting difficult.

For these reasons, alternative methods for monitoring cell growth were tested on their suitability for *S. citri*. As mentioned above, *Spiroplasma* produces lactate during growth. The drop in pH of the medium could be used for monitoring the growth of the cells by measuring the pH. Another possibility is to measure the amount of total protein in a defined volume of the culture.

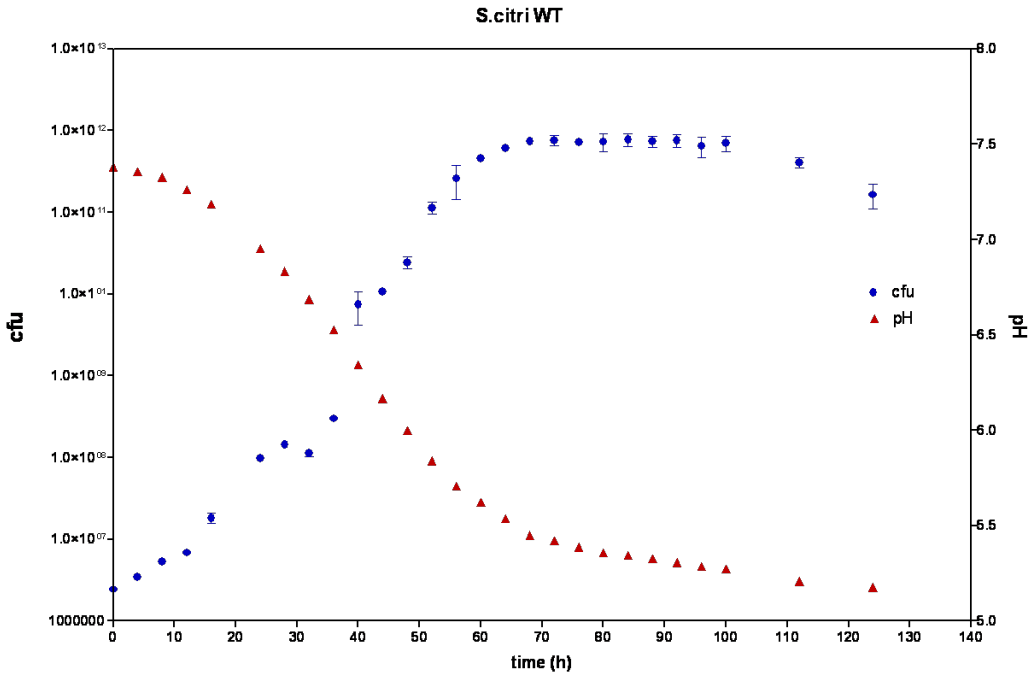

Figure 4.1.2: Growth curve of *S. citri*. Blue: Colony forming units. Red: pH.

As depicted in figure 4.1.2, the pH correlates to the colony-forming units obtained by plating. Measuring the protein concentration turned out to be error-prone, the variance of the values was very high. This is due to two main reasons: First, it is complex to lyse the cells and then it is error-susceptible due to the small volumes and the difficulties to remove the whole supernatant before resuspending the cells in a defined volume of buffer.
On the contrary, measuring the pH turned out to be very easy, quick and precise and was hence used for all further growth measurements.

4.2 Cell Morphology related to Growth Phase

In this study, we wanted to examine the distribution and topology of ribosomes in different growth states of *S. citri*. According to the growth curve shown in 4.1.1 the stages for logarithmic, stationary and starvation phase were specified:
Samples were taken after 4 h, 72 h and 120 h corresponding to logarithmic phase, stationary phase and starvation phase, respectively.

4.2.1 Light Microscopy of *S. citri* during different Growth States

S. citri is a motile, helical, wall-free organism that replicates by elongation and subsequent restriction [29].
The cell morphology of living *S. citri* cells in the logarithmic and in the stationary phase was monitored by phase-contrast light microscopy.

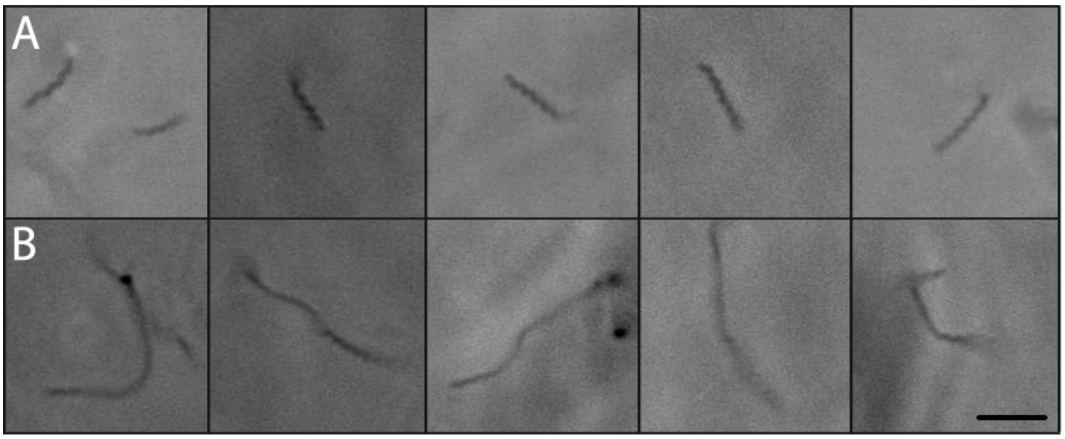

Figure 4.2.1: Light microscopy of *S. citri* in logarithmic and sationary growth phase. A) Logarithmic phase (4 h), B) stationary phase (72 h). Magnification: 1000 x, Scalebar corresponds to 5 μm.

In logarithmic phase, the cells show distinctive helical form with an average length of five turns. One turn is equivalent to 1 μm. In the stationary phase the cells elongate up to a length of 14 turns and show progressive loss of helicity.

4.2.2 Cryo-electron Tomography of *S. citri* during different Growth States

The Logarithmic Growth State

As *Spiroplasma* lacks a cell wall, the organism is very fragile and tends to rupture by the influence of mechanical forces, osmolarity or pH. Therefore a method for sample preparation had to be established that preserves the physiological shape of the cells.
Prior to plunge-freezing, the cells were washed and resuspended in a high-osmolar buffer containing sorbitol, a sugar that can not be catabolized by *S. citri*. In combination with a very slow-soaking filter paper the amount of cells on the grid that were visibly intact increased enormously compared to cells that were blotted directly from the medium.

The morphology of the *S. citri* cells observed by light microscopy was preserved during

the treatment and plunging procedure, judging the appearence of the cells in the electron tomograms (figure 4.2.2, 4.2.3 and 4.2.4).

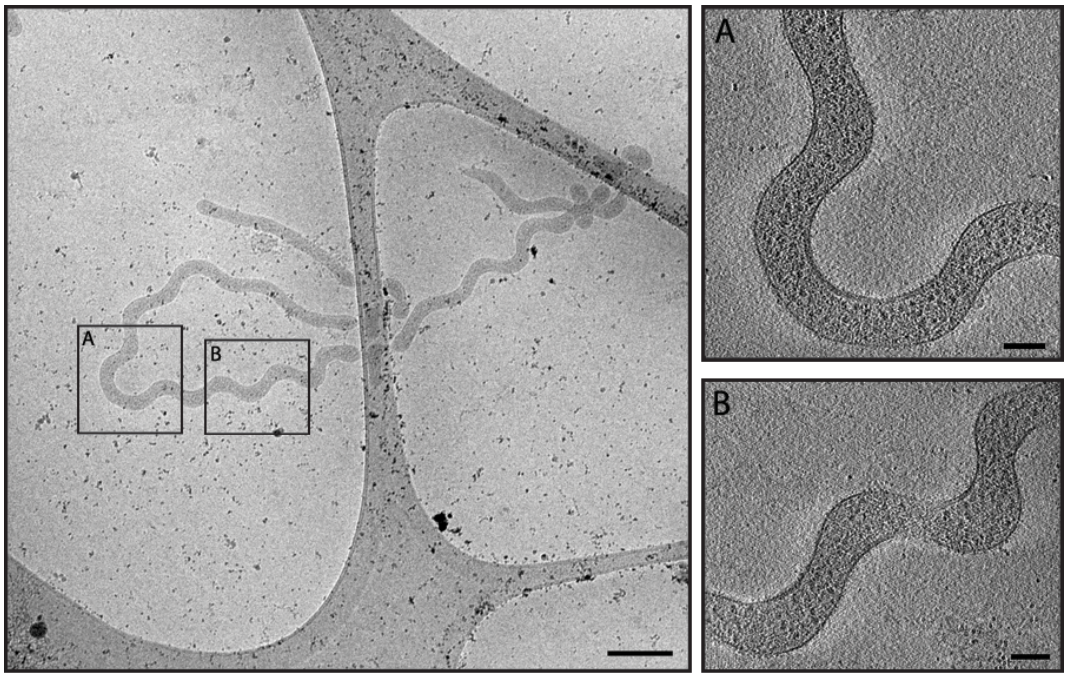

Figure 4.2.2: Electron tomography of *S. citri* in logarithmic growth phase (4 h). Left: Overview micrograph with a nominal magnification of 9 300 x (screen up); Scalebar corresponds to 400 nm. A) and B) Orthoslices of detail tomograms; Scalebar corresponds to 100 nm.

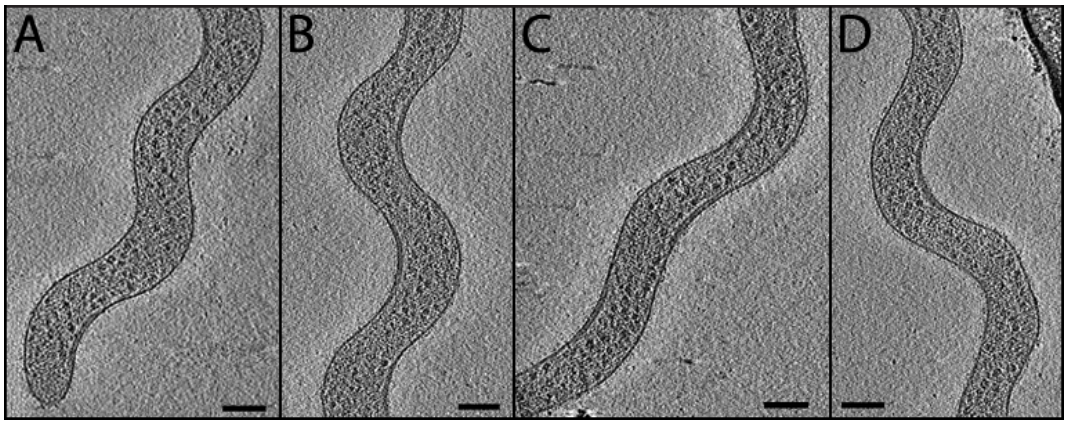

Figure 4.2.3: Electron tomography of *S. citri* in logarithmic growth phase (4 h) II. A) to D) Orthoslices of detail tomograms of several *S. citri*; Scalebar corresponds to 100 nm.

The morphology of the cells drawn from the tomograms is very uniform. The cells in

exponential growth phase all show a clearly defined helical shape and have an average diameter of 120 nm.
From the 13 tomograms taken after 4 h, four showed the end/ head of the cell, like seen in figure 4.2.3A. Three of these ends had a blunt but strait shape, while one cell showed a tapering end which indicates that the cell had divided recently (see figure 4.2.4).

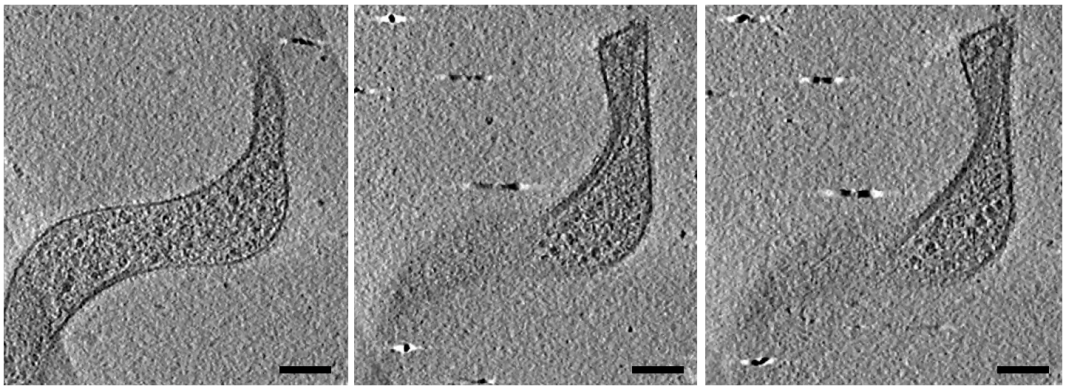

Figure 4.2.4: Orthoslices of a *S. citri* cell with tapered ends. From left to right: orthoslices separated by 21.6 nm and 28.8 nm from an original reconstruction of 120 slices. Scalebar corresponds to 100 nm.

The orthoslices already reveal the presence of macromolecular complexes. The cytoplasm is well-filled with particles that appear as contrasted motives.
Another feature that is visible in the orthoslices is a part of the bacterial cytoskeleton. The filaments that form the turn by spanning the cell are clearly evident, especially in figure 4.2.4.

The Stationary Growth Phase

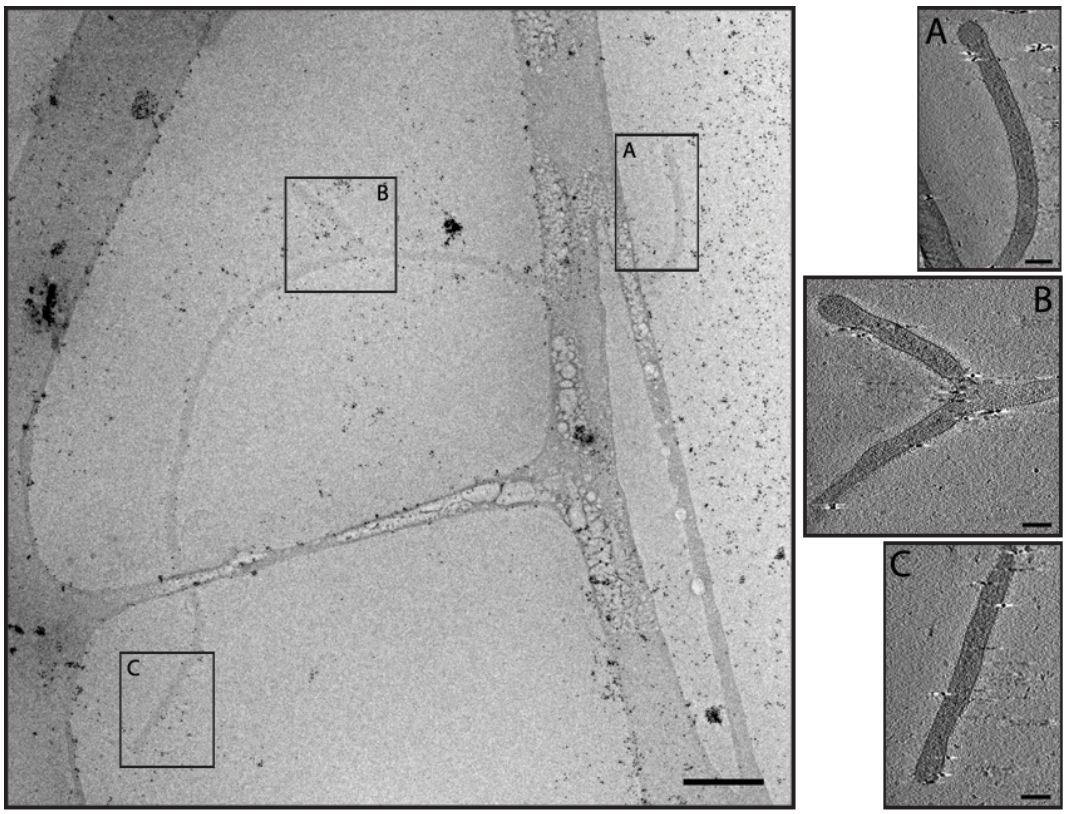

Figure 4.2.5: Electron tomography of *S. citri* in stationary growth phase (72 h). Left: Overview micrograph with a nominal magnification of 9 300 x (screen up); Scalebar correspondes to 400 nm. A) to C) Orthoslices of detail tomograms; Scalebar corresponds to 100 nm.

The tomograms taken after 72 h reveal the changing morphology of *S. citri* when entering the stationary phase. The cells lost their helicity and are significantly thinner with an average diameter of 90 nm and the ends/ heads of the cells are exclusively blunt with a rounded form.

The contrast of the tomograms is generally lower than the contrast of the tomograms taken in logarithmic phase. Nevertheless, contrasting particles can also be seen in orthoslices from stationary phase tomograms. But no cytoskeletal filaments could be detected in these cells.

A morphological feature that was only observed in older cells (stationary and starvation phase) is depicted in the overview picture of figure 4.2.5 and the corresponding detail in figure 4.2.5**B**): A second cell branches from the main body.

The overview micrograph was acquired after tomogram acquisition. The beam damage caused by extensive electron exposure during tracking and focusing is visible on the carbon film.

The Starvation Phase

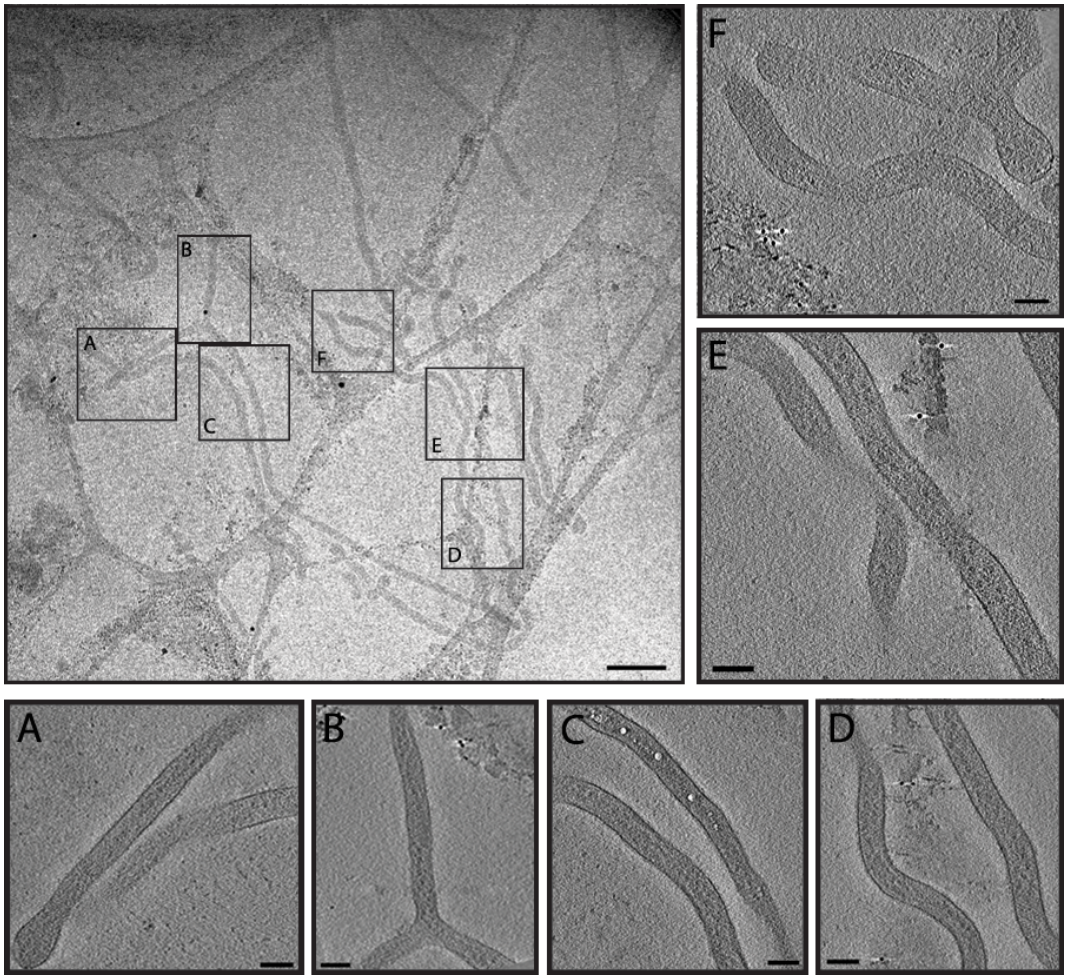

Figure 4.2.6: Electron tomography of S. citri in starvation phase (120 h). Upper left: Overview micrograph with a nominal magnification of 9 300 x (sceen up); Scalebar correspondes to 400 nm. A) to F) Orthoslices of detail tomograms; Scalebar corresponds to 100 nm.

The cell length still increases from stationary to starvation phase. Despite the enormous length of about 9 μm, the cell morphology in general is quite similar to the 72 h cells: There is no regular helicity and the cells show rounded ends/ heads. The average diameter of the cells is about 85 nm and therefore only slightly thinner than in stationary

phase.
Again, a branching event was observed (figure 4.2.6**B**). All tomograms shown were taken from different parts of the same cell. Owing to overlapping exposure sites the tomogram depicted in 4.2.6**C** shows some beam damage.

4.3 Ribosome Distribution

4.3.1 Template Matching

Template matching was performed with Molmatch. To calculate the *local correlation function (LCF)* the structure of the 70S ribosome from *E. coli* filtered to a resolution of 5 nm was used.

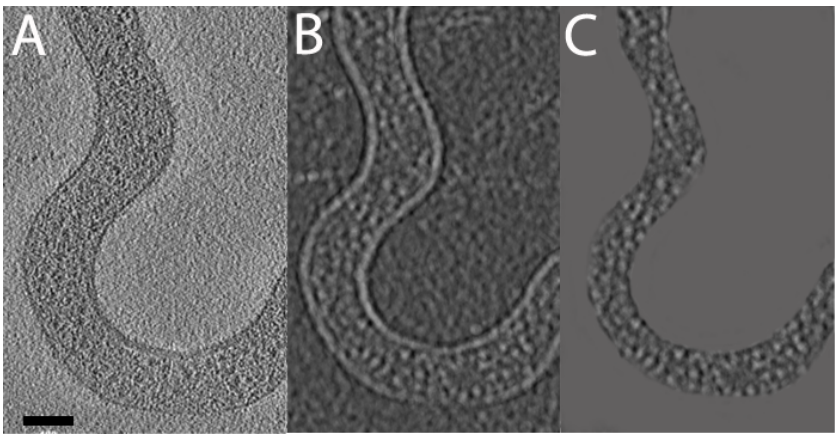

Figure 4.3.1: Matching the 70S ribosome in *S. citri* with molmatch. A) Orthoslice (1.9 nm) from the processed tomogram; Scalebar corresponds to 100 nm. B) Orthoslice of the *LCF* volume (molmatch output). C) Orthoslice of masked volume with excluded membranes

The intensity of the peaks in the *LCF* volume correlates to the value of the cross-correlation coefficient (figure 4.3.1). Goldmarkers present in the tomogram used for fiducial alignment of projections and the membrane tend to show cross-correlation with the template, which is due to their high contrast. Therefore, the membrane and the goldmarkers have to be masked prior to selection of peaks, to prevent false positives.
From this limited volume the 300 highest values of the *LCF* were extracted. The particles corresponding to the peaks were subsequently inspected visually to discard other conspicuous false positive detection.

The template matching algorithm was run twice: Once with the correct template hand-

edness and once with a mirrored version of the template. The corresponding cross-correlation coefficients were plotted and compared (figure 4.3.2).

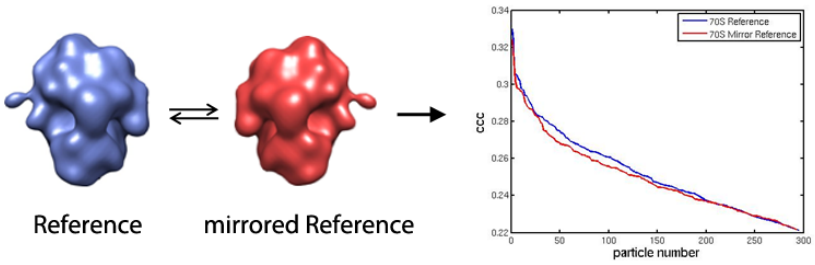

Figure 4.3.2: Comparison of the cross-correlation coefficients of the correct template and a mirrored version of the template.

The values corresponding to the correct template are slightly higher than the values corresponding to the mirrored version, but this difference is important evidence of ribosome-recognition fidelity. This validates a reliable detection of correct orientations of ribosomes in the tomograms.
The selected particles were reconstructed as subtomograms in full resolution. Classification based on constraint-correlation and principal component analysis (PCA) clustering was performed. Particles were grouped into seven classes for each growth state depending on their similarity (figure 4.3.3). The number of classes was chosen arbitrarily with the purpose to include 200 - 300 particles in each class. The particles that contribute best to the 3D reconstruction were selected. Thus, the initial subset of particles was further adjusted by excluding false positives.

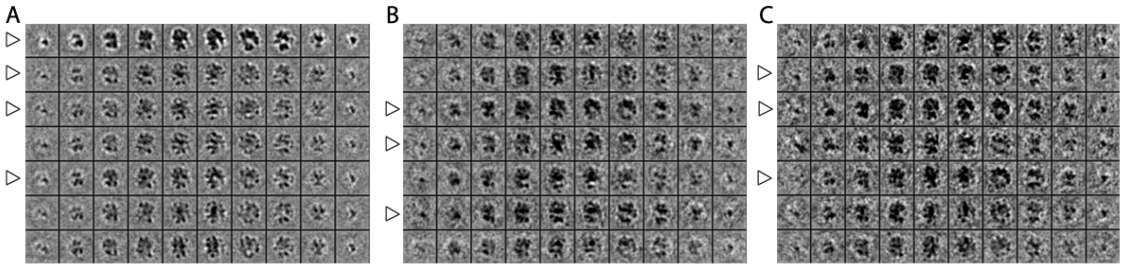

Figure 4.3.3: Classification of particles: 10 slices from the 3D averages from the seven classes. The particles obtained by the tomograms of the different growth states were grouped into seven classes (top to bottom) each. A) Particle classes 1-7 (top to bottom) from the 4 h tomograms. B) Particle classes 1-7 (top to bottom) from the 72 h tomograms. C) Particle classes 1-7 (top to bottom) from the 120 h tomograms.

The quality of the classes and therefore the contribution of the contained particles to

the 3D average, were judged based on the appearance and the ccc value. For the 4 h particles, class 1, 2, 3 and 5 were chosen, for the 72 h particles class 3, 4 and 6 and for the 120 h particles class 2, 3 and 4. Those particles are considered to be correctly identified ribosomes. The particles contained in the other classes were discarded.

4.3.2 Distribution and Orientation of Ribosomes

The particles identified as ribosomes were visualized inside the cell to get an overview of the cellular distribution. The coordinates for the location and orientation of the ribosomes were extracted from the Molmatch file. The cell membrane was segmented manually with Amira.

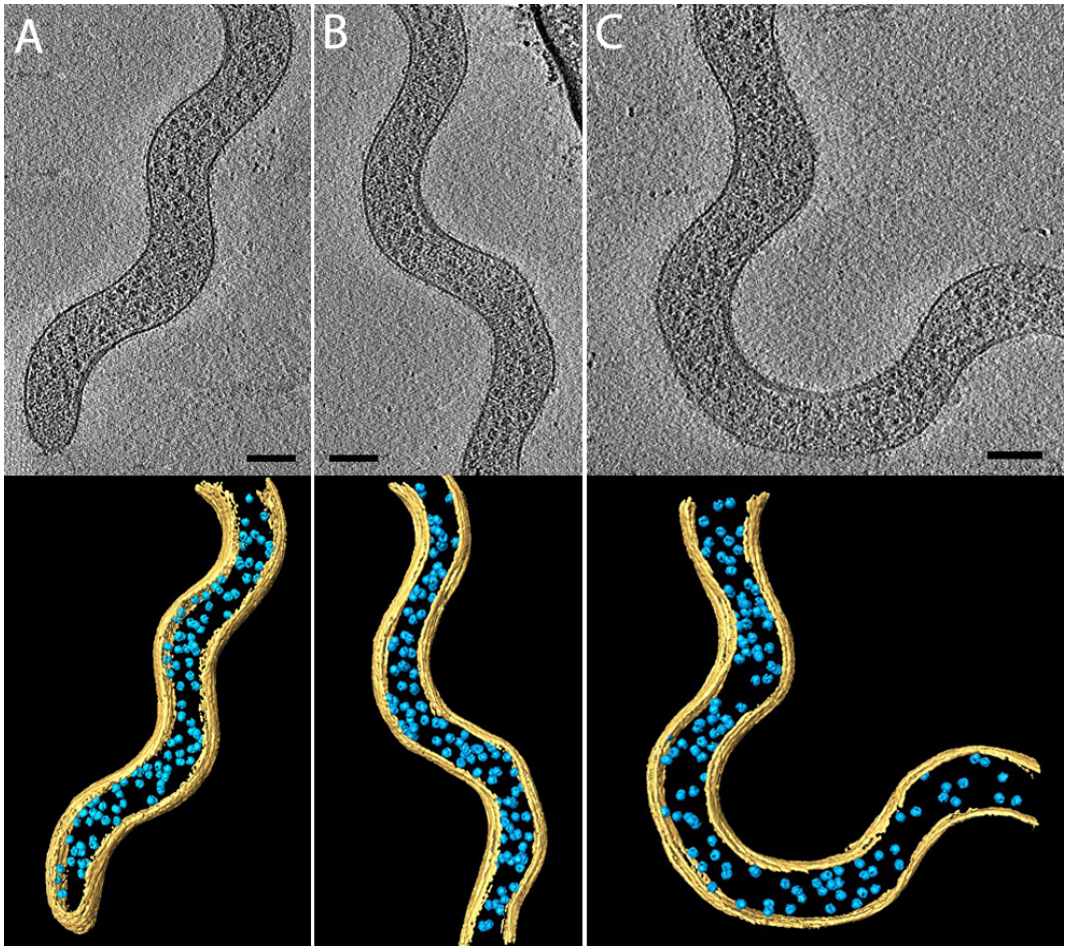

Figure 4.3.4: Distribution of ribosomes inside the cell at 4 h. A) to C) Three orthoslices from tomograms are shown with the corresponding segmentation. Top: Orthoslices of 4 h tomograms. Bottom: Corresponding segmented membranes with ribosomes.

The ribosomes appear to be distributed all over the cells. But it is hardly possible to decide by eye whether they form local clusters or are excluded from certain cell regions to an extend that deviates from statistical fluctuations. To evaluate possible deviations from a hypothetical equal distribution, the positions of ribosomes were analyzed. Each cell was devided into N slices of constant volume along the longitudinal axis, N beeing the number of ribosomes in the respective cell, such that one particle per subvolume can be expected on average. By this way, the helical or curved cells were virtually straightened to cylindric volumes and were made comparable to each other. The actual number of ribosomes per slice was determined and the frequencies compiled in a histogram (figure 4.3.6, 4.3.9 and 4.3.12). The data follows a Poisson distribution if the particles were randomly distributed in the cell. The model was varified with simulated data (figure 4.3.5**B**).

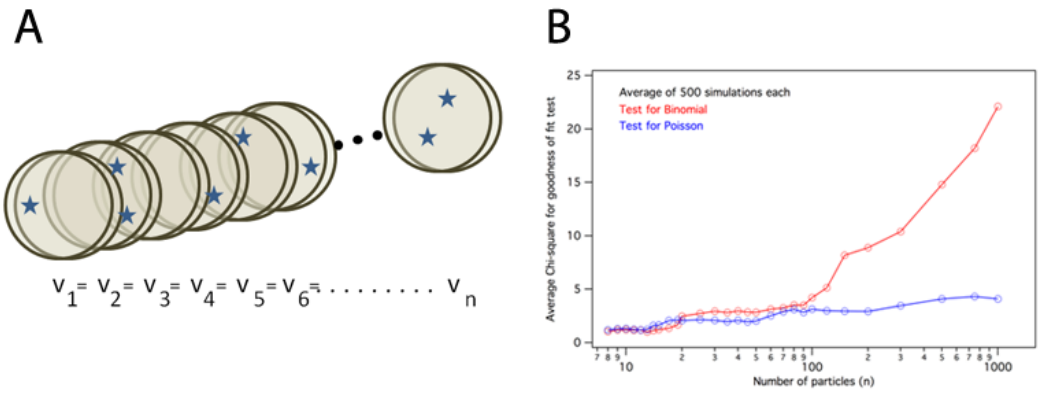

Figure 4.3.5: Distribution analysis of ribosomes along the cell. A) The cells were devided into slices with a volume of the occupancy for one ribosome. All slices have the same volume. B) Model of a statistical uniform distribution depending on the number of particles used for the simulation. For both models, Binomial and Poisson, 500 independent calulations were done and the Chi^2 values were plotted.

The Poisson distribution is particularly affected if particles are systematically clustered, but is 'blind' with respect to the positions of occupied and empty segments. Therefore, this analysis was combined with a subsequent distance analysis between particles. For the sake of simplicity, the relative positions of occupied segments were taken for calculating all distances and these were compiled in a histogram (figure 4.3.7, 4.3.10 and 4.3.13). The expected distribution is a linear function of the distance with (N-1) shortest distances between neighboring particles [segments] down to 1 largest distance between the particles [segments] located at the very ends of the cell 'tube'. The model is depicted as red line.

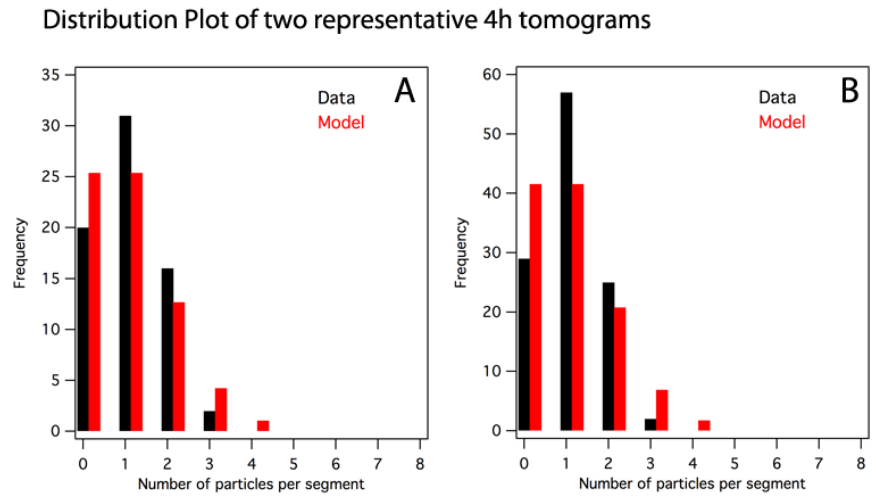

Figure 4.3.6: Distribution of ribosomes along the cell for two representative 4 h tomograms. A) Distribution of tomogram t4; B) Distribution of tomogram t3.

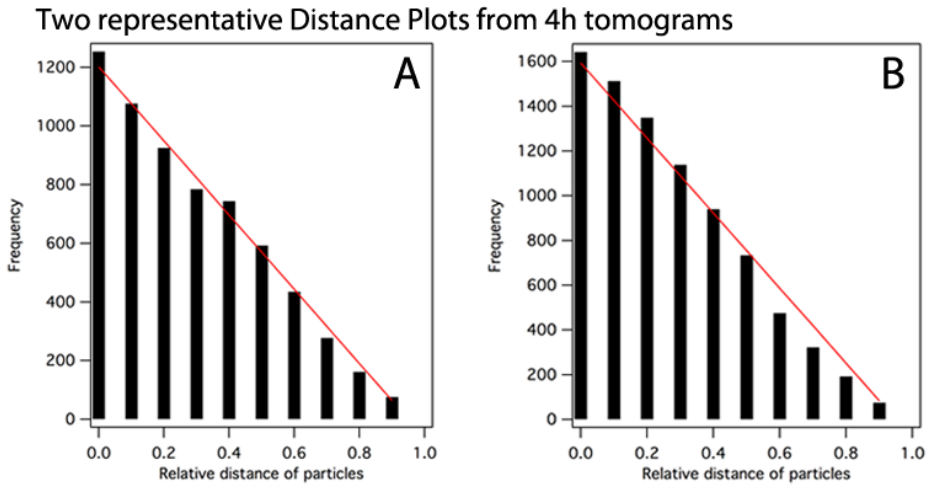

Figure 4.3.7: Distance analysis of ribosomes along the cell for two representative 4 h tomograms. A) Distribution of tomogram t3; B) Distribution of tomogram t4.

According to the analysis, there is no specific clustering in the 4 h cells. The particles are distributed evenly along the cell axis and no particular pattern is discernible. The distribution plot (figure 4.3.6) shows a frequency of slices containing one ribosome that is higher at the expense of empty slices compared to frequencies expected. The distance plot (figure 4.3.7) of the two representative 4 h tomograms shows a nearly perfect statistical uniform distribution that fits to the predicted model (red line). The very slight

over-representation of short distances (figure 4.3.7**B**) correlates to the high frequency of one particle per segment (figure 4.3.6). The analysis indicates that there is a kind of systematic distribution of particles along the cell but no clustering.

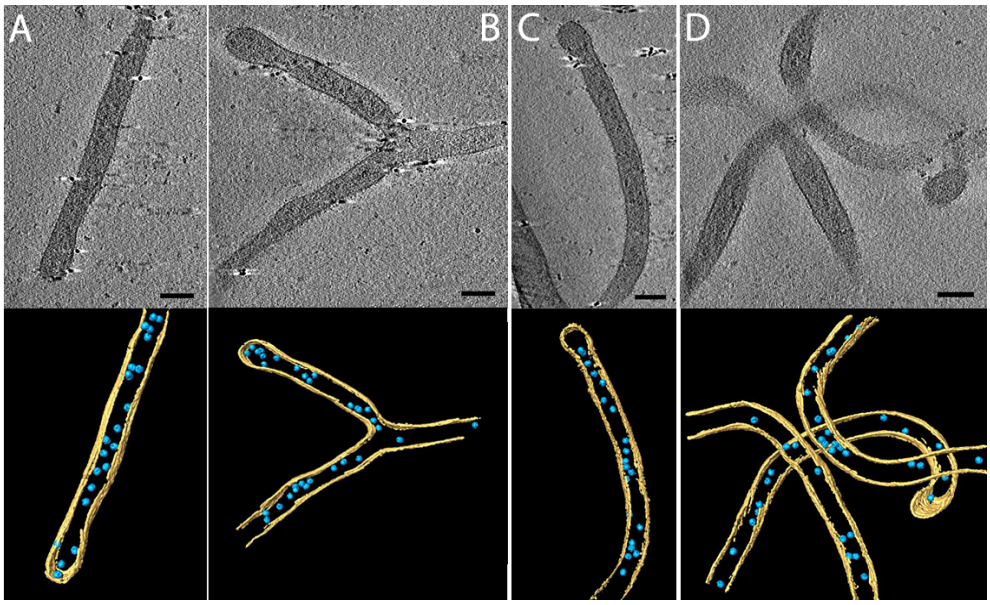

Figure 4.3.8: Distribution of ribosomes inside the cell at 72 h. A) to D) Four orthoslices from tomograms are shown with the corresponding segmentation. Top: Orthoslices of 72 h tomograms. Bottom: Corresponding segmented membranes with ribosomes.

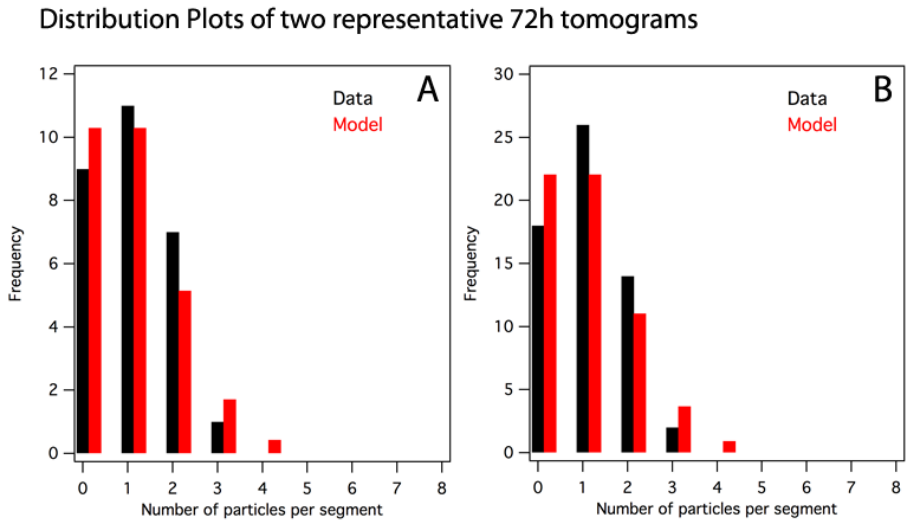

Figure 4.3.9: Distribution of ribosomes along the cell for two representative 72 h tomograms. A) Distribution of tomogram t9; B) Distribution of tomogram t11.

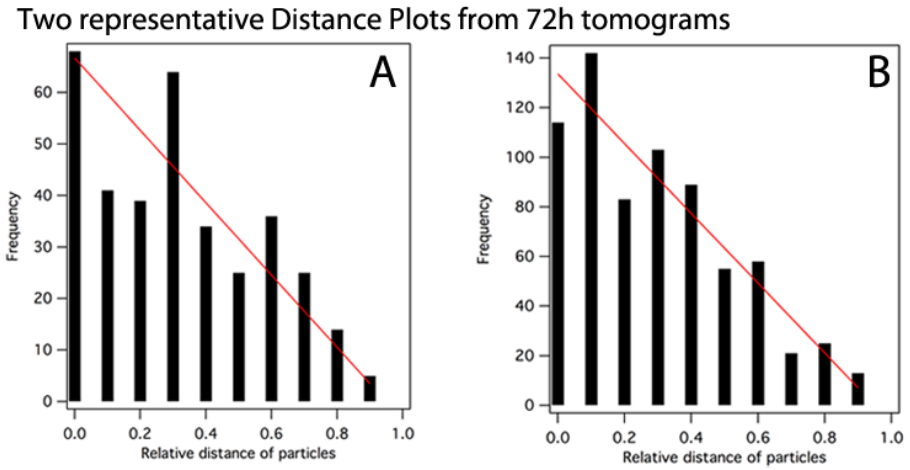

Figure 4.3.10: Distance analysis of ribosomes along the cell for two representative 72 h tomograms. A) Distribution of tomogram t11; B) Distribution of tomogram t12.

There are less ribosomes in the stationary phase cells (72 h) than in the logarithmic phase cells shown before (figure 4.3.8). The distribution plot shows a statistical uniform distribution of the ribosomes over the length of the cells that does not differ significantly from the Poisson model (figure 4.3.9). But the Poisson model does not take into account the local distribution of occupied and empty segments. The distance analysis shows that there are considerable abberations from the expectation that are in agreement with the optical impression: There are gaps that cause a passive formation of groups. Accordingly, medium and higher distances are over-represented. There are two scenarios: Some of the tomograms show a decrease in short distances with a related increase of medium distances (figure 4.3.10**A**), whereas some tomograms show a uniform distribution, that is, still, not as accurate as for the 4 h tomograms (figure 4.3.10**B**). This indicates, that during stationary phase there is a uniform distribution of ribosomes along the cell with some clustering events.

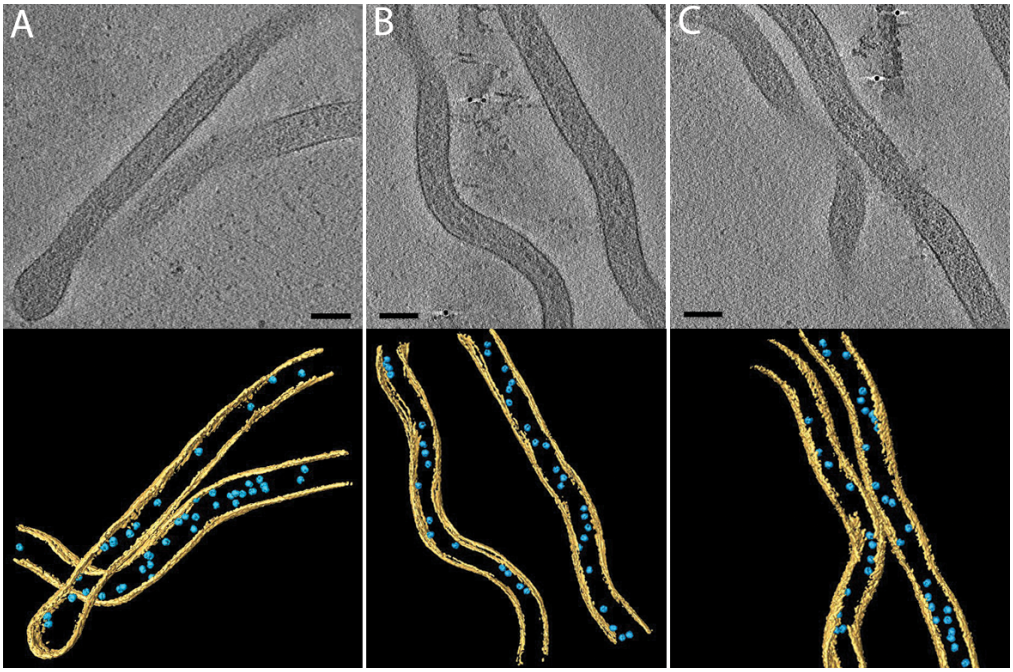

Figure 4.3.11: Distribution of ribosomes inside the cell at 120 h. A) to C) Three orthoslices from tomograms are shown with the corresponding segmentation. Top: Orthoslices of 120 h tomograms. Bottom: Corresponding segmented membranes with ribosomes.

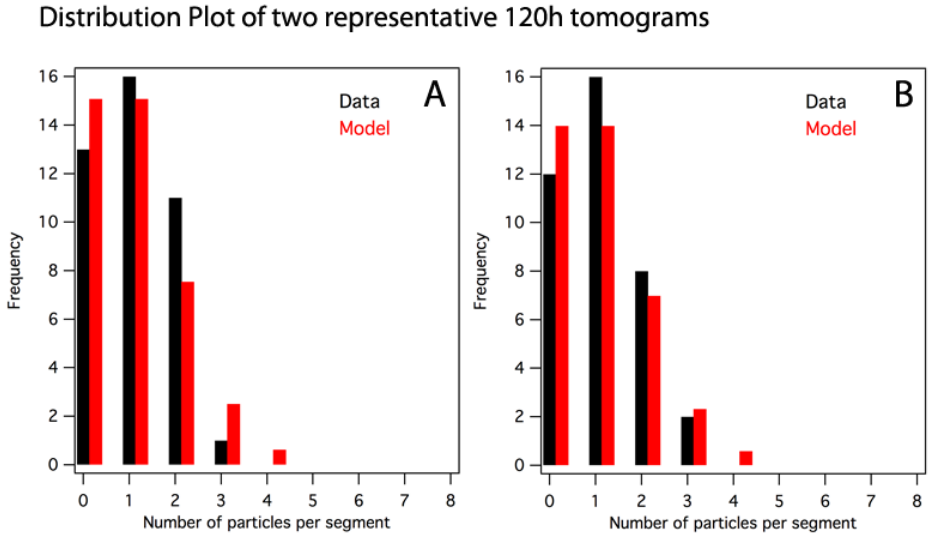

Figure 4.3.12: Distribution of ribosomes along the cell for two representative 120 h tomograms. A) Distribution of tomogram t11; B) Distribution of tomogram t9.

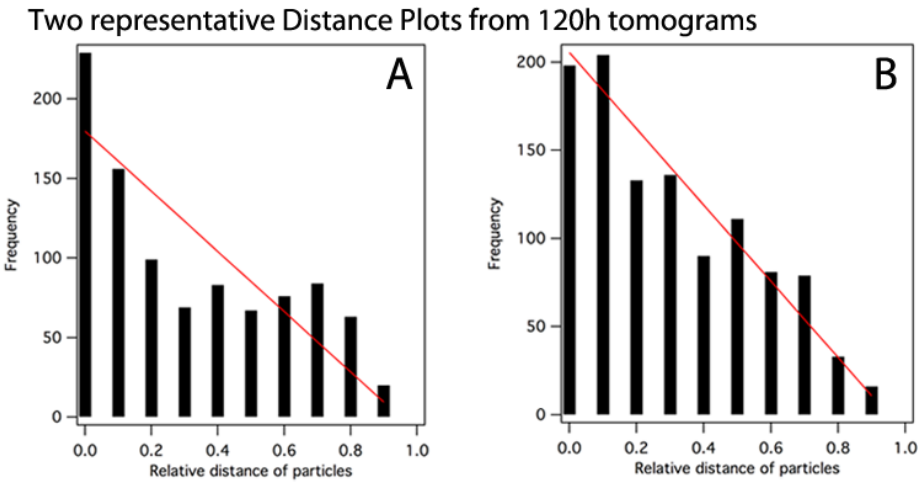

Figure 4.3.13: Distance analysis of ribosomes along the cell for two representative 120 h tomograms. A) Distribution of tomogram t9; B) Distribution of tomogram t13.

The 120 h cells also show no visible pattern of ribosomes (figure 4.3.11). The number of ribosomes is comparable to the number of ribosomes in the stationary phase. The distribution plots are similar to the distribution plots of the 72 h cells: the distribution pattern of the ribosomes along the cell does not differ significantly from the Poisson model, but the distance plots for the 120 h tomograms show a passive formation of groups caused by a number of connected, empty segments. One part of the tomograms show some distinct clustering with decreased frequencies for short and medium distances and increased frequencies for long distances (figure 4.3.13**A**). The other part shows a more uniform distribution but also with some medium and long distances that are more frequent than expected by the model (figure 4.3.13**B**). The amount of connected unoccupied slices in 120 h cells is still higher than in the 72 h cells. The analysis indicates a statistical uniform distribution along the cell with partially considerable clustering events.

4.3.3 Distance of Ribosomes to the Membrane

Another point of interest is the distribution of the ribosomes in relation to the cell membrane. Therefore, the distance from the center of mass of the ribosomes to the membrane was calculated for four tomograms from stationary phase and for five tomograms from logarithmic and starvation phase. Only tomograms with the same cell diameter within the growth state were used for this analysis. The distances were calculated and plotted in a histogram. A statistical uniform distribution of the distances would result in a histogram like shown in figure 4.3.14**B**: The decay at the very short distances is due to the center of mass beeing the reference point. The ribosomes can not be closer to the

membrane then the size of their radius. Thus, an area close to the membrane can not be occupied by ribosomes. Moreover, due to the missing wedge, ribosomes with a very short distance to the membrane can not be visualized and are therefore missing for the analysis (figure 4.3.14**A**).

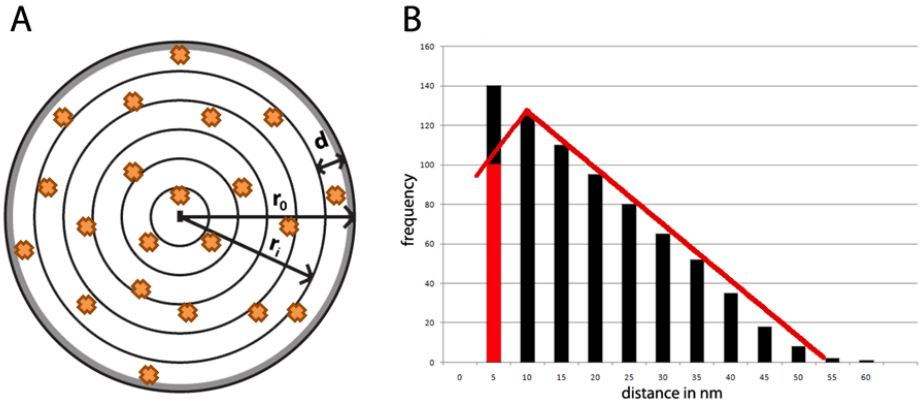

Figure 4.3.14: Distance of ribosomes to the membrane. A) Schematic drawing of a cross-section through the cell. There is an area in the outer most ring where no ribosomes can be located (grey). B) Model for a statistical uniform distribution of the distances of the ribosomes to the membrane. Red: Model taking into account the excluded volume and the missing wedge. Black: Model without the technique-dependent influences.

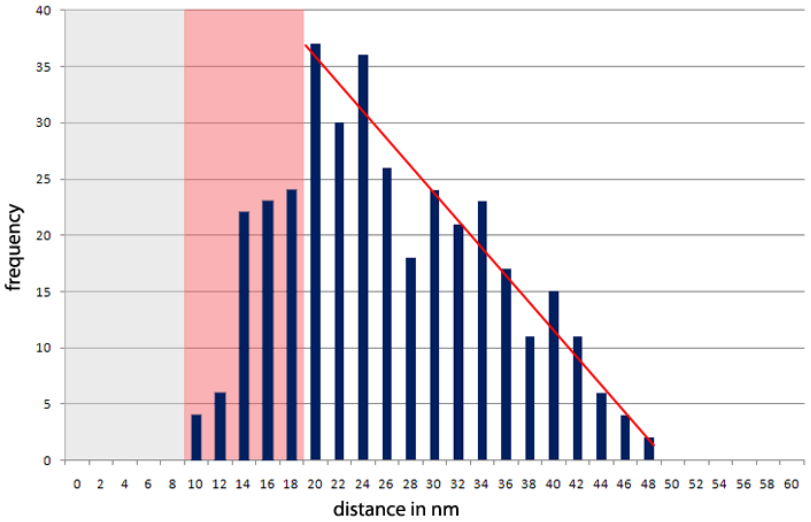

Figure 4.3.15: Distance of ribosomes to the membrane for five 4 h tomograms with equal cell diameter. Grey: Area where no ribosomes can be located by their center of mass. Red: Predicted decay due to the masking during the template matching process and the missing wedge effect. The predicted model is shown as a red line.

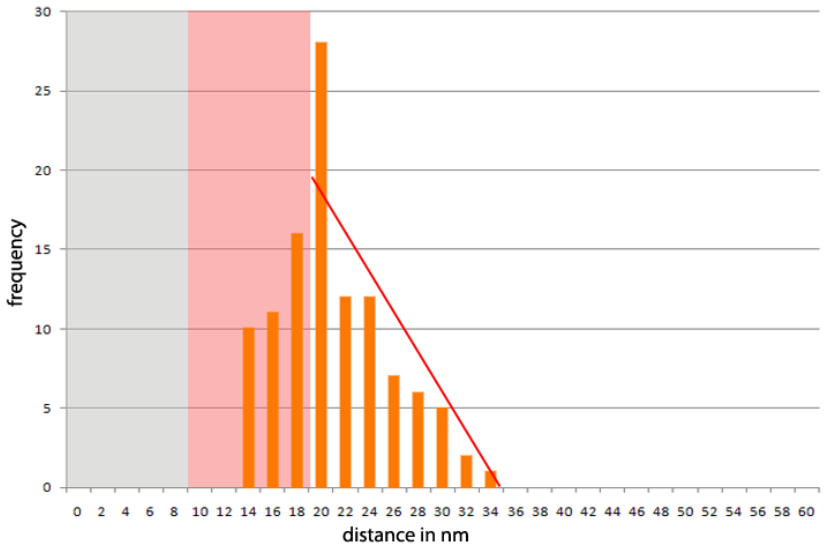

Figure 4.3.16: Distance of ribosomes to the membrane for four 72 h tomograms with equal cell diameter. Grey: Area where no ribosomes can be located by their center of mass. Red: Predicted decay due to the masking during the template matching process and the missing wedge effect. The predicted model is shown as a red line.

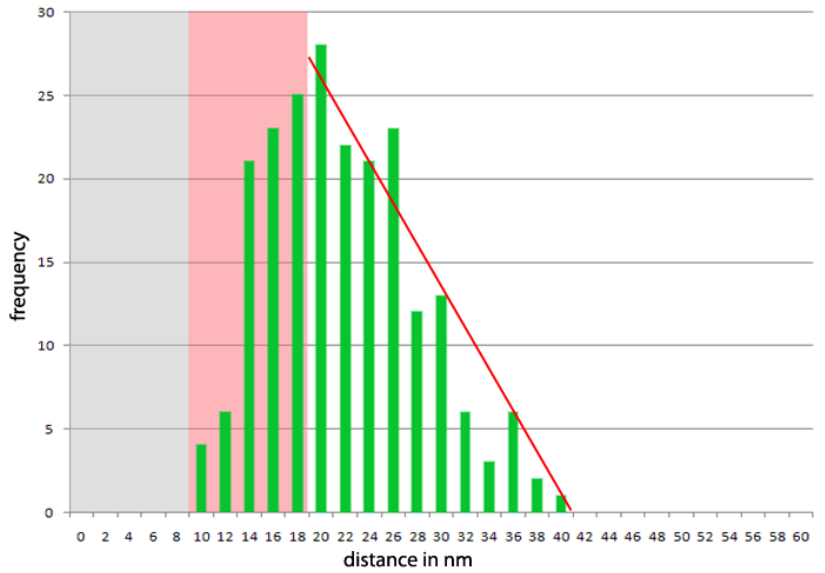

Figure 4.3.17: Distance of ribosomes to the membrane for four 120 h tomograms with equal cell diameter. Grey: Area where no ribosomes can be located by their center of mass. Red: Predicted decay due to the masking during the template matching process and the missing wedge effect. The predicted model is shown as a red line.

The five tomograms from logarithmic phase contained at total of 513 ribosomes that show a statistical uniform distribution concerning their distance to the cell membrane with some slight over-representation of medium distances on the expense of longer distances when compared to the predicted model (figure 4.3.15). The maximum number of ribosomes are in a distance of 24 nm to the cell membrane.
The 141 ribosomes from the four stationary phase tomograms and the 239 ribosomes from the five starvation phase tomograms also show a uniform distribution. The highest frequency is here at 20 nm distance (figure 4.3.16 and 4.3.17). Compared to the model, there is an over-representation of medium distances to the membrane in the 72 h cells (figure 4.3.16). This over-representation is also seen for the 120 h cells (figure 4.3.17), where distances between 20 and 26 nm seem to be preferred and distances between 28 and 34 nm are under-represented. This indicates that in starving cells the ribosomes are more excluded from the center of the cell. However, in general the data follow the predicted model and the differences are not significant. The model was calculated only for the white area.
There is an area with distances from 9 to 18 nm from the mebrane, where a decay is predicted (figure 4.3.13**B**). This is due to two technical issues: First, During the template matching process the membrane was masked maually where some cytosolic parts were excluded from the analyzed volume and second, the missing wedge effect. The data for all three growth phases follows this predicted decay.

4.3.4 Neighboring of Ribosomes

Ribosomes can form defined structures inside cells that relate to the direct neighboring of two or more ribosomes. In logaritmic phase *E. coli* cells, the formation of polysomes could be observed, in starving *E. coli* cells dimers were present.
To investigate if *S. citri* also forms neighboring structures in its different growth states, the distance of the center of mass of each ribosome to its closest neighbor was plotted (figure 4.3.18). The relative orientations of the next neighbors were plotted to determine if there is a preferred orientation.

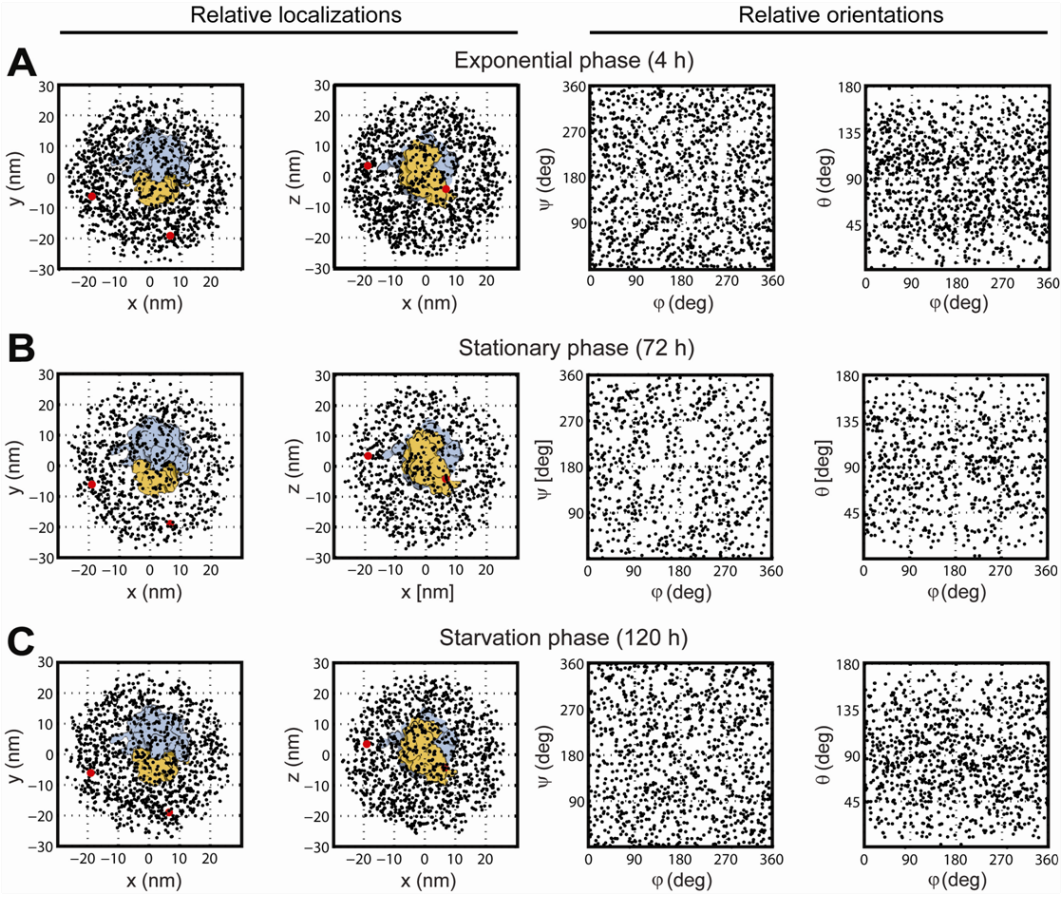

Figure 4.3.18: Analysis of the clustering and orientation of the ribosomes in different growth phases. A) Logarithmic phase (4 h). B) Stationary phase (72 h). C) Starvation phase (120 h). The red dots mark exit sites.

No formation of neighbouring structures could be observed in neither of the growth states. There are no accumulations of neighbors around the exit sites of the mRNA (red dots) like it would occur if polysomes were present and there are no clusters close to the 30S subunit like shown for dimers. The orientation of the closest neighbors does not show any preference but ist isotropically distributed.

4.3.5 Density of Ribosomes in the Cell

The number of ribosomes per tomogram was read out from the motiflists to calculate the ribosome density in the visible section of the cell.

Number of ribosomes per tomogram

Logarithmic phase		Stationary phase		Starvation phase	
tomogram	number of ribosomes	tomogram	number of ribosomes	tomogram	number of ribosomes
t1	69	t1	55	t1	28
t2	97	t2	71	t2	22
t3	113	t3	74	t3	53
t4	124	t4	82	t4	54
t5	97	t5	45	t5	56
t5	137	t5	49	t5	63
t7	93	t7	83	t7	43
t8	120	t8	32	t8	60
t9	99	t9	38	t9	44
t10	114	t10	28	t10	41
t11	121	t11	27	t11	47
t12	124	t12	44	t12	38
		t13	60	t13	46
	1308		688		595

Figure 4.3.19: Number of ribosomes per tomogram for the three different growth states.

For the logarithmic phase 12 tomograms were recorded and analyzed, for the stationary and the starvation phase 13 each. In total, 38 tomograms were analyzed. The number of ribosomes changes significantly from exponentially fast growing cells to stationary cells or even starving cells. The total ribosome number of 1308 for 12 different 4 h tomograms gives a value of 109 ribosomes per tomogram on average. For 72 h this average is 53 ribosomes per tomogram, which is a decrease of 50%. 120 h tomograms show an average of 46 ribosomes per tomogram.

To obtain an estimate for the ribosome density per μm^3 cell volume, the volume of the visible part of the cell was calculated. For the 4 h cells the cell volume was calculated based on simulated projections of a membrane model. The membranes were modeled in 3dsmax (Autodesk,USA) [1] considering the curvature of manually segmented membranes from experimental tomograms (figure 4.3.20). The modeling, which fills up the membrane region affected by the missing wedge, was necessary for a more accurate estimation of cellular volume. The calculation of the cell volume was done for five cells per growth phase.

[1] kindly done by Julio Ortiz

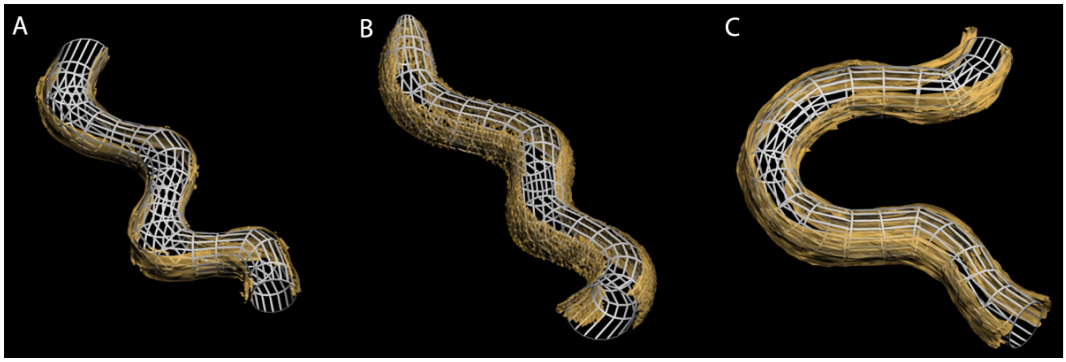

Figure 4.3.20: Volume determination of logarithic phase cells by modeling the membrane. A) to C) Example for three different membrane models based on the manually segmented membranes from the experimental data.

Although the cells differ in their appearance and their curvature, the calculated volume of all cells within one state is very similar. The volume of the visible part of the cell, the ribosome number and the ribosome density per μm^3 are stated in the following tables.

tomogram	cell volume $[\mu m^3]$	number of ribosomes	ribosome density $[(\mu m^3)^{-1}]$	percentage $(V_{Ribo}/\ V_{cell})$
t1	0.013	69	5307	1.8
t2	0.009	97	10777	3.6
t3	0.011	113	10272	3.5
t4	0.014	124	8857	3.0
t5	0.013	78	6000	2.0

Table 4.3.1: Cell volume and occupation by ribosomes for the 4 h cells.

With an estimated ribosome volume of 3400 nm^3 [105] the percentage of ribosome occupation inside the cell was calculated.

The cell volume for the stationary and starvation phase cells was calculated assuming a cylindrical form as these cell are not helical.

tomogram	cell volume [μm^3]	number of ribosomes	ribosome density [$(\mu m^3)^{-1}$]	percentage (V_{Ribo}/ V_{cell})
t1	0.006	28	4666	1.6
t2	0.006	38	6333	2.1
t3	0.009	49	5444	1.8
t4	0.007	45	6428	2.1
t5	0.010	55	5500	1.9

Table 4.3.2: Cell volume and occupation by ribosomes for the 72 h cells.

tomogram	cell volume [μm^3]	number of ribosomes	ribosome density [$(\mu m^3)^{-1}$]	percentage (V_{Ribo}/ V_{cell})
t1	0.006	38	6333	2.1
t2	0.010	47	4700	1.6
t3	0.008	44	5500	1.9
t4	0.006	41	6833	2.5
t5	0.007	46	6570	2.2

Table 4.3.3: Cell volume and occupation by ribosomes for the 120 h cells.

4.4 Ribosome Morphology

4.4.1 3D Averaging of Ribosomes and Resolution Determination

The selected particles were 3D-aligned and averaged. The resolution was determined for the particles from the 4 h state. The derived structure had a resolution of 2.08 nm (figure 4.4.1). Resolution criterion was the Fourier shell correlation coefficient at 0.5. Therefore, the Fourier shell coefficient of two independent averages of each 50 % of the particles was calculated. The orientation coordinates of the detected particles are spread among the full angular range. This indicates that the complete structure is sampled isotroply and is independent of the missing wedge effect.

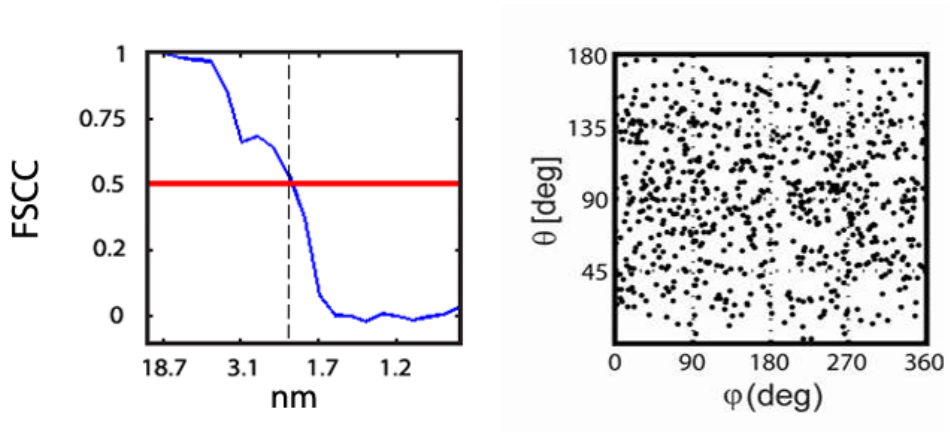

Figure 4.4.1: Determination of the resolution and distribution of the ribosomes in the tomogram (4 h). A) Resolution determined by the Fourier shell correlation coefficient as 2 nm. Plot of the Euler angle Θ against Euler angle ϕ. The orientation of the ribosomes is evenly distributed over the full angular range.

4.4.2 Comparison of Ribosome Morphologies

The 3D averages of the ribosomes recovered from tomograms of 4, 72 and 120 h samples show different features depending on the growth state.

There are two features that stand out in the 3D average from 4 h ribosomes compared to the other structures (indicated by arrows in figure 4.4.2). There is one extra density on the right side of the ribosome to which the elongation factor is supposed to bind during translation. The second feature is an extra density at the back of the ribosome that looks like a tube. Also the 'handle' that is located at the left side of the ribosome is most dominant in the 4 h structure.
Compared to the template structure from *E. coli* the *S. citri* structure looks broader and more massive.

The structures were normalized with 'mean 0 plus one standard deviation' and difference maps were calculated to emphasize the differences between the structures derived from the growth states. The difference maps are shown in figure 4.4.3. The densities that are not present in the subtracted structure are shown in red, densities that are only visible in the subtracted structure are shown in green.

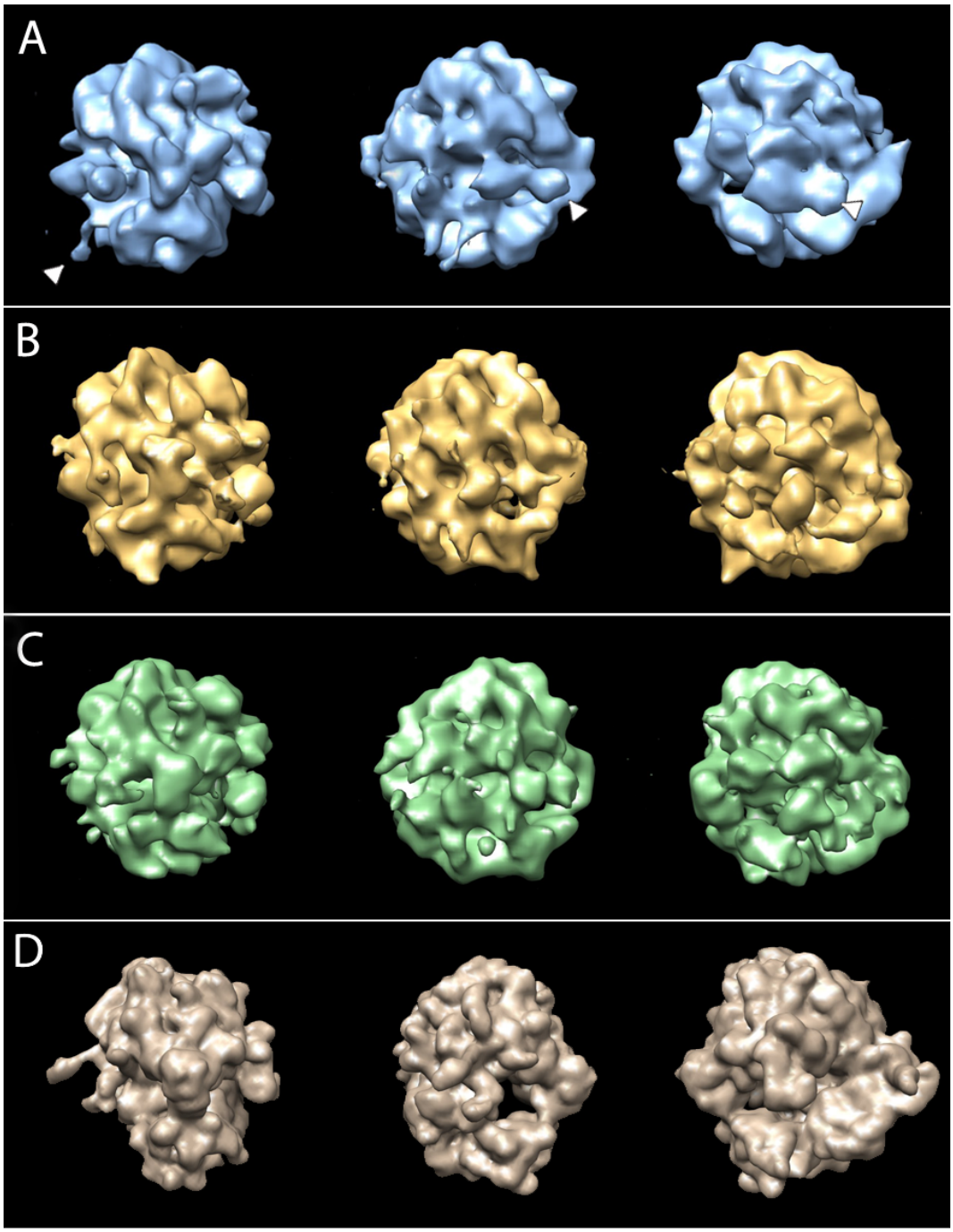

Figure 4.4.2: 3D average of ribosomes from different growth states. From left to right: front, left side, right side. A) ribosome structure from 4 h sample. B) ribosome structure from 72 h sample. C) ribosome structure from 120 h sample. D) Template from *E. coli* filtered to a resolution of 2 nm.

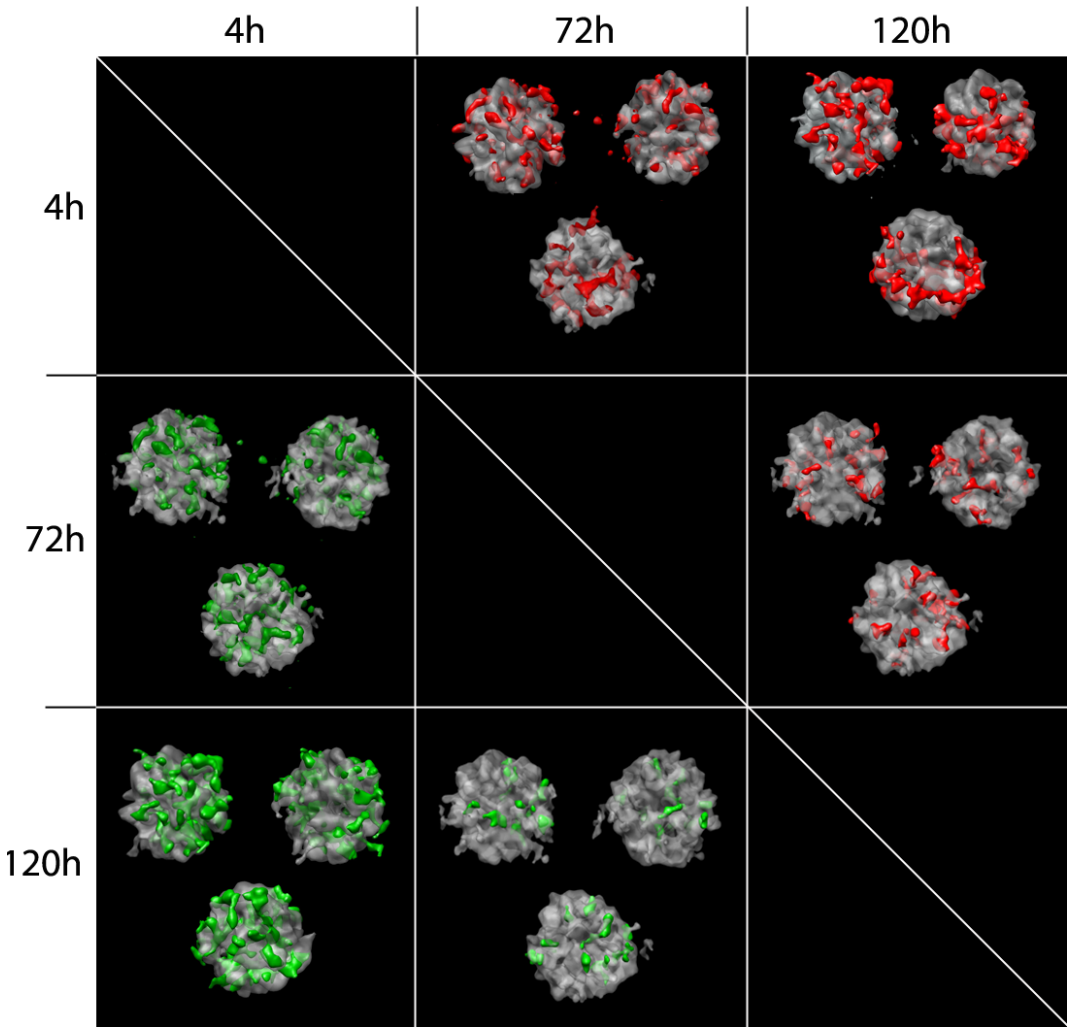

Figure 4.4.3: Difference maps of the structures derived from the different growth states. Each structure of the upper row was subtracted by the according structure of the vertical column. Densities that are missing in the initial structure are shown in red, densities that are only present in the initial structure are shown in green. Inside the table: upper left: front view; upper right: left side view; lower middle: right side view.

The most striking differences are seen between the average of the 4 h cells and the average of the 120 h cells. The averages of the 72 h cells compared to the 120 h cells show least differences.

A Fourier shell correlation (FSC) was calculated for every average pair and for every average with the reference structure. Results are shown in figure 4.4.4, the 0.5 criterion is stated in Angstrom. In this case, the FSC is used as a measure for similarity or difference between the averages, with a low FSC value indicating a similarity and a high FSC value indicating a difference.

	4h	72h	120h	reference
4h		43	43	68
72h			38	44
120h				44
reference				

Figure 4.4.4: Comparison of the similarities/ differences of the 3D averages using the 0.5 criterion of the FSC. The values are stated in Angstrom.

The values indicate, that there is a higher similarity of the 72 h average compared to the 120 h average, than between the 4 h average and the two other states. The FSC values that compare the reference to the 3D averages obtained from the data show a very high difference between the reference and the 4 h average, but only a medium difference to the 72 h and the 120 h average.

To make sure that there was no bias of the template and that all features are exclusively derived from the data, the 3D average was compared to the template like it was used in molmatch.

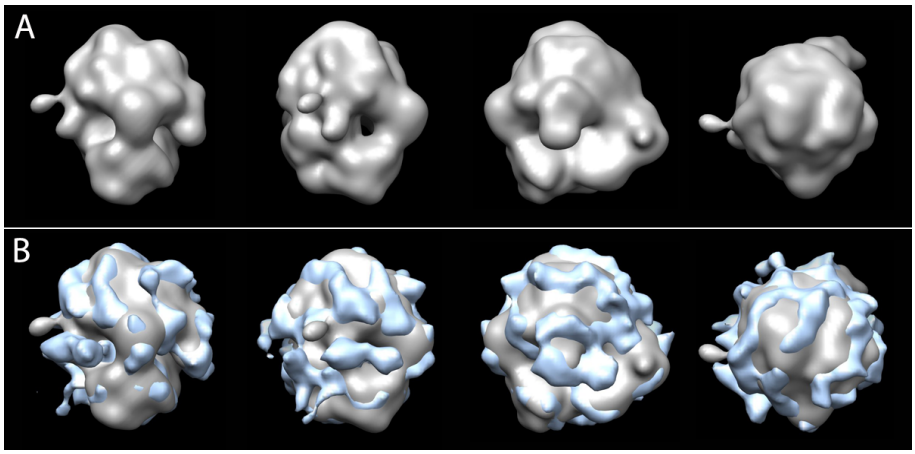

Figure 4.4.5: Comparison of the template used for template matching and the emerged 3D average of the 4 h ribosomes. From left to right: front, left side, right side, top. A) Template from *E. coli* with a resolution of 5 nm. B) template merged with the 3D average derived from the 4 h ribosomes.

Figure 4.4.5 shows that the extra densities attached to the ribosome structure of the 4 h samples are not influenced by the template. All three features, the 'handle' on the left side, the 'tube' at the back and the extra density at the elongation factor binding site are derived from the data.

5 Genetic Tools for Visualizing Macromolecules in *S. citri*

5.1 Expression of Heterologous Genes in *S. citri*

Expression of foreign genes in an organism as thin as *Spiroplasma citri* bears numerous advantages. The structure of complexes can be determined in a close-to-native environment without potential artefacts resulting from lysis, purification or crystallization.

5.1.1 Creating an Expression Vector with Suitable Restriction Sites

To express foreign genes, we designed expression vectors based on the pSD4 plasmid, a derivate of the natural *Spiroplasma* plasmid pSpi6. The pSD4 vector (figure 5.1.1) was kindly provided by Joel Renaudin and Sybille Duret (INRA, Bordeaux). This original vector contained the tetracyclin resistance gene TetM, the full origin of replication sequence (OriC) and a dnaN promotor sequence on a pSpi backbone.

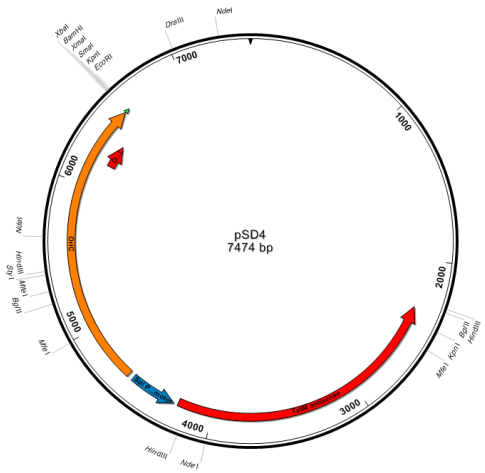

Figure 5.1.1: Vector map of pSD4. Orange: OriC region with dnaN promotor, blue: Spiralin promotor for TetM, red: TetM

As proteins of interest, Tripeptidylpeptidase II (TPPII) and GFP were chosen, TPPII for its characteristic size and shape and GFP for its detectability by fluorescence microscopy. As the pSD4 vector does not contain a multiple cloning site suited for our purposes, alternative cloning strategies were applied. In a first attempt, *tppII* and *gfp* were amplified by PCR adding a HaeIII site to both ends. The vector was cut at the BamHI site and subsequently treated with Klenow fragment, thereby creating a blunt end. Blunt-end ligation was performed under different conditions, including insert overspill, molar ratio one to one and PEG mediation, but turned out to be not successful.
Therefore, two new restriction sites were added to the vector by CCR, NheI and NotI (figure 5.1.2**A**). First a casette of approximately 400 bps was amplified from the pSD4 vector by PCR, adding a BamHI site to the 5'-end and a DraIII site to the 3'-end. A first round of CCR was performed to add a NheI site downstream the BamHI site. The CCR product was purified and used as template for the second round of CCR where a NotI site was added downstream the new NheI site. The second CCR product was purified and cut with BamHI and DraIII in parallel with the pSD4 vector. The digested insert was ligated to the BamHI/ DraIII precut pSD4 vector, resulting in a new vector pSD5. This new vector was then transformed into *E. coli* Top10.
Ten colonies of the transformants were picked, precultures were grown and the plasmids were purified. Control digests were performed with NheI and DraIII and with NotI and DraIII (figure 5.1.2**B**).

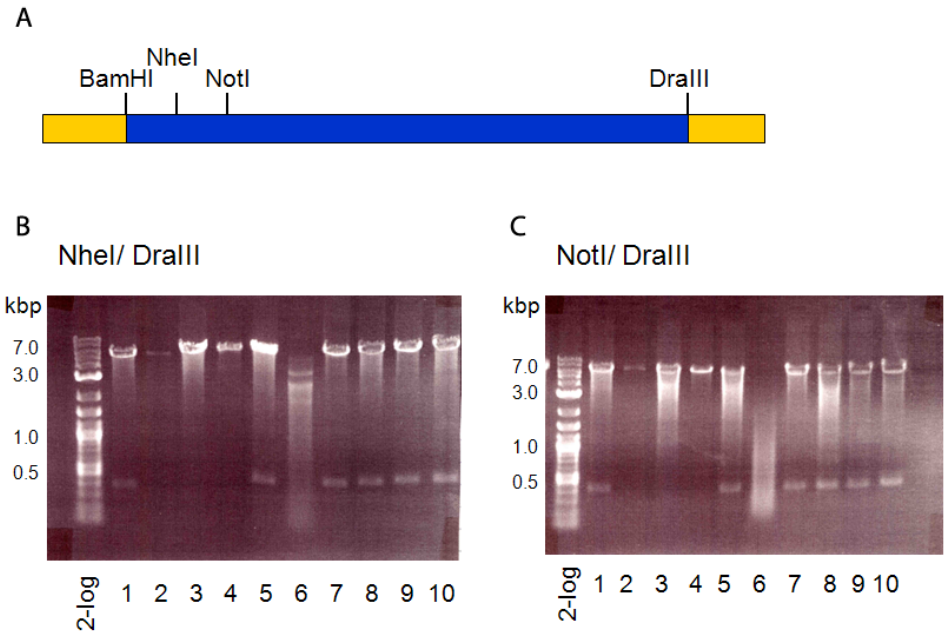

Figure 5.1.2: The new vector, pSD5, was digested with NheI/ DraIII and NotI/ DraIII. A) Schematic drawing of the cloning cassette. B) Control digest of pSD5 with NheI/ DraIII. C) Control digest of pSD5 with NotI/ DraIII.

As seen in figure 5.1.2**B** and **C**, six of the ten isolated plasmids show the expected band of 400 bps for both, the NheI and the NotI control digest. The plasmid used in lane 10 was sequenced and used for further experiments.

5.1.2 Cloning of TPPII and GFP into the pSD5 Expression Vector

The *tppII* and *gfp* structural genes were amplified by PCR, adding a NheI site to the 5'-end and a NotI site to the 3'-end. The genes of interest and the expression vector were cut with NheI and NotI and the inserts were ligated to the vector. The ligated vector was transformed into *E.coli* Top10. Ten colonies were picked for each sample and precultures were grown to isolate the plasmids.
For control digestion, BamHI was used. Expected fragment sizes for correct insertion are shown in figure 5.1.3.

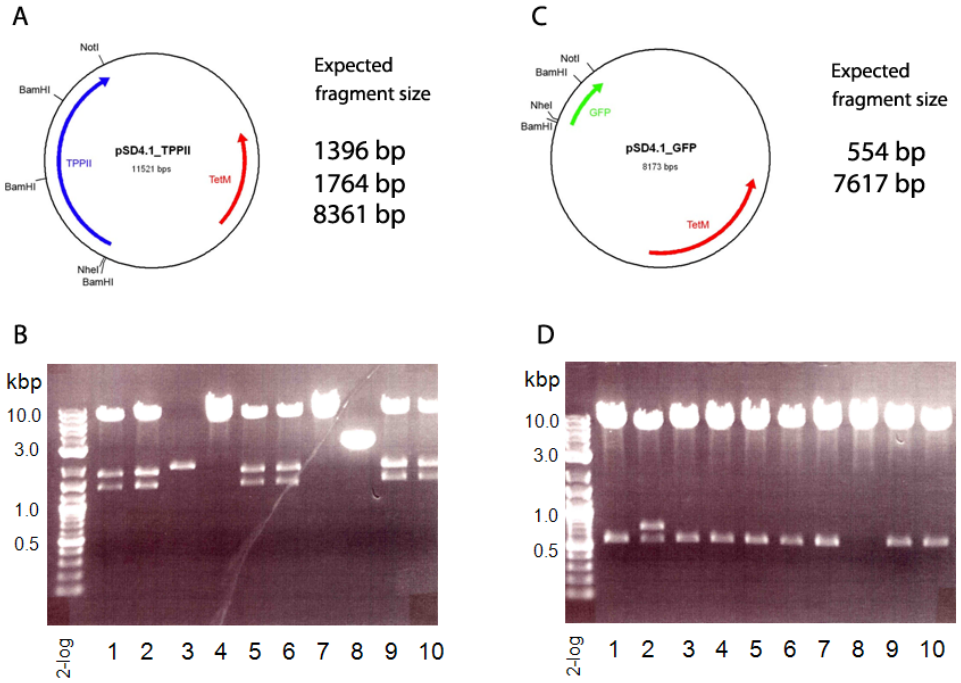

Figure 5.1.3: Control digest of pSD_TPP and pSD_GFP with BamHI. A) vector map of pSD_TPPII and expected fragment size. B) vector map of pSD_GFP and expected fragment size. C) Agarose gel of pSD_TPPII control digest. D) Agarose gel of pSD_GFP control digest.

For pSD_TPPII, six out of ten plasmids show the expected digestion pattern. For pSD_GFP, eight out of ten plasmids show the expected band sizes. pSD_TPPII(2) and pSD_GFP(1) were sequenced and used for transformation into *S. citri*.

5.1.3 Transformation of Plasmid DNA into *S. citri*

Transformation of plasmid DNA into *S. citri* was optimized by combining several transformation approaches. The original protocol described in [19] had to be adapted to the technical equipment used in this work. For chemical transformation, the Calcium-chloride-method [58], the Kushner-method [48], the PEG-mediated [45] and the liposome-mediated [101] method were used.

Transformation by electroporation was done using a BioRad Genepulser XCell. In contrast to the old Genepulser (used in [19]), the lowest possible electric capacity is 10 μF instead of 2.5 μF. This causes a differing transformation profile and the optimal condi-

tions had to be determined.
Electroporation with 2 pulses per sample was the most favorable method. An obtained time constant of about 6.5 ms turned out to result in efficient transformation. The incubation time of 3 h before plating was sufficient, longer incubation (over night) did not result in more colonies. After three weeks of incubation, ten colonies were picked from each sample and transferred to liquid medium. The presence of the vector was verified by PCR. The optimized electroporation protocol yielded about 80% positive clones.

5.1.4 Redesigning the Expression Vector: Checking Transcription and Translation

The presence of vector pSD_TPPII and pSD_GFP in the transformed cells was verified by PCR. The expression of the target proteins was checked by Western Blot but could not be confirmed. Fluorescence microscopy with *S. citri*[GFP] did not show any fluorescence signal.
It was therefore assumed, that no protein expression was mediated by the vector used. In the following, a vector with a different promotor sequence was designed and generated. As new promotor the spiralin promotor (pspi), that drives the endogenous expression of *S. citri*'s most abundant membrane protein, Spiralin, was used (figure 5.1.4**A**). Additionally, the distance between the Shine-Dalgarno motif and the start codon was varied between 6 and 16 base pairs for the case that translation initiation requires either a short, medium or long distance in *S. citri* (figure 5.1.4**B**).

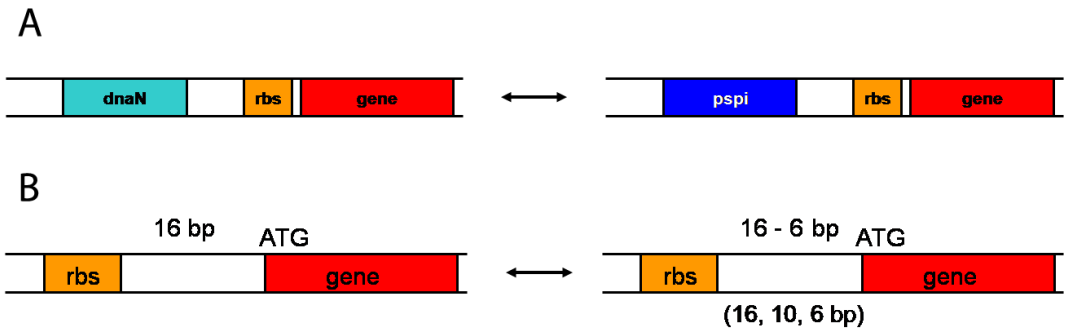

Figure 5.1.4: Changing the promotor and length of translation initiation region. A) The dnaN promotor is replaced by the spiralin promotor. B) The distance between Shine-Dalgarno sequence and start codon is set to 16, 10 or 6 bps.

The resulting vectors were called pSD6, pSD10 and pSD16 for the dnaN promotor and

pSpP6, pSpP10 and pSpP16 for the spiralin promotor. Only GFP was cloned into the vectors mentioned and transformed into *S. citri* GII-3. Protein expression was checked by Western Blotting.

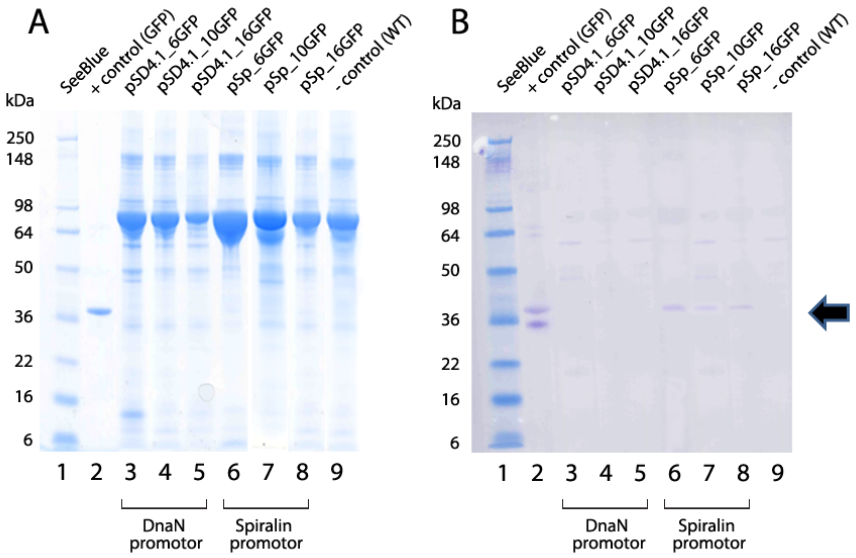

Figure 5.1.5: SDS gel and Western Blot for pSDs and pSPs expressing GFP. A) SDS Gel. B) Western Blot

Figure 5.1.5 shows only very faint bands for the SDS gel, but in the Western Blot the band corresponding to GFP is clearly seen in all three lanes for the spiralin promotor vector. None of the vectors holding the dnaN promotors expresses GFP.
This means that the spiralin promotor was able to drive the expression of a foreign gene in *S. citri* and that the distance between Shine-Dalgarno sequence and start codon is not crucial in this organism and can vary from at least 6 to 16 bps.

5.1.5 Fluorescence in *S. citri*

The transgenic *S. citri* cells expressing GFP were used for fluorescence experiments. Fluorescence microscopy was performed but no fluorescence signal could be detected.
As GFP was verifiably expressed in these cells, either protein folding or a lack of oxygen were suspected to be the reason for the missing fluorescence. To examine if the oxygen present in the facultatively anaerobically growing *S. citri* cells is sufficient for GFP to build a functional chromophoric center, *E. coli* cells expressing the same GFP were cultured under standard *E. coli* conditions (37 °C, shaking at 180 rpm) and under *S. citri* conditions (32 °C, no shaking) from the moment of induction. GFP expression was

induced with 1 mM IPTG. Expression was allowed for 1 h, then fluorescence microscopy was performed.

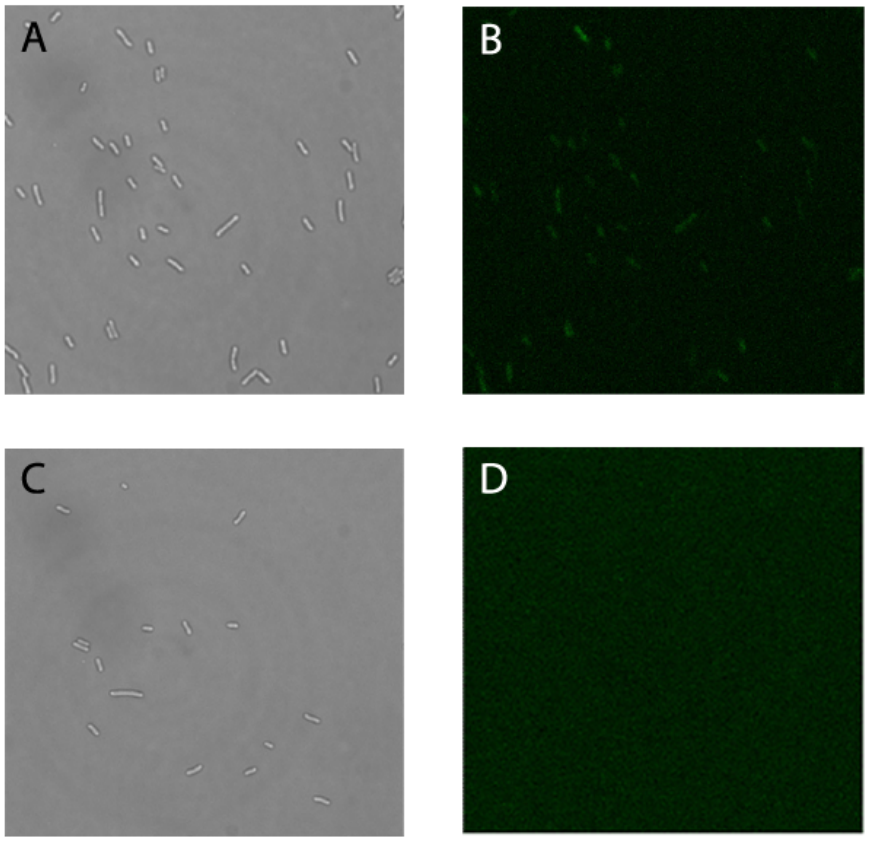

Figure 5.1.6: *E. coli* expressing GFP under aerobic and partly unaerobic conditions. A) *E. coli* expressing GFP under standard *E. coli* conditions; light channel B) *E. coli* expressing GFP under standard *E. coli* conditions; fluorescence channel C) *E. coli* expressing GFP under standard *S. citri* conditions; light channel D) *E. coli* expressing GFP under standard *S. citri* conditions; fluorescence channel

In figure 5.1.6 it can be clearly seen, that *E. coli* expressing GFP under standard aerobic conditions can be detected in the fluorescence channel, whereas *E. coli* expressing GFP under *S. citri* conditions does not show a fluorescence signal. Although *S. citri* grows only facultatively anaerobically without shaking, the results suggest that the oxygen present in the medium is not sufficient to activate the GFP chromophor.

GFP is therefore not suitable for fluorescence experiments in *S. citri* in general.

Drepper *et al.* [17] reported a flavinmononucleotide-based fluorescent protein (FbFP)

that is oxygen-independent. We used this FbFP (subtype Bs1) to replace GFP in our constructs and to obtain fluorescent *S. citri* cells. First, FbFP(Bs1) was cloned into a pET17b vector and again expressed in *E. coli* under aerobic and facultatively anaerobic conditions.

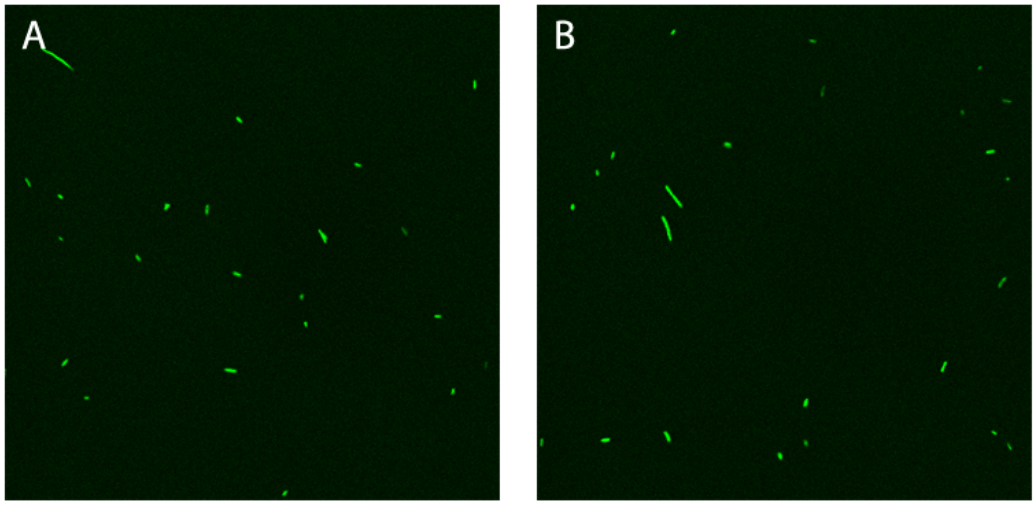

Figure 5.1.7: *E. coli* expressing FbFP under aerobic and partly unaerobic conditions. A) *E. coli* expressing FbFP under standard *E. coli* conditions. B) *E. coli* expressing FbFP under standard *S. citri* conditions.

In figure 5.1.7 it can be seen, that FbFP is easily detectable in *E. coli* under aerobic as well as under partly anaerobic conditions. Moreover, the fluorescence signal is much stronger than the previously observed GFP signal with less background which makes it easier to be detected in thin cells like *S. citri*.

Expression of FbFP in *S. citri*

FbFP(Bs1) was cloned into pSpP16 and the resulting vector was transformed into *S. citri*. For the fluorescence microscopy the cells were washed with HSO buffer to reduce the background signal attributed to the medium components. The cells were resuspended and placed on objective slides covered with an agar pad.

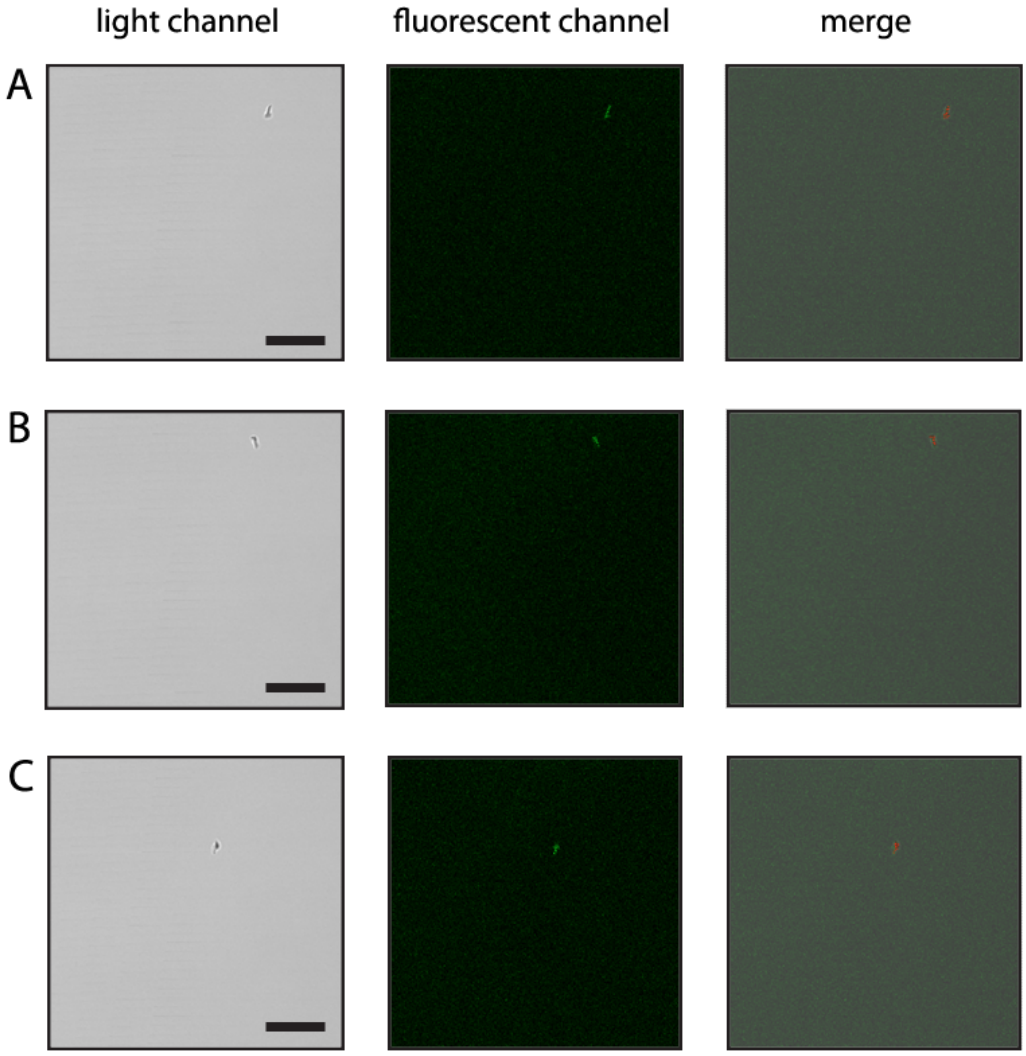

Figure 5.1.8: Fluorescence microscopy of *S. citri* expressing FbFP(Bs1). A) to C) Three different cell aggregates. Left column: fluorescence channel, middle column: light channel, right column: merge. Scalebar corresponds to 20 μm.

The three samples depicted in figure 5.1.8 show no single cells but aggregates of a few cells. These aggregates are caused by the centrifugation during the washing procedure. Nevertheless all three show a fluorescence signal where the cell aggregate is located. This indicates that expressing FbFP(Bs1) causes a detectable fluorescence signal in *S. citri*. Unfortunately, this signal is not very prominent and further optimization has to

be done to use FbFP-based fluorescence in *S. citri* on a regular basis.

Expression of TPPII and 20S Proteasome in *S. citri*

Although the transformation of *S. citri* with pSpP_TPPII was successful, the cells lost the vector on average after four passages. Therefore, an improved vector for constitutive expression was designed and cloned in order to decrease the vector size.
The OriC site was cut and replaced by a shorter OriC fragment which was shown to be the shortest functional OriC sequence in *S. citri* [19].
The dnaN promotor was replaced by the Spiralin promotor. Downstream of the promotor sequence a new multiple cloning site (MCS) was inserted.
As target protein, TPPII and the 20S proteasome from *T. acidophilus* (TAP) were used. The TAP sequence was amplified by PCR from the host vector pRSET5a_TAP, flanked with NheI and the *Spiroplasma* ribosome binding site at the 5'-end and the *Spiroplasma* stop codon and NotI at the 3'-end. The PCR product was cloned into the newly designed vector pSpi.
TAP consists of two different subunits that are arranged on the vector in an operon with the alpha subunit downstream of the beta subunit. This RBS upstream of the alpha-subunit is from *E. coli* and was therefore mutated to the *S. citri* sequence using the Quick Change Kit.
The resulting vectors pSpi_TPPII and pSpi_TAP were transformed into *S. citri* and 10 colonies were picked in each case from the resulting plates.
The presence of the vector was verified after four passages in liquid medium. For pSpi_TAP 6 out of 10 samples held the vector, for pSpi_TPPII 4 out of 10 did. Transcription of the target genes was then proven by RT-PCR (figure 5.1.9). Prior to writing the cDNA using a reverse transcriptase, DNA contamination was removed by DNase digestion.

The result of the RT-PCR is only reliable if there is no remaining DNA in the RNA sample from which amplification of the target sequence could occur. Figure 5.1.9 shows that no DNA residues were present in the sample and that TAP mRNA presence could be verified in all six clones. For TPPII the presence of mRNA could be proven for 3 out of 4 clones (figure 5.1.10).

Expression of the target proteins was first checked by Dot Blotting. Thereby the cells were just lysed and the lysate was brought in drops on a nitrocellulose membrane.

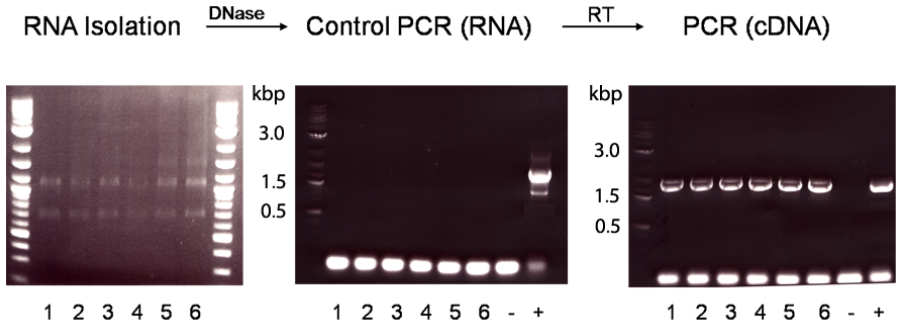

Figure 5.1.9: RT-PCR of TAP in transgenic *S. citri*. Left: Isolated RNA. Middle: PCR after DNase digest. Right: PCR on cDNA. -: negative control without cDNA, +: positive control, pSpi_TAP.

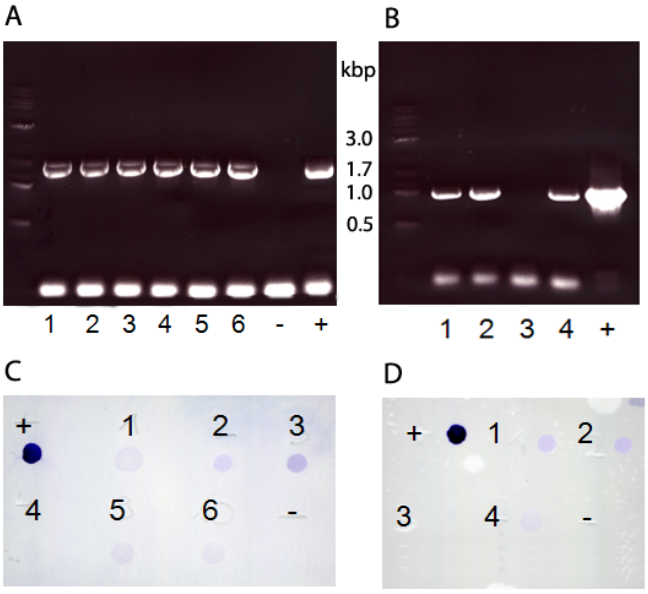

Figure 5.1.10: RT-PCR and Dot Blot of TAP and TPPII in transgenic *S. citri*. A) and B) mRNA amplified from the samples with TAP and TPPII primers respectively. -: negative control without cDNA but with primers. +: positive control (expression vector) C) and D) Dot Blot analysis of the lysed cells. For TAP detection an anti-His antibody was used, for TPPII detection an anti-dTPPII antibody was used.

Both, TPPII and TAP can be detected in the cell lysate of transgenic *S. citri* (figure 5.1.10**C** and **D**). All samples that transcribe mRNA of the target protein also translate the protein. To exclude an unspecific interaction of the respective antibodies with components of the cell lysate, a Western Blot was performed for one representative of

each sample. For TPPII, sample number 2 was chosen (figure 5.1.11), for TAP sample number 3 (figure 5.1.12).

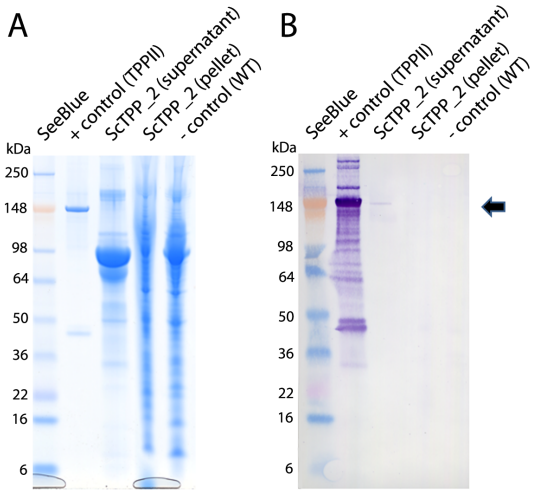

Figure 5.1.11: SDS gel and Western blot of TPPII expressing *S. citri*; sample number 2. A) SDS gel B) Western Blot

Although there is nearly no band visible in the sample lane of the SDS gel, the Western Blot shows a faint band at the apparent molecular mass of TPPII (150 kDa). This means that TPPII was successfully expressed in *S. citri*.

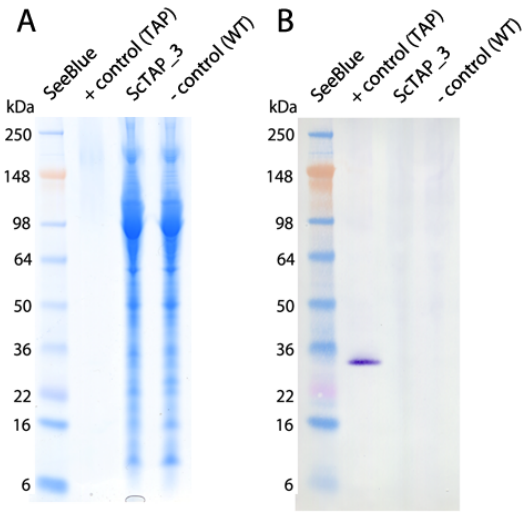

Figure 5.1.12: SDS gel and Western blot of TAP expressing *S. citri*; sample number 3. A) SDS gel B) Western Blot

For TAP no band of respective size could be detected by Western Blotting. The samples for the Western Blot experiment were taken after 10 passages. A repeated check for the vector presence by PCR showed that all of the TAP clones had lost the vector.

5.1.6 Vectors for inducible Expression in *S. citri*

As the improved expression vector pSpi still tends to be lost after a few passages, an inducible vector was designed and generated. A better control over the expression of foreign genes was thought to reduce the stress for the cells, thereby inducing the cells to keep the vector for a longer period of time.

The Fru Promotor

For the design of an inducible vector an appropriate promotor is crucial. Gaurivaud et *al.* described the fructose operon of *S. citri* and identified the FruR gene as putative activator [30]. The fructose operon is organized like shown in figure 5.1.13.

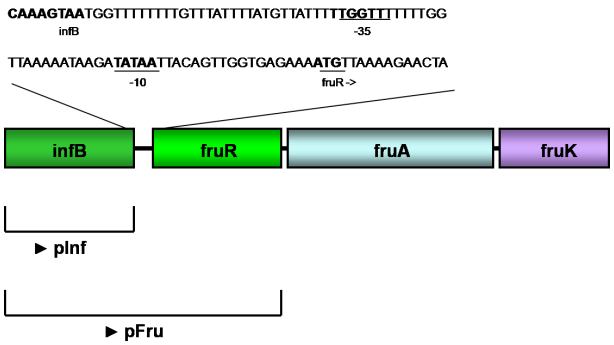

Figure 5.1.13: Organization of the fructose operon of *S. citri*. InfB acts as promotor region. Upstream of the FruR region the typical translation initiation sequences are found.

InfB acts as promotor upstream of the FruR region. Gaurivaud showed that FruR acts as enhancer upon exposition to fructose. Therefore two new inducible vectors were designed: pFP1, which has the FruR region adjacted to InfB and pFP2, which holds just the promotor region.

As both vectors originated from pSD4, the OriC region was cut and replaced by a short but functional OriC sequence of 163 bps. The dnaN promotor region was cut and replaced either with InfB or with InfB and FruR (figure 5.1.14). Both promotor regions were amplified from genomic DNA using appropriate primer pairs. One of the two PstI

restriction sites present on the vector was chosen for the cloning of the promotor region. The second PstI site, that is located within the TetM sequence, had to be mutated silently to remove the restriction site prior to the insertion of the promotor region.
A multiple cloning site (MCS) containing several standard restriction sites was added downstream of the promotor region. The MCS was synthesized as single strands with a forward and a reverse orientation. Both strands were annealed and the DNA was cut and cloned into the vectors.

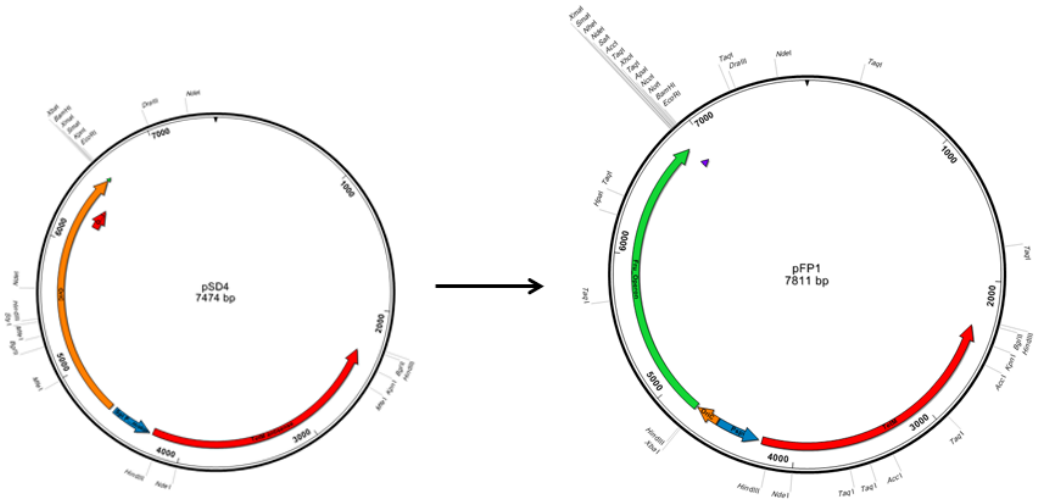

Figure 5.1.14: Designing the inducable vector pFP on the basis of pSD4. Red: The tetracyclin resistance gene TetM, blue: spiralin promotor for TetM, orange: OriC region, green: Fru promotor (either InfB + FruR or just InfB).

Both vectors, pFP1 and pFP2 were sequenced and then used for the cloning of target genes. These target genes were TPPII, TAP and all three variants of FbFP. The standard variant is Bs1 which is derived from the Gram-positive *B. subtilis* and was originally published. Bs2 is a shorter variant lacking a domain that reportedly caused trouble when expressing the protein in other organisms than *B. subtilis*. The third variant, Pp1 has a distinct sequence and was derived from the Gram-negative organism *Pseudomonas putida*. Although the sequence of this variant differs from the Bs variants, the fluorescence characteristics are the same, however, with a somewhat lower fluorescence yield.
As shown in chapter 5.1.5, Bs1 could be expressed and detected in *S. citri*. It should be tested if Bs2 or Pp1 show higher expression and/ or better fluorescence results.

The target genes were amplified from their host vectors by PCR, thereby flanking them with NheI and the *S. citri* ribosome binding site at the 5'- end and the *S. citri* stop codon and NotI at the 3'- end. The vectors and the inserts were cut with the mentioned restriction enzymes, ligated and transformed into *E. coli* Top10. Two colonies were picked from the corresponding plates and the plasmids were isolated. A control digest of the 10 different samples showed that 100 % of the cloned vectors inserted the gene of interest correctly (figure 5.1.15).

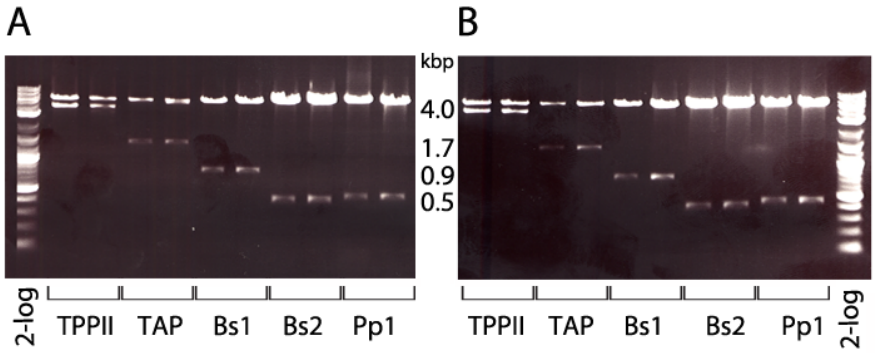

Figure 5.1.15: Control digest of the inducible expression vectors pFP1 and pFP2 with TPPII, TAP, Bs1, Bs2 and Pp1. A) Control digest of pFP1_TPPII, pFP1_TAP, pFP1_Bs1, pFP1_Bs2 and pFP1_Pp1 with NheI and NotI. B) Control digest of pFP2_TPPII, pFP2_TAP, pFP2_Bs1, pFP2_Bs2 and pFP2_Pp1 with NheI and NotI. The bands at 4000, 1700, 1000, 470 and 500 bps correspond to the restriction fragments of TPPII, TAP, Bs1, Bs2 and Pp1 respectively.

Fructose-free Medium

All papers that describe the work with *S. citri* in a fructose-dependent manner report a fructose-free medium based on a PPLO serum fraction that does not contain fructose. Unfortunately, this serum fraction is no longer available as the production was stopped in the 1970s. The standard medium for *S. citri* contains fetal bovine serum (FBS), which is also a source of fructose.

Therefore, a new fructose-free medium recipe without FBS had to be developed to perform experiments with a fructose-inducible promotor. On the other hand, FBS is the main source of cholesterol and BSA in the SP4 medium that was used by default so far. Those two components were added to the SP4 medium lacking FBS in different administration forms and different concentrations. The growth of the cells was monitored by recording growth curves via pH measurements (figure 5.1.16).

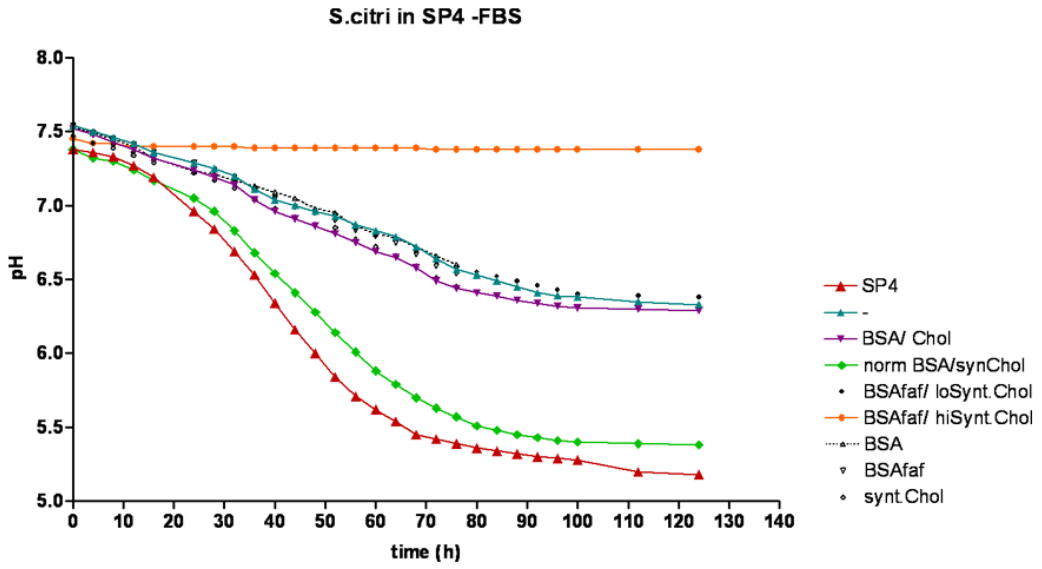

Figure 5.1.16: Growth curves of *S. citri* cells in SP4 medium lacking FBS. BSA was supplemented as standard BSA and fatty acid free BSA (BSAfaf) in different concentrations. Cholesterol was supplied as solution (diluted in EtOH) or as synthetic cholesterol for cell culture in different concentration.

Shown in red is the positive control of *S. citri* grown in SP4 medium with FBS. Nearly no cell growth takes place if fatty acid-free BSA is combined with very high concentrations of synthetic cholesterol (orange). Most combinations of BSA, fatty acid-free BSA and cholesterol obstruct cell growth distinctly, but BSA seems to support cell growth slightly better than fatty acid-free BSA (purple).
The best results were obtained when combining BSA with medium concentrations of synthetic cholesterol (green). The respective growth curve is very similar to the control. This combination was used as liquid medium and agar plates for transformation experiments with inducible vectors.

Inducing Protein Expression in *S. citri*

The inducible vectors pFP1 and pFP2 holding the genes of interest were tranformed into *S. citri* by electroporation. The colonies took longer to grow on the plates and 10 of them were picked for each sample and grown in liquid medium.
Unfortunately the picked colonies did not contain the vector and further experiments could not be performed.

5.2 Tagging of Proteins

In addition to the expression of foreign genes in *S. citri*, an approach of tagging endogenous proteins with fluorescent labels was performed. For this purpose, the integration vector pGOT [19] was used. This vector enables the addition of a fluorescent tag to the gene of interest by the following strategy: Transformants are first screened for their resistance to gentamycin and then site-specific recombinants are selected for their resistance to tetracyclin, which can only be expressed through recombination at the target gene sequence (figure 5.2.1).

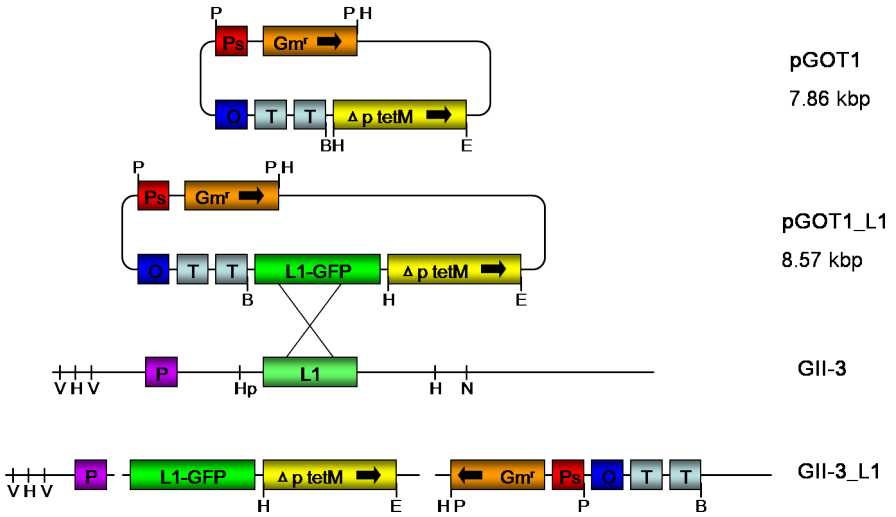

Figure 5.2.1: Two-step strategy for specific gene targeting in *S. citri*. First the transformants are selected by their resistance to gentamycin. Subsequently, positive recombinants are selected by their resistance to tetracylin that only appears after integration at the chromosomal target gene site.

As target genes, two ribosomal proteins were chosen, L1 and L29. This aims at detecting ribosomes by fluorescent microscopy in addition to the template matching approach described in chapter 4. Although no single molecules can be resolved, a distribution pattern should be visible.

In a first step, a C-terminal fragment of L1 and the full length L29 were inserted to the vector via the BamHI restriction site. The target sequences were amplified by PCR from genomic DNA, thereby flagging it with a BamHI site at the 5'- end and a BamHI and a NheI site at the 3'- end.
As there is only one restriction site involved, the insert can be integrated into the vec-

tor in two different orientations: in 5'-3'-direction (correct) or 3'-5'-direction (inverse). After transformation, seven colonies were picked for pGOT_L1 and six colonies for pGOT_L29. The plasmids were isolated and a control digest with HindIII was performed.

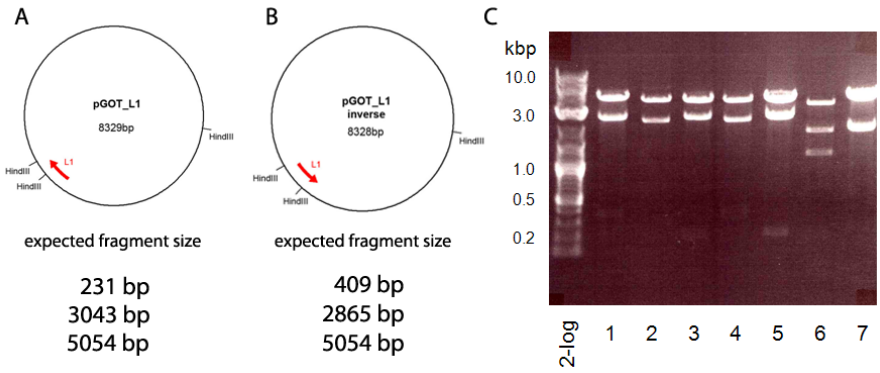

Figure 5.2.2: Control digest of pGOT_L1 with HindIII. A) and B) Vector map with L1 inserted in correct or reverse orientation. The expected fragment sizes are stated. C) Agarosegel of seven digested samples

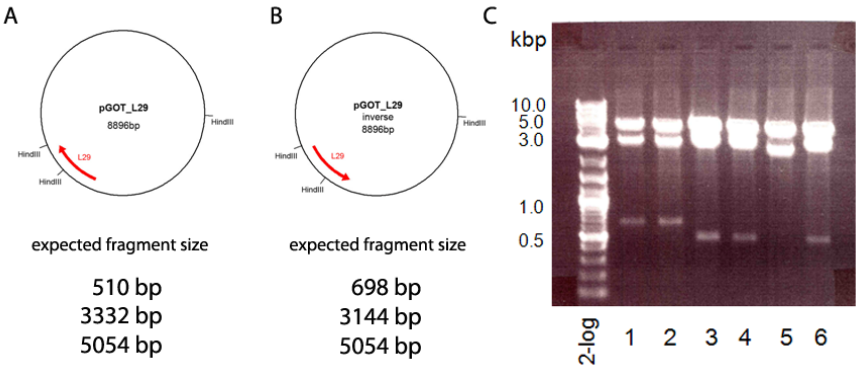

Figure 5.2.3: Control digest of pGOT_L29 with HindIII. A) and B) Vector map with L29 inserted in correct or reverse orientation. The expected fragment sizes are stated. C) Agarosegel of six digested samples

Figure 5.2.2 shows that for pGOT_L1 two out of seven samples (lane 3 and 5) inserted the target sequence correctly. For pGOT_L29 three out of six samples show the correct orientation.

In a second step, first GFP and later all three variants of FbFP were amplified with

a 12 amino acid linker and a flanking NheI restriction site and inserted into the NheI site downstream of the L1 or L29 sequence. Again, there are two possible orientations and the insertion was examined by a control digest with MfeI.

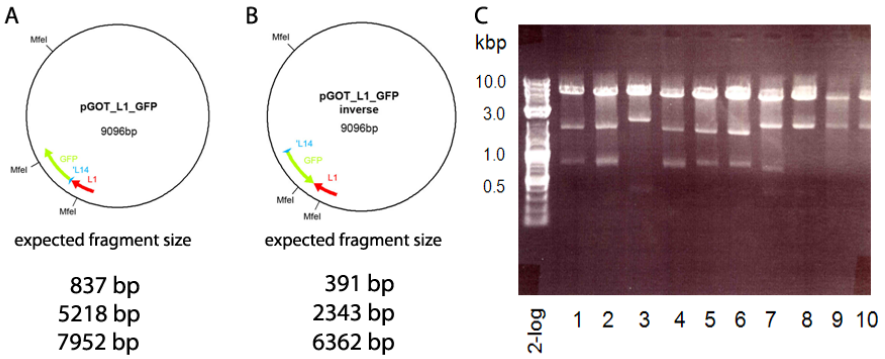

Figure 5.2.4: Control digest of pGOT_L1_GFP with MfeI. A) and B) Vector map with GFP inserted in correct or reverse orientation. The expected fragment sizes are stated. C) Agarosegel of ten digested samples

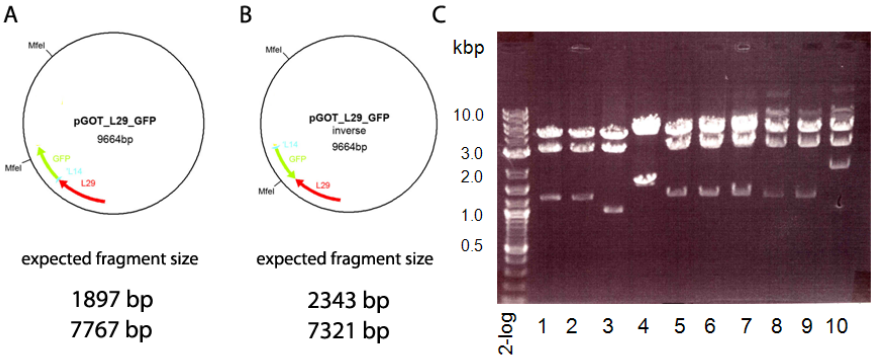

Figure 5.2.5: Control digest of pGOT_L29_GFP with MfeI. A) and B) Vector map with GFP inserted in correct or reverse orientation. The expected fragment sizes are stated. C) Agarosegel of ten digested samples

For pGOT_L1_GFP five out of ten samples (lane 1, 2, 4, 5 and 6) inserted the GFP in the correct orientation. For pGOT_L29_GFP seven out of ten samples (lane 1, 2 and 5 to 9) show the correct insert orientation.

Following the scheme described, some more macromolecules were cloned into pGOT and tagged with FbFP(Bs1). Those were: Spiralin, the most abundant membrane protein

in *Spiroplasma*, FtsZ, the molecule forming the 'Z-Ring' during bacterial cell division, ParA, which is located towards the cell poles during cell division, GroL, the most abundant chaperone and MreB, an actin-like cytoskeletal protein.
All vecors were sequenced and subsequently transformed into *S. citri* GII-3.
Unfortunately, the positive transformants that were selected upon their resistance to gentamycin never integrated the vector into their genome so that no expression of tagged proteins could be investigated. Although several approaches were undertaken, no integration event could be observed. After 15 passages the cells lost the vector and gained resistance to the antibiotics used.

6 Discussion

6.1 Visualization of Macromolecules by CET

6.1.1 Cell Morphology

The fragility of the organism, especially upon osmotic shock or mechanical forces and a challenging sample preparation were reported earlier [70]. For negative staining a special transfer method was established [29] but no such optimization was done for cryo samples. The preparation prior to and during plunge-freezing turned out to be essential for the quality of the cryo-sample. In order to concentrate the cells on the grid, a centrifugation step was performed, which did not influence the viability or morphology of the cells. This was proven by plating centrifuged and uncentrifuged cells and counting the colony forming units as well as by light microscopy. The first attempts to apply the cells in a volume of their medium and blot the sample with the standard filter paper Whatman No 1 resulted in an extraordinaryly high number of ruptured cells. We therefore resuspended the cells in a high osmolar buffer prior to blotting and tried different filter papers with changing soaking qualities. The use of buffer in combination with a very thin and slow soaking filter paper finally result in optically intact cells.
A number of investigators have studied the morphology of the *Spiroplasmas* during their growth cycle in the 1970's [10, 67, 27]. They have described alterations in the morphology of the cells in aging cultures, when changes to the pH and osmolarity occur, or when a decline in nutritients and an accumulation of degradation products takes place.
In young broth cultures the cells are of short helical shape. The helical forms increase in length during logarithmic phase. The most dominant length in the logarithmic phase is a four-turn helix, but also cells from one elementary helix up to ten turns can be observed [29]. In stationary phase, the helices may greatly elongate and then show progressive loss of helicity and motility and tend to aggregate [100]. Another modification observed in aging cultures is the formation of round 'spore-like bodies' [27]. These round forms are supposed to be formed under suboptimal environmental culture conditions. The rounded ends/ heads we observed at the starvation phase cells might be a prestage of these 'spore-like bodies'.

We observed branching cells in the tomograms of stationary and starvation phase. These branching cells emerge as thin, non-helical daughter cells laterally protruding from the main body. The appearance of these branching structures was reported in negatively stained samples [10], but no age of the culture was stated. Davies *et al.* noted that several 'filaments' may emerge from a main body [14].

6.1.2 Distribution of Ribosomes

The ribosomes that were visualized in the different growth states of *S. citri* did not show a specific distribution pattern. In all states, the proteins were distributed evenly throughout the cell in a statistical uniform way. The logarithmic phase cells show a more regular distribution of the ribosomes than expected, whereas the distribution of ribosomes in stationary and starvation phase cells fit the Poisson model. In the latter cells, there is a significant amount of unoccupied space. This might be due to DNA condensation in older cells, when the genes are not transcribed at high rates any more [15].
There have not been many localization studies for ribosomes in bacteria in different growth states, but for *B. subtilis* it was reported that there is a compartmentalization of transcription and translation components [52].
RNA polymerase was found to reside principally within the nucleoid, whereas ribosomes were localized almost exclusively outside the nucleoid, concentrating particularly towards sites of cell division. This zonal compartmentalization was shown to be independent from cell division. The results were obtained by fluorescent microscopy of GFP-labeled ribosomes (GFP fused to the S2 protein). The fluorescence was localized predominantly towards the cell poles and mid-cell future division sites in exponentially growing cells. As the cultures reached the stationary phase, the polar localization of ribosomes was less apparent and the signal was both weaker and more uniformly distributed. This was supposed to reflect the reduction in ribosome content and translational activity. Later it was shown that the specific polar localization of ribosomes in *B. subtilis* depends on active transcription [60].

The distance analysis of ribosomes to the membrane revealed a statistical uniform distribution with a peak at 24 nm for the logarithmic phase cells and at 20 nm for the stationary and starvation phase cells. The largest distances and therefore the most central orientation in the round *S. citri* cells are observed in the 4 h logarithmic phase cells. Where the other growth states have their cut-off at about 40 nm, the 4 h cells have a serious amount of ribosomes with a distance of 42 nm to the membrane. On the other

hand, these cells have a bigger size in diameter with an average of 100 nm. The cells in 72 and 120 h cultures have only a diameter of about 90 nm. But still, the cut-off at 34 nm for the stationary phase cells point to a slightly membrane oriented distribution, as there was still a margin towards the center of the cell.
Not only the distribution of the ribosomes towards the membrane, but also the direct neighbouring of the ribosomes was examined. The neighborhoods of the single ribosomes give no hint on any kind of polyribosomal structures. Blotting the relative orientations in x-y and x-z direction shows the isotropic distribution of the ribosomes in the cells and also the angular distribution spans the whole angle range. This is true for all three growth phases. One possibility of structure formation is the appearance of dimers, also called 100S ribosomes. This kind of structure can be observed in starving *E. coli* cells. An explanation for the absence of dimers in starving *S. citri* cells might be the lack of factors that are associated with ribosome modulation. The genome of *S. citri* was screened for *rmf*, *YhbH* and *YhiA* but none of these genes are present in the organism. This is not uncommon as *S. citri* is a plant pathogen that is specialized to grow in a defined environment. As a consequence, *S. citri* has undergone a reverse evolution and lost quite a part of genetic material. The genome of this organism has only a size of 1 680 kbs.
Another ribosomal pattern are polyribosomes. When translating a gene repeatedly this is not done sequentially but simultaneously. Several ribosomes read one mRNA thereby moving down the template with little space. In case of one ribosome getting stalled, the others collide and form very densely packed polyribosomal structures. The 3D structure of polysomes from *E. coli* lysate has been published lately [7].

The volume occupation by ribosomes was calculated as number of ribosomes per μm^3. For the 4 h cultures the average ribosome density was about 8500 per μm^3. The stationary phase cells had a density of about 4700 per μm^3 and the starvation phase cells of about 5000 per μm^3. With an estimated volume of 3400 nm^3 for a 70S ribosome [105] the percentage of occupation by the ribosome per cell exerpt was calculated. The volume occupied by ribosomes in the logarithmic phase is between 1.8 and 3.5 % of the total cell volume. For stationary phase this value is between 1.6 and 2.2 % for both phases.
An *E. coli* cell has a volume of 0.4 to 1.8 μm^3 [47] and the number of ribosomes per μm^3 range from 6200 to 36 000 per μm^3 during mid-log phase depending on the devision rate [16]. With these values one can calculate an occupation of cell volume by ribosomes of 5.7 % for a small cell with a devision rate of 0.6 h^{-1} or 6.8 % for a large cell with a devision rate of 2.5 h^{-1}.
This shows that *S. citri* cells have about 50 % less space occupied by ribosomes than *E.*

coli cells.

6.1.3 Ribosome Morphology

The topology of the 3D averages differed remarkably between the growth states. There are three prominent extra densities attached to the structure derived from the 4 h logarithmic phase that are not present in the structures of the 72 h and the 120 h samples. The most striking feature is the extra density on the right side of the ribosome, where the elongation factor EF-Tu is supposed to bind during active translation. Structures of ribosomes with bound EF-Tu derived from Cryo-electron microscopy show a denstity at the exact same area where we obsere the extra density [97, 37]. The second feature is located on the left side of the ribosome and forms a kind of 'handle' close to the L1 stalk. This density can not be assigned to a special known function, but the fact, that the stalks of the ribosome are more dominant in the 4 h samples hints at a significant number of actively transcribing ribosomes in the sample. It is known, that structural changes occur in the ribosome during translation, especially in the L1-stalk and the L7/L12-stalk region [96, 53].
In comparison to the *E. coli* 70S ribosome, the *S. citri* ribosome looks more massive with a slightly larger diameter in x-y direction. The *E. coli* ribosome might not be the best reference to compare the *S. citri* ribosome with, as the phylogenetic distance between the two organisms is large. On the other hand there is no ribosomal structure available that is closer related.
The fact, that differences in morphology could be detected in the samples from the same cells but in different growth states, demonstrates the power of cryo-electron tomography. In contrast to structures from uniform, isolated samples, the structures derived from intact cells with our method, show a ribosome caught in an active state of transcription for the 4 h samples and apparently unengaged ribosomes for the other states. This does not mean that there is no transcription taking place in these cells, but the amount of active ribosomes is too small for the features to arise in the 3D average of all particles.

6.1.4 Template Matching

Tomograms are a valuable source of information as they show a snapshot of local molecular interactions. To date, the resolution of cryo-tomograms is about 4 nm which is sufficient to detect quaternary structures inside the cell. The template matching technique used for this purpose is a powerful tool but is affected with several challenges.
Due to the electron sensitivity of the vitrified samples and the resulting beam damage,

tomograms are recorded at a very low electron dose, thus resulting in a low signal to noise ratio (SNR). Moreover, owing to the missing wedge effect the tomograms are distorted what results in an anisotropic resolution.
Apart from the technical aspects, the cytoplasm of cells is densely packed and proteins are not found in an isolated environment but are observed to interact with their neighbors [34]. This high protein concentration, known as molecular crowding, also has a negative impact on the contrast of the tomograms. Apart from some very dominant structures like membranes or filaments it is nearly impossible to identify macromolecular complexes manually [62]. The template matching was developed and shown to work in phantom cells (liposomes filled with a defined set of proteins) where it was shown that it is possible to detect and distinguish between two different but topologically similar macromolecules, the 20S Proteasome and the Thermosome [4, 24]. This technique was then extended to intact procaryotic cells where 70S ribosomes were detected in *Spiroplasma melliferum* cells and their cellular distribution was visualized as a protein atlas [66].
But still, more than 50 % of the particles detected by template matching are false positives, that have to be eliminated manually. However, this manual selection is subjective, not reproducible and, due to the huge amount of data, very time consuming.

6.1.5 3D Averaging

The selected particles were reconstructed in subtomograms in full resolution and aligned against a first average of all particles that had only a rough orientation. We abandoned the alignment against a downsampled 70S ribosome reference to minimize a possible template bias.
Particle classification was performed using constraint-correlation based on a principal component analysis algorithm (PCA).

A second approach is a reference-free alignment and classification [81]. As initial model for the iterative maximum-likelihood (ML) refinement algorithm, a sphere, an average of all particles with random orientation resulting in a featureless blob or simply noise can be used. The aim of the algorithm is to find the most likely set of parameters to construct a statistical model describing structurally heterogenous data. The main difference from conventional projection-matching protocols is that the discrete assignments of projection orientation and class membership are replaced by probability-weighted integrations over all possible assignments.

To verify our results, the data set of the 4 h particles were analyzed with this ML method (kindly done by Sjors Scheres, Centro National de Biotecnologia, CSIC, Cantoblanco, Madrid, Spain and Michael Stölken, MPI of Biochemistry). The reference-free alignment resulted in a 3D average that clearly depicted a 70S ribosome. The extra-density at the elongation factor binding site was also approved. In general the obtained structure had a lower resolution and showed less details but the core information matched with our results from constraint correlation.

6.2 Genetic Tools for *S. citri*

6.2.1 OriC Plasmids in *S. citri*

The development of OriC plasmides used in *S. citri* started in 1994 with the sequencing of a 5.6 kbps DNA fragment containing the OriC region. This fragment was shown to cover the genes for the replication initiator protein dnaA, the beta-subunit of the DNA polymerase III dnaN and the DNA gyrase subunits A and B (gyrA and gyrB) [103]. Only one year later, Renaudin *et al.* identified the 2 kbps OriC fragment as autonomously replicating sequence and proved the mandatory provision of the dnaA boxes for this purpose. They generated the first integrative vector that could be shuttled between *S. citri* and *E. coli* with this OriC sequence, a ColE1-derived *E. coli* replicon and the TetM sequence for antibiotic resistence. Upon passaging of the *S. citri* transformants, the plasmid integrated into the spiroplasmal host chromosome by recombination at the replication origin. The integration process led to duplication of the oriC sequences.
A vector without the *E. coli* replicon could be stably maintained as a free extrachromosomal element. This vector was used to express the G fragment of the cytadhesin P1 gene of *Mycoplasma pneumoniae* and the spiralin gene of *Spiroplasma phoeniceum* in *S. citri* [73].
This vector was the basis of the pSD4 vector which we wanted to use for the expression of foreign genes in *S. citri* except that it contained a fibril protein promoter instead of the dnaN promotor region.
Although the expression of genes from related species was shown to be successful, so far no expression of foreign genes has been done. The pSD4 vector, that was kindly provided by Sybille Duret and Joel Renaudin (INRA, Bordeaux) has never been used for protein expression but was a precursor when developing an integration vector for gene disruption.

The pSD4 vector contained the promotor for the dnaN gene but this promotor turned out to be unable to drive foreign gene expression in *S. citri*. The *S. citri* ribosomal

binding site was enclosed to the gene of interest by PCR. The ribosome binding site of *S. citri* needs a higher consensus to the 16S of the ribosome than usual. There, the TATA box is a TATAATA box. As hypothetical reason for the absence of expressed protein could also have been a lack of translation, the ribosome binding site was altered in a way that differing distances between Shine-Dalgarno sequence and start codon were used. Our results show that this distance is not strictly predefined in *S. citri* as all constructs under the control of the spiralin promotor are suited to drive protein expression, independently of the length of that sequence.
One main problem still remains when working with transgenic *S. citri*: They tend to lose the transformed vector. When using the pSP vector, the cells dump the vector after approximately four to six passages. However, the cells gain spontaneous resistance to the antibiotic so the culture still grows. A regular screen on the presence of the vector is therefore relevant.
The improved vector pSpi contained a shorter OriC fragment, thereby reducing the chances of intergartion into the genome. In general, this integration is not unfavorable, but this would result in stable mutants. However, it can not be excluded that integration of the vector is the first step for the cells to gain resistance before excising the unwanted part of the vector. Nevertehless, the pSpi vector had only a slightly increased duration of stay. Raising the antibiotic concentrations from 2 to 15 μg/ml during passaging prolonged the delay of the vector inside the cells.
This recurrent loss of the vector was the reason that no further experiments like activity assays or electron tomography could be performed with the transgenic cells.

6.2.2 GFP in *S. citri*

No fluorescent protein has been expressed in *S. citri* before. Duret *et al.* constructed an integration vector with GFP fused to the spiralin gene in order to knock out the endogenous spiralin and replace it in the cell by GFP-tagged Spiralin [20]. The experiment resulted in a Spiralin knock-out phenotype. No fluorescence could be observed because of a mutation of glycerin to cystein at position 33 of the GFP.
Our results show that GFP is in general not suited for fluorescence experiments in *S. citri* due to the lack of oxygen. The fact, that GFP needs molecular oxygen to form a functional chromophore was first shown by Heim *et al.* [40]. They demonstrated that GFP expressed in anaerobically grown bacteria looked identical on SDS gels but was nonfluorescent. When oxygen was re-admitted, the fluorescence was restored. Inouye *et al.* [42] came to the same conclusion.
The molecular mechanisms underlying these observations was described later: The chro-

mophore is a p-hydroxybenzylideneimidazolinone formed from residues 65-67, which are Ser-Tyr-Gly in the native protein. First, GFP folds into a nearly native conformation, then the imidazolinone is formed by nucleophilic attack of the amide of Gly67 on the carbonyl of residue 65, followed by dehydration. Finally, molecular oxygen dehydrogenates the $\alpha - \beta-$ bond of residue 66 to put its aromatic group into conjugation with the imidazolinone [93].
The fact that molecular oxygen is needed for fluorescence is undisputed but the essential amount of oxygen is not stated.
As an alternative, we used a flavin mononucleotide-based fluorescent protein (FbFP) described by Drepper *et al.* [17]. They started with blue light photoreceptors from *Bacillus subtilis* and *Pseudomonas putida* that contain light-oxygen-voltage sensing domains and engineered flavin mononucleotide - based fluorescent proteins that can be used as fluorescent reporters in both aerobic and anaerobic biological systems.
There are now three variants of FbFP available: Bs1, Bs2 (both from *Bacillus subtilis*) and Pp1 (from *Pseudomonas putida*). We cloned vectors with all three variants but only the Bs1 was transformed and expressed in *S. citri*. This was due to the fact that Bs1 has the best fluorescence yield.

6.2.3 Fluorescence Microscopy of *S. citri*

We performed fluorescence microscopy with *S. citri* on a Leica Confocal microscope. This had the advantage that light and fluorescent channel could be recorded simultaneously. Light microscopy with *S. citri* bears several challenges: The main disadvantages are caused simply by the size of the organism. *S. citri* has an average diameter of 100 nm and therefore gives very little contrast in a phase contrast microscope. It is therefore a task to find the correct focus plane. The maximum magnification of the objective lens used is 63-fold. Digital post-magnification is possible but does not contribute to resolution. Concerning this point, other microscope types like normal DIC or TIRF would be advantageous but motility of the cells demands a multi-channel acquisition, which is usually only equipped at a confocal microscope.
The cells are, as mentioned above, very motile and move through the medium during image acquisition. The motility can be stemmed by using agar pads but this makes the adjustment of the focus plane nearly impossible.
First, we applied the cells to the object slide in their medium, but the medium had a high salt concentration and other factors that caused an unfavorable high background when using the fluorescent channel. That is why we washed the cells in HSO buffer prior to applying them on the slide. Due to the centrifugation step involved, the cells

tended to form aggregates, which could not be resuspended completely. This means that no single cell microscopy could be performed. However, the aggregates, which had an average size of 4 - 10 cells, were large enough to be detected even on agar pads.
The resulting fluorescence signal was still very weak. This may be due to several reasons: One is the thickness of the cells. With an average diameter of 100 nm only few FbFP molecules can contribute to the fluorescence signal in the Z-plane.
Another reason could be that the expression is too weak in general and only little FbFP is present in the cell. This could be verified by a quantitative PCR reaction.
But the pH is also a crucial factor for the function of any fluorescent protein. GFP is even used as intracellular pH sensor [65, 3]. *Spiroplasma* produces lactate during cell growth and the pH of the medium drops from 7.8 at the beginning of a passage to 5.6 after three days. The intracellular pH of *S. citri* has not been measured so far.
Either way, to use FbFP in *S. citri* routinely there has to be done a lot of optimization work. The results shown in this work are only first steps towards fluorescent microscopy in *Spiroplasma*.

6.2.4 Induced Gene Expression in *S. citri*

One chance to overcome the problem of vector loss is to engineer vectors for inducible gene expression. In theory, the gene is only read out for a short and defined period of time. For the design of follow-up experiments it would be advantageous to know exactly when the protein of interest was present in the cell. An inactive vector without any impact on the cell physiology is also expected to be kept inside the cell more readily.
When looking for an inducible promotor for *S. citri*, we aimed at an endogenous promotor. Mollicutes are rather divergent from other bacteria and an endogenous sequence was expected to be more promising than using a promotor from another organism.
Upon transposon mutation Gaurivaud *et al.* [31] found and characterized the fructose operon of *S. citri*. The promotor region was identified by primer extention [30] and the first gene in the operon, FruR was reported to act as enhancer of this promotor. We cloned two inducible expression vectors, one containing the promotor region and FruR, and one containing only the promotor.
New fructose-free medium had to be developed, as the PPLO serum fraction, the basis of all media stated in papers related to the fructose operon [31, 30, 1, 72] is no longer produced. We replaced FBS, the main source of fructose, in the standard medium SP4 by supplementing with BSA and synthetic cholesterole. Cell growth was monitored by recording growth curves based on dropping pH.
Although cell growth of healthy cultures in the supplemented medium SP^- was compa-

rable to the control, transformation efficiency was lower than with SP4 medium. Only about 20% of the picked colonies contained the vector. Unfortunately, the cells grew very slowly and lost the vector after three passages so that no further experiments could be performed.
Recently, Breton *et al.* [8] accounted the successful expression of a protein under the control of the tetracycline-inducible promoter Pxyl/tetO(2) from *Bacillus subtilis* in two mollicutes, the plant pathogen *Spiroplasma citri* and the animal pathogen *Mycoplasma agalactiae*. They were able to rescue a Spiralin-deficient mutant of *S. citri* [20] using this system.

6.2.5 Tagging of endogenous Proteins

Fusion of a fluorescent tag to endogenous proteins has been done in numerous organisms. GFP is routinely used to do localization studies in eukarotes, archea and bacteria. In *S. citri* a disruption vector was established that was first used to create knock-outs of certain genes. But the concept of the vector also allows to tag proteins. The endogenous DNA sequence is replaced either by an unfunctional gene variant or by a tagged one. The laboratory at INRA in Bordeaux did a lot of work on this vector.
As *S. citri* lacks RecA, the frequency of recombination is low [59]. Therefore the vector has to be self-replicating to stay present in the cell until one of these rare recombination events takes place. Lartigue *et al.* determined the shortest functional OriC sequence and designed a vector with this short variant [49]. This prevents recombination at the OriC site instead at the gene of interest.
This vector was further improved and shown to successfully inactivate the *crr* gene encoding the IIA component of the glucose phosphotransferase system (PTS) permease and the arginine deiminase (arcA) [19].
With this vector described in [19] we wanted to tag ribosomal proteins first with GFP, later with FbFP. The constructs were all successfully cloned and sequenced and transformation into *S. citri* was effective. But none of the samples showed a recombination of the vector into the genome and after 15 passages the cells lost the vector. If the recombination does not take place during the first 12 passages, it is very unlikely to succeed (S. Duret, personal communication). We performed the transformation repeatedly but no vector integration took place. However, the designed vectors could be easily used to create knock-downs of Spiralin, GroEL, MreB, ParA and FtsZ.

Abbreviations

CC	Correlation Coefficient
CCR	Combined Polymerase Chain Reaction
CET	Cryo-electron Tomography
CTF	Contrast Transfer Function
EM	Electron Microscopy
FEG	Field Emission Gun
GFP	Green Fluorescent Protein
IPTG	Isopropyl-β-D-thiogalactopyranoside
LCF	Local Correlation Function
mRNA	messenger RNA
PCA	Principal Component Analysis
PCR	Polymerase Chain Reaction
PSF	Point Spread Function
rRNA	ribosomal RNA
SDS	Sodium Dodecylsulfate
SNR	Signal-to Noise Ratio
TAP	*Thermoplasma acidophilum* Proteasome
TEM	Transmission Electron Microscope
TPPII	Tripeptidyl Peptidase II
tRNA	transfer RNA

Acknowledgments

I would like to express my deep gratitude and high regard to Professor Dr. Wolfgang Baumeister, head of the Department of Molecular Structural Biology, for giving me the opportunity to realize my PhD thesis in his department, for his generous support and supervision.

I owe my gratitude to Dr. Julio Ortiz for his supervision and encouragement for his support especially concerning data processing and 3D imaging and for critically proof-reading this thesis.

My sincere appreciation to Professor Dr. Joel Renaudin and Dr. Sybille Duret for providing the vectors for genetic manipulation of *S. citri* on which this work was based on and for introducing me to the cultivation and handling of the cells.

I am indebted to my many of my colleagues who supported me: Harald Engelhard, Jürgen Peters and Stephan Nickell for helpful suggestions and proof-reading this thesis, Peter Zwickel, Susanne Witt and Oana Mihalache for encouraging me in the lab.
Andreas Korinek for providing the comfortable tomography software and spending numerous days at the microscope with me for optimizing it, Michael Stölken for the Maximum-Likelyhood calculations and Matthias Eibauer for the CTF correction of the tomographic data.
Thanks to Günter Pfeiffer and Jürgen Plitzko for their support at the microscopes.
I would like to thank all my colleagues in the department who contributed to that pleasant atmosphere and giving me a helping hand whenever it was necessary: Amy Schönegge, Manuela Gruska, Inga Wolf, Andrew Leis, Lars Andrees, Shoh Asano and many others.

Special thanks to Roland Knispel for fruitful scientific discussions, motivating me when I was close to becoming a sheep farmer in New Zealand and for relentlessly moving my furniture.

Elke Glasmacher and Imke Helling for their constant support including scientific discussions, highly intellectual TV evenings and repeatedly rescuing me from sure insanity. Elke also for proofreading this thesis.

I also would like to thank the members of the tuesday and thursday volleyball team for providing a compensation to all the intellectual work and for giving me their friendship and hours of fun.

Zu guter Letzt möchte ich mich bei meiner Familie bedanken. Allen voran meinen Eltern die mich mit unermüdlicher Ausdauer begleitet haben und die meine Ausbildung in jeder erdenklichen Hinsicht unterstützt haben. Ohne euch wäre diese Arbeit nicht möglich gewesen.
Danke auch an meine Geschwister, Cornelia, Markus und Uli, für euer konstantes Interesse und eure Unterstützung. Besonders Markus für das wiederholte Schleppen meiner Möbel.
Und Danke an meinen Freund Claude, für dein Verständnis und dass du mir mein Lachen wieder gegeben hast.

Danke an Alle!

Bibliography

[1] Aurélie André, Mickaël Maucourt, Annick Moing, Dominique Rolin, and Joël Renaudin. Sugar import and phytopathogenicity of spiroplasma citri: glucose and fructose play distinct roles. *Mol Plant Microbe Interact*, 18(1):33–42, Jan 2005.

[2] N. Ban, P. Nissen, J. Hansen, P. B. Moore, and T. A. Steitz. The complete atomic structure of the large ribosomal subunit at 2.4 a resolution. *Science*, 289(5481):905–920, Aug 2000.

[3] Ranieri Bizzarri, Michela Serresi, Stefano Luin, and Fabio Beltram. Green fluorescent protein based ph indicators for in vivo use: a review. *Anal Bioanal Chem*, 393(4):1107–1122, Feb 2009.

[4] J. Bohm, A. S. Frangakis, R. Hegerl, S. Nickell, D. Typke, and W. Baumeister. Toward detecting and identifying macromolecules in a cellular context: template matching applied to electron tomograms. *Proc Natl Acad Sci U S A*, 97(26):14245–14250, Dec 2000.

[5] J. M. Bové. Molecular features of mollicutes. *Clin Infect Dis*, 17 Suppl 1:S10–S31, Aug 1993.

[6] Joseph M Bové, Joël Renaudin, Colette Saillard, Xavier Foissac, and Monique Garnier. Spiroplasma citri, a plant pathogenic molligute: relationships with its two hosts, the plant and the leafhopper vector. *Annu Rev Phytopathol*, 41:483–500, 2003.

[7] Florian Brandt, Stephanie A Etchells, Julio O Ortiz, Adrian H Elcock, F. Ulrich Hartl, and Wolfgang Baumeister. The native 3d organization of bacterial polysomes. *Cell*, 136(2):261–271, Jan 2009.

[8] Marc Breton, Evelyne Sagné, Sybille Duret, Laure Béven, Christine Citti, and Joël Renaudin. First report of a tetracycline-inducible gene expression system for mollicutes. *Microbiology*, 156(Pt 1):198–205, Jan 2010.

[9] J. H. Cate, M. M. Yusupov, G. Z. Yusupova, T. N. Earnest, and H. F. Noller. X-ray crystal structures of 70s ribosome functional complexes. *Science*, 285(5436):2095–2104, Sep 1999.

[10] R. M. Cole, J. G. Tully, T. J. Popkin, and J. M. Bové. Morphology, ultrastructure, and bacteriophage infection of the helical mycoplasma-like organism (spiroplasma citri gen. nov., sp. nov.) cultured from "stubborn" disease of citrus. *J Bacteriol*, 115(1):367–384, Jul 1973.

[11] V. E. Cosslett. Energy loss and chromatic abberation in electron microscopy. *Zeitschrift für angewandte Physik*, 27:138–141, 1969.

[12] R. A. Crowther, L. A. Amos, J. T. Finch, D. J. De Rosier, and A. Klug. Three dimensional reconstructions of spherical viruses by fourier synthesis from electron micrographs. *Nature*, 226(5244):421–425, May 1970.

[13] M. J. Daniels and J. M. Longland. Chemotactic behavior of spiroplasmas. *Current Microbiology*, 10:191–194, 1984.

[14] R. E. Davies, J. F. Worley, R. F. Whitcomb, T. Ishijima, and R. L. Steere. Helical filaments produced by a mycoplasma-like organism associated with corn stunt disease. *Science*, 176:521–523, 1972.

[15] Renko de Vries. Dna condensation in bacteria: Interplay between macromolecular crowding and nucleoid proteins. *Biochimie*, Jul 2010.

[16] P. P. Dennis and H. Bremer. Macromolecular composition during steady-state growth of escherichia coli b-r. *J Bacteriol*, 119(1):270–281, Jul 1974.

[17] Thomas Drepper, Thorsten Eggert, Franco Circolone, Achim Heck, Ulrich Krauss, Jan-Karl Guterl, Marion Wendorff, Aba Losi, Wolfgang Gärtner, and Karl-Erich Jaeger. Reporter proteins for in vivo fluorescence without oxygen. *Nat Biotechnol*, 25(4):443–445, Apr 2007.

[18] S. Duret, J. L. Danet, M. Garnier, and J. Renaudin. Gene disruption through homologous recombination in spiroplasma citri: an scm1-disrupted motility mutant is pathogenic. *J Bacteriol*, 181(24):7449–7456, Dec 1999.

[19] Sybille Duret, Aurélie André, and Joël Renaudin. Specific gene targeting in spiroplasma citri: improved vectors and production of unmarked mutations using site-specific recombination. *Microbiology*, 151(Pt 8):2793–2803, Aug 2005.

[20] Sybille Duret, Nathalie Berho, Jean-Luc Danet, Monique Garnier, and Joël Renaudin. Spiralin is not essential for helicity, motility, or pathogenicity but is required for efficient transmission of spiroplasma citri by its leafhopper vector circulifer haematoceps. *Appl Environ Microbiol*, 69(10):6225–6234, Oct 2003.

[21] B. Feja and U. Aebi. Determination of the inelastic mean free path of electrons in vitrified ice layers for on-line thickness measurements by zero-loss imaging. *J Microsc*, 193(1):15–19, Jan 1999.

[22] J. Fletcher, A. Wayadande, U. Melcher, and F. Ye. The phytopathogenic mollicute-insect vector interface: a closer look. *Phytopathology*, 88(12):1351–1358, Dec 1998.

[23] X. Foissac, C. Saillard, and J. M. Bové. Random insertion of transposon tn4001 in the genome of spiroplasma citri strain gii3. *Plasmid*, 37(1):80–86, 1997.

[24] Achilleas S Frangakis, Jochen Böhm, Friedrich Förster, Stephan Nickell, Daniela Nicastro, Dieter Typke, Reiner Hegerl, and Wolfgang Baumeister. Identification of macromolecular complexes in cryoelectron tomograms of phantom cells. *Proc Natl Acad Sci U S A*, 99(22):14153–14158, Oct 2002.

[25] J. Frank, J. Zhu, P. Penczek, Y. Li, S. Srivastava, A. Verschoor, M. Radermacher, R. Grassucci, R. K. Lata, and R. K. Agrawal. A model of protein synthesis based on cryo-electron microscopy of the e. coli ribosome. *Nature*, 376(6539):441–444, Aug 1995.

[26] Friedrich Förster, Ohad Medalia, Nathan Zauberman, Wolfgang Baumeister, and Deborah Fass. Retrovirus envelope protein complex structure in situ studied by cryo-electron tomography. *Proc Natl Acad Sci U S A*, 102(13):4729–4734, Mar 2005.

[27] A. A. Fudl-Allah and E. C. Calavan. Cellular morphology and reproduction of the mycoplasma-like organism associated with citrus stubborn disease. *Phytopathology*, 64:1309–1313, 1974.

[28] I. S. Gabashvili, S. T. Gregory, M. Valle, R. Grassucci, M. Worbs, M. C. Wahl, A. E. Dahlberg, and J. Frank. The polypeptide tunnel system in the ribosome and its gating in erythromycin resistance mutants of l4 and l22. *Mol Cell*, 8(1):181–188, Jul 2001.

[29] M. Garnier, M. Clerc, and J. M. Bove. Growth and division of spiroplasmas: morphology of spiroplasma citri during growth in liquid medium. *J Bacteriol*, 147(2):642–652, Aug 1981.

[30] P. Gaurivaud, F. Laigret, M. Garnier, and J. M. Bové. Characterization of frur as a putative activator of the fructose operon of spiroplasma citri. *FEMS Microbiol Lett*, 198(1):73–78, Apr 2001.

[31] P. Gaurivaud, F. Laigret, E. Verdin, M. Garnier, and J. M. Bové. Fructose operon mutants of spiroplasma citri. *Microbiology*, 146 (Pt 9):2229–2236, Sep 2000.

[32] R. Grimm, A. J. Koster, U. Ziese, D. Typke, and W. Baumeister. Zero-loss energy filtering under low-dose conditions using a post-column energy filter. *Journal of Microscopy*, 183:60–68, 1996.

[33] R. Grimm, D. Typke, M. Bärmann, and W. Baumeister. Determination of the inelastic mean free path in ice by examination of tilted vesicles and automated most probable loss imaging. *Ultramicroscopy*, 63(3-4):169–179, Jul 1996.

[34] Kay Grünewald, Ohad Medalia, Ariane Gross, Alasdair C Steven, and Wolfgang Baumeister. Prospects of electron cryotomography to visualize macromolecular complexes inside cellular compartments: implications of crowding. *Biophys Chem*, 100(1-3):577–591, 2003.

[35] A. Grziwa, W. Baumeister, B. Dahlmann, and F. Kopp. Localization of subunits in proteasomes from thermoplasma acidophilum by immunoelectron microscopy. *FEBS Lett*, 290(1-2):186–190, Sep 1991.

[36] R. Guckenberger. Determination of a common origin in the micrographs of tilt series in 3-dimensional electron microscopy. *Ultramicroscopy*, 9(1-2):167–173, 1982.

[37] Peter W Haebel, Sascha Gutmann, and Nenad Ban. Dial tm for rescue: tmrna engages ribosomes stalled on defective mrnas. *Curr Opin Struct Biol*, 14(1):58–65, Feb 2004.

[38] G. Harauz and M. van Heel. Exact filters for general geometry 3-dimensional reconstruction. *Optik*, 73(4):146–156, 1986.

[39] J. Harms, F. Schluenzen, R. Zarivach, A. Bashan, S. Gat, I. Agmon, H. Bartels, F. Franceschi, and A. Yonath. High resolution structure of the large ribosomal subunit from a mesophilic eubacterium. *Cell*, 107(5):679–688, Nov 2001.

[40] R. Heim, D. C. Prasher, and R. Y. Tsien. Wavelength mutations and posttranslational autoxidation of green fluorescent protein. *Proc Natl Acad Sci U S A*, 91(26):12501–12504, Dec 1994.

[41] W. Hoppe and R. Hegerl. *Topics in Current Physics Computer Processing of Electron Microscopic Images*, chapter Three-dimensional structure determination by electron microscopy (non-periodic specimens). Springer Verlag, 1986.

[42] S. Inouye and F. I. Tsuji. Evidence for redox forms of the aequorea green fluorescent protein. *FEBS Lett*, 351(2):211–214, Sep 1994.

[43] C. Jacob, F. Nouzières, S. Duret, J. M. Bové, and J. Renaudin. Isolation, characterization, and complementation of a motility mutant of spiroplasma citri. *J Bacteriol*, 179(15):4802–4810, Aug 1997.

[44] Simon Jenni and Nenad Ban. The chemistry of protein synthesis and voyage through the ribosomal tunnel. *Curr Opin Struct Biol*, 13(2):212–219, Apr 2003.

[45] S. Knapp, H. Uhring, and F. Salamini. *Genetic transformation of diploid Solanum tuberosum by direct gene transfer and mediated by Agrobacterium tumefaciens.*, chapter Progress in Plant Protoplast Research, pages 355–356. Kluwer Academic Publishers, Dordrecht, 1988.

[46] N. Knipfer and T. E. Shrader. Inactivation of the 20s proteasome in mycobacterium smegmatis. *Mol Microbiol*, 25(2):375–383, Jul 1997.

[47] H. E. Kubitschek and J. A. Friske. Determination of bacterial cell volume with the coulter counter. *J Bacteriol*, 168(3):1466–1467, Dec 1986.

[48] S. R. Kushner. *An improved method for transformation of Escherichia coll with ColEl-derived plasmids.*, pages 17–23. Elsevier, 1978.

[49] Carole Lartigue, Sybille Duret, Monique Garnier, and Joël Renaudin. New plasmid vectors for specific gene targeting in spiroplasma citri. *Plasmid*, 48(2):149–159, Sep 2002.

[50] K. R. Lata, R. K. Agrawal, P. Penczek, R. Grassucci, J. Zhu, and J. Frank. Three-dimensional reconstruction of the escherichia coli 30 s ribosomal subunit in ice. *J Mol Biol*, 262(1):43–52, Sep 1996.

[51] Andrew Leis, Beate Rockel, Lars Andrees, and Wolfgang Baumeister. Visualizing cells at the nanoscale. *Trends Biochem Sci*, 34(2):60–70, Feb 2009.

[52] P. J. Lewis, S. D. Thaker, and J. Errington. Compartmentalization of transcription and translation in bacillus subtilis. *EMBO J*, 19(4):710–718, Feb 2000.

[53] A Liljas. *Structural Aspects of Protein Synthesis*. Singapore: World Scientific Publishing Co. Pte. Ltd., 2004.

[54] Y. Liu, P. A. Penczek, B. F. McEwen, and J. Frank. A marker-free alignment method for electron tomography. *Ultramicroscopy*, 58(3-4):393–402, Jun 1995.

[55] Jianli Lu and Carol Deutsch. Folding zones inside the ribosomal exit tunnel. *Nat Struct Mol Biol*, 12(12):1123–1129, Dec 2005.

[56] Vladan Lucic, Friedrich Förster, and Wolfgang Baumeister. Structural studies by electron tomography: from cells to molecules. *Annu Rev Biochem*, 74:833–865, 2005.

[57] J. Löwe, D. Stock, B. Jap, P. Zwickl, W. Baumeister, and R. Huber. Crystal structure of the 20s proteasome from the archaeon t. acidophilum at 3.4 a resolution. *Science*, 268(5210):533–539, Apr 1995.

[58] M. Mandel and A. Higa. Calcium-dependent bacteriophage dna infection. *J. Mol. Biol.*, 53:109–118, 1970.

[59] A. Marais, J. M. Bove, and J. Renaudin. Characterization of the reca gene regions of spiroplasma citri and spiroplasma melliferum. *J Bacteriol*, 178(23):7003–7009, Dec 1996.

[60] J. Mascarenhas, M. H. Weber, and P. L. Graumann. Specific polar localization of ribosomes in bacillus subtilis depends on active transcription. *EMBO Rep*, 2(8):685–689, Aug 2001.

[61] M. Mathews, N. Sonenberg, and J. W. B. Hershey. *Translational Control of Gene Expression*. Cold Spring Harbour Laboratory Press, 2000.

[62] Ohad Medalia, Igor Weber, Achilleas S Frangakis, Daniela Nicastro, Gunther Gerisch, and Wolfgang Baumeister. Macromolecular architecture in eukaryotic cells visualized by cryoelectron tomography. *Science*, 298(5596):1209–1213, Nov 2002.

[63] Stephan Nickell, Christine Kofler, Andrew P Leis, and Wolfgang Baumeister. A visual approach to proteomics. *Nat Rev Mol Cell Biol*, 7(3):225–230, Mar 2006.

[64] P. Nissen, J. Hansen, N. Ban, P. B. Moore, and T. A. Steitz. The structural basis of ribosome activity in peptide bond synthesis. *Science*, 289(5481):920–930, Aug 2000.

[65] Rick Orij, Jarne Postmus, Alex Ter Beek, Stanley Brul, and Gertien J Smits. In vivo measurement of cytosolic and mitochondrial ph using a ph-sensitive gfp derivative in saccharomyces cerevisiae reveals a relation between intracellular ph and growth. *Microbiology*, 155(Pt 1):268–278, Jan 2009.

[66] Julio O Ortiz, Friedrich Förster, Julia Kürner, Alexandros A Linaroudis, and Wolfgang Baumeister. Mapping 70s ribosomes in intact cells by cryoelectron tomography and pattern recognition. *J Struct Biol*, 156(2):334–341, Nov 2006.

[67] K. R. Patel, K. J. Mayberry-Carson, and P. F. Smith. Effect of external environmental factors on the morphology of spiroplasma citri. *J Bacteriol*, 133(2):925–931, Feb 1978.

[68] G. Pühler, S. Weinkauf, L. Bachmann, S. Müller, A. Engel, R. Hegerl, and W. Baumeister. Subunit stoichiometry and three-dimensional arrangement in proteasomes from thermoplasma acidophilum. *EMBO J*, 11(4):1607–1616, Apr 1992.

[69] M. Radermacher, T. Wagenknecht, A. Verschoor, and J. Frank. A new 3-d reconstruction scheme applied to the 50s ribosomal subunit of e. coli. *J Microsc*, 141(Pt 1):RP1–RP2, Jan 1986.

[70] S. Razin, M. Hasin, Z. Ne'eman, and S. Rottem. Isolation, chemical composition, and ultrastructural features of the cell membrane of the mycoplasma-like organism *Spiroplasma citr. Journal of Bacteriology*, 116:1421–1435, 1973.

[71] J. Renaudin. *Molecular Biology and Pathogenicity of Mycoplasmas*, chapter Extrachromosomal elements and gene transfer, pages 347–370. Kluwer Academic/ Plenum Publishers, 2002.

[72] J. Renaudin. Sugar metabolism and pathogenicity of spiroplasma citri. *Journal of Plant Pathology*, 88:129–139, 2006.

[73] J. Renaudin, A. Marais, E. Verdin, S. Duret, X. Foissac, F. Laigret, and J. M. Bové. Integrative and free spiroplasma citri oric plasmids: expression of the spiroplasma phoeniceum spiralin in spiroplasma citri. *J Bacteriol*, 177(10):2870–2877, May 1995.

[74] Beate Rockel, Jürgen Peters, Shirley A Müller, Gönül Seyit, Philippe Ringler, Reiner Hegerl, Robert M Glaeser, and Wolfgang Baumeister. Molecular architecture and assembly mechanism of drosophila tripeptidyl peptidase ii. *Proc Natl Acad Sci U S A*, 102(29):10135–10140, Jul 2005.

[75] A. M. Roseman. Docking structures of domains into maps from cryo-electron microscopy using local correlation. *Acta Crystallogr D Biol Crystallogr*, 56(Pt 10):1332–1340, Oct 2000.

[76] E. Ruska. The development of the electronmicroscope and electron microscopy. nobel lecture. *Rev. Modern Phys.*, 59(3):121–164, 1987.

[77] P. Saglio, D. Laflèche, C. Bonissol, and J. M. Bové. Culture in vitro des mycoplasmes associés au stubborn des agrumes et leur observation au microscope èlectronique. *C R Acad Sci Paris*, 272:1387–1390, 1971.

[78] P. Saglio, M. Lhospital, D. Laflèche, G. Dupont, J. M. Bové, J. G. Tully, and E. A. Freundt. Spiroplasma citri gen. and sp. n.: a mycoplasma-like organism associated with 'stubborn' disease of citrus. *Int J Syst Bacteriol*, 23:191–204, 1973.

[79] Andrej Sali, Robert Glaeser, Thomas Earnest, and Wolfgang Baumeister. From words to literature in structural proteomics. *Nature*, 422(6928):216–225, Mar 2003.

[80] B.E.H. Saxberg and W.O. Saxton. Quantum noise in 2d projections and 3d reconstructions. *Ultramicroscopy*, 6:127–138, 1981.

[81] Sjors H W Scheres, Haixiao Gao, Mikel Valle, Gabor T Herman, Paul P B Eggermont, Joachim Frank, and Jose-Maria Carazo. Disentangling conformational states of macromolecules in 3d-em through likelihood optimization. *Nat Methods*, 4(1):27–29, Jan 2007.

[82] O. Scherzer. The theroretical resolution limit of the electron microscope. *J. Applied Physics*, 20:20–29, 1949.

[83] I. N. Shatsky, A. V. Bakin, A. A. Bogdanov, and V. D. Vasiliev. How does the mrna pass through the ribosome? *Biochimie*, 73(7-8):937–945, 1991.

[84] J. Shine and L. Dalgarno. The 3'-terminal sequence of escherichia coli 16s ribosomal rna: complementarity to nonsense triplets and ribosome binding sites. *Proc Natl Acad Sci U S A*, 71(4):1342–1346, Apr 1974.

[85] R. J. Siezen and J. A. Leunissen. Subtilases: the superfamily of subtilisin-like serine proteases. *Protein Sci*, 6(3):501–523, Mar 1997.

[86] C. M. Spahn and C. D. Prescott. Throwing a spanner in the works: antibiotics and the translation apparatus. *J Mol Med*, 74(8):423–439, Aug 1996.

[87] Alex Stewart and Nikolaus Grigorieff. Noise bias in the refinement of structures derived from single particles. *Ultramicroscopy*, 102(1):67–84, Dec 2004.

[88] K. Tanaka, K. Ii, A. Ichihara, L. Waxman, and A. L. Goldberg. A high molecular weight protease in the cytosol of rat liver. i. purification, enzymological properties, and tissue distribution. *J Biol Chem*, 261(32):15197–15203, Nov 1986.

[89] K. A. Taylor, J. Tang, Y. Cheng, and H. Winkler. The use of electron tomography for structural analysis of disordered protein arrays. *J Struct Biol*, 120(3):372–386, Dec 1997.

[90] A. Tocilj, F. Schlünzen, D. Janell, M. Glühmann, H. A. Hansen, J. Harms, A. Bashan, H. Bartels, I. Agmon, F. Franceschi, and A. Yonath. The small ribosomal subunit from thermus thermophilus at 4.5 a resolution: pattern fittings and the identification of a functional site. *Proc Natl Acad Sci U S A*, 96(25):14252–14257, Dec 1999.

[91] C. Toyoshima and N. Unwin. Contrast transfer for frozen-hydrated specimens: determination from pairs of defocused images. *Ultramicroscopy*, 25(4):279–291, 1988.

[92] S. Trachtenberg. Mollicutes-wall-less bacteria with internal cytoskeletons. *J Struct Biol*, 124(2-3):244–256, Dec 1998.

[93] R. Y. Tsien. The green fluorescent protein. *Annu Rev Biochem*, 67:509–544, 1998.

[94] Daqi Tu, Gregor Blaha, Peter B Moore, and Thomas A Steitz. Structures of mlsbk antibiotics bound to mutated large ribosomal subunits provide a structural explanation for resistance. *Cell*, 121(2):257–270, Apr 2005.

[95] J. G. Tully. *Enceclopedia of Microbiology*. Academic Press, New York, 1992.

[96] Mikel Valle, Andrey Zavialov, Wen Li, Scott M Stagg, Jayati Sengupta, Rikke C Nielsen, Poul Nissen, Stephen C Harvey, Måns Ehrenberg, and Joachim Frank. Incorporation of aminoacyl-trna into the ribosome as seen by cryo-electron microscopy. *Nat Struct Biol*, 10(11):899–906, Nov 2003.

[97] Mikel Valle, Andrey Zavialov, Jayati Sengupta, Urmila Rawat, Måns Ehrenberg, and Joachim Frank. Locking and unlocking of ribosomal motions. *Cell*, 114(1):123–134, Jul 2003.

[98] M. van Heel, M. Schatz, and E. V. Orlova. Correlation function revised. *Ultramicroscopy*, 46:307–316, 1992.

[99] W. G. Weisburg, J. G. Tully, D. L. Rose, J. P. Petzel, H. Oyaizu, D. Yang, L. Mandelco, J. Sechrest, T. G. Lawrence, and J. Van Etten. A phylogenetic analysis of the mycoplasmas: basis for their classification. *J Bacteriol*, 171(12):6455–6467, Dec 1989.

[100] R. F. Whitcomb and M. E. Coan. Comparative growth of flower, bee and citrus spiroplasmas. In *Abstracts of the Annual Meeting of the American Society for Microbiology*, page 79, 1980.

[101] M. Whitt, L. Buonocore, and J. K. Rose. Liposome-mediated transfection. *Curr Protoc Immunol*, Chapter 10:Unit 10.16, May 2001.

[102] B. T. Wimberly, D. E. Brodersen, W. M. Clemons, R. J. Morgan-Warren, A. P. Carter, C. Vonrhein, T. Hartsch, and V. Ramakrishnan. Structure of the 30s ribosomal subunit. *Nature*, 407(6802):327–339, Sep 2000.

[103] F. Ye, J. Renaudin, J. M. Bové, and F. Laigret. Cloning and sequencing of the replication origin (oric) of the spiroplasma citri chromosome and construction of autonomously replicating artificial plasmids. *Curr Microbiol*, 29(1):23–29, Jul 1994.

[104] M. M. Yusupov, G. Z. Yusupova, A. Baucom, K. Lieberman, T. N. Earnest, J. H. Cate, and H. F. Noller. Crystal structure of the ribosome at 5.5 a resolution. *Science*, 292(5518):883–896, May 2001.

[105] J. Zhu, P. A. Penczek, R. Schröder, and J. Frank. Three-dimensional reconstruction with contrast transfer function correction from energy-filtered cryoelectron micrographs: procedure and application to the 70s escherichia coli ribosome. *J Struct Biol*, 118(3):197–219, Apr 1997.